Automated Quantification of Atherosclerosis in CTA of the Carotid Arteries

Danijela Vukadinović

Cover design by Danijela Vukadinović.

Cover theme: A sink drain getting clogged.

The research described in this PhD thesis was conducted at the Departments of Radiology and Medical Informatics, Erasmus MC, the Netherlands.

ISBN: 978-94-6191-285-5

Printed by IPSKAMP Drukkers

AUTOMATED QUANTIFICATION OF ATHEROSCLEROSIS IN CTA OF CAROTID ARTERIES

AUTOMATISCHE KWANTIFICATIE VAN ATHEROSCLEROSE IN CTA VAN DE HALSSLAGADERS

PROEFSCHRIFT

TER VERKRIJGING VAN DE GRAAD VAN DOCTOR AAN DE
ERASMUS UNIVERSITEIT ROTTERDAM
OP GEZAG VAN DE
RECTOR MAGNIFICUS

PROF.DR. H.G. SCHMIDT

EN VOLGENS BESLUIT VAN HET COLLEGE VAN PROMOTIES.

DE OPENBARE VERDEDIGING ZAL PLAATSVINDEN OP
DONDERDAG 24 MEI 2012 OM 11:30 UUR

DOOR

DANIJELA VUKADINOVIĆ

GEBOREN TE BELGRADO, JOEGOSLAVIË

ERASMUS UNIVERSITEIT ROTTERDAM

Promotiecommissie

Promotor: **Prof.dr. W.J. Niessen**

Overige leden: **Prof.dr.ir. M. Breeuwer**
Prof.dr.ir. B.P.F. Lelieveldt
Prof.dr.ir. A.F.W. van der Steen

Copromotor: **Dr.ir. T. van Walsum**

Mami, tati i bratu

Contents

1 Introduction

How is the human body built and how does it function? What are the causes of disease, and where is disease located? Throughout the history of mankind these questions were answered by the use of invasive methods that included the "opening" of the human body, mainly cadavers. Thanks to these invasive techniques the first precise and complete anatomy works started to appear in the 16th century. The most influential works were published by Leonardo da Vinci [1] and the anatomist and physician Andreas Vesalius [2].

The discovery of X-rays in 1895 [3], and their use for medical applications, introduced a new era, in which non-invasive imaging of the functioning human body became feasible. Nowadays, medical imaging includes many different imaging modalities, such as X-ray, computed tomography (CT), magnetic resonance imaging (MRI), ultrasound (US), nuclear and optical imaging, and has become an indispensable diagnostic tool for a wide range of applications. Initially, the application of medical imaging focused on the visualization of anatomy and on the detection and localization of disease. However, with the development of different modalities it has evolved into a much more versatile tool providing important information on e.g. physiology and organ function [4], biochemistry and metabolism using nuclear imaging (mainly positron emission tomography (PET) imaging [5]), molecular and processes on the molecular and cellular level using molecular imaging techniques [6].

For a long time, human observers' knowledge, experience and pattern recognition abilities have been crucial in the interpretation of medical images. However, as the human eye is not capable of performing accurate quantification, many clinical decisions are made based on the visual estimate of disease progression. With the increasing amount of high dimensional data produced with MRI and CT scanners, and the need for objective quantification, the subjective human assessment of medical images has reached its limits. That is why there is a trend to enhance, assist or replace the work of the clinician by automatic image processing.

Obtaining quantitative data from imaging data often requires the accurate delineation of the target anatomical or pathological region, a process which is called segmentation. The manual segmentation of structures in 3D images is tedious, error prone and very time consuming, which is why many researchers are investigating automatic approaches. Depending on the application, robust fully automatic segmentation is not always feasible. In this case, semi-automated approaches are pursued, where the segmentation is e.g. initialized and/or manually guided or corrected with the aim to accelerate the segmentation process while achieving good accuracy and reproducibility.

In this thesis semi-automated algorithms for quantification of carotid artery atherosclerosis in computed tomography angiography (CTA) images are developed and evaluated. In the following sections, we discuss the background of atherosclerosis, CTA imaging and the contributions of our thesis.

1.1 Atherosclerosis and the Carotid Artery

The word atherosclerosis originates from the Greek words athero (meaning gruel or paste), and sclerosis (meaning hardness). The term refers to the deposit of calcium, fatty substances, cholesterol, cellular waste products and fibrin (collectively known as plaque) that builds up in the inner lining of the artery (Fig. 1.1).

Atherosclerosis is a slow process, which may take many years before leading to symptoms. Increased atherosclerotic burden at the carotid bifurcation first builds up at the outer border of the carotid wall without narrowing of the lumen [7]. In the later stages of plaque progression the vessel lumen becomes compromised, eventually causing stenosis or occlusion. Carotid artery atherosclerosis may lead to ischemic stroke, which constitutes the third cause

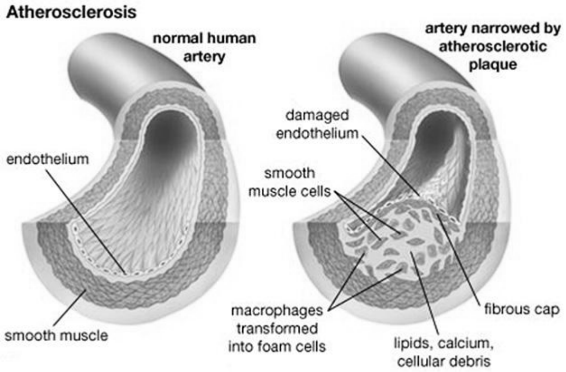

Figure 1.1 Normal (left) and atherosclerotic human artery (right) (http://www.tappmedical.com/atherosclerosis.htm)

of death worldwide and an important cause of disability. Ischemic stroke happens when there is a lack of blood supply to the brain. The most common cause (~50%) of an ischemic stroke is atherosclerosis of large vessels (carotid artery, vertebral artery and the Circle of Willis) [8] (Fig. 1.2). Some studies [9][10][11] show that plaque composition is an important risk factor for ischemic stroke. Furthermore, the plaque volume is a better descriptor of the severity of atherosclerotic disease than the degree of stenosis [12]. Therefore, automating the process of lumen stenosis grading and plaque component segmentation can have important clinical implications, supporting the decision towards medication treatment or surgery (carotid endarterectomy, angioplasty and stenting).

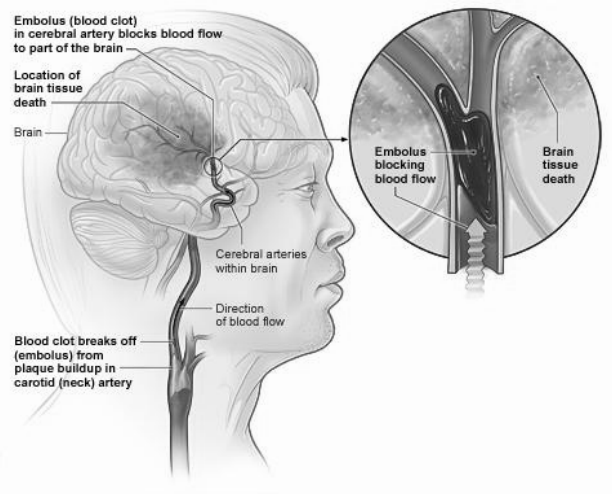

Figure 1.2 An illustration of an occurrence of an ischemic stroke caused by the lack of blood supply to the brain. (http://www.nhlbi.nih.gov/health/health-topics/topics/stroke/types.html)

1.2 Computed Tomography Angiography

For a long time digital substraction angiography (DSA) has been the gold standard for visualizing lumen reduction in carotid arteries because of its high spatial (50μm) and temporal resolution (10ms). Two major trials that used DSA data, The North American Symptomatic Carotid Endarterectomy Trial

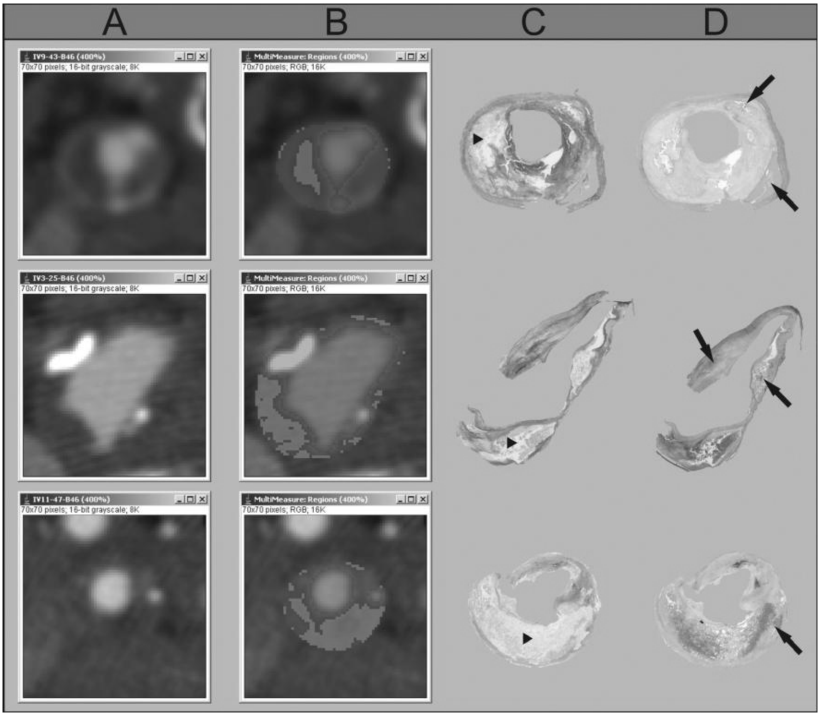

Figure 1.3 Column A: three axial MDCT images of the carotid artery with atherosclerotic plaque. Column B: MDCT plaque morphology images based on differences in Hounsfield Units. Column C and D: Corresponding histological sections with Sirius Red (SR) and haematoxylin eosin (HE) staining, respectively). The blue regions in the MDCT morphology images correspond well with the lumen and calcifications (arrow) on HE stained histological sections. The red regions in the MDCT morphology images correspond well with the red collagen-rich regions in the SR stained histological sections. The yellow regions in the MDCT morphology images correspond well with lipid core (i.e. lipid, hemorrhage and necrotic debris) (arrowhead) regions on histology (the non-red regions on the SR stained sections that are not calcified areas on the HE stained sections). [18]

(NASCET) [13] and the European Carotid Surgery Trial (ECST) [14], established luminal stenosis grade as an important criterion in deciding on treatment planning of patients with cerebral ischemia symptoms. However, there are a number of limitations of DSA. It is an invasive procedure that can only depict the intraluminal portion of the vessels. Furthermore, only a limited number of projections is typically obtained for actual luminal reduction measurement, which may result in a wrong estimate of the maximum lumen reduction

In view of the limitations of DSA, there is an increasing interest in CTA as a modality for assessing the carotid artery bifurcation. Computed tomography angiography is an imaging modality that can be used to accurately visualize the severity of luminal stenosis in 3D [15]. With CTA it is extremely easy to detect calcifications in the carotid artery (Fig. 1.3). CTA has also become an established method for successful artery calcium scoring in coronary arteries [16][17]. With the introduction of MultiDetector CT (MDCT) in 1998 fast imaging at high temporal and spatial resolution became possible. The main advantage of this technology compared with conventional mechanical spiral CT scanner is that it consists of multiple detector rows, which allow simultaneous acquisition of multiple slices. CT scanners using e.g. 16 and 64 – slice technology offer a very high spatial resolution and can generate very thin slices allowing the acquisition of isotropic voxels [18]. It has been shown, using 16-slice CT, that noncalcified coronary lesions could be detected with a reasonable sensitivity of 78% [19]. It has been also shown, with comparison to histology, that assessment of carotid atherosclerotic plaque components is feasible with MDCT using different plaque components Hounsfield units (HU) densities in vitro [20] and in vivo [21]. In Figure 1.3 an illustration from [21] of atherosclerotic plaques in MDCT cross-sectional slices and corresponding histology samples are shown.

1.3 Quantification of Carotid Atherosclerosis

Plaque in the carotid artery has a complex structure, and may consist of several components. The presence of plaque components (i.e. haemorrhage, fibrous tissue, lipid rich necrotic core, calcification), their percentage and their volume may be important in assessing the nature of the plaque, including its vulnerability to rupture. Determining such plaque characteristics manually is a tedious, and error-prone task, which could be facilitated much by (semi-)automatic quantification approaches. The automatic analysis of carotid atherosclerotic plaque is a challenging task, owing to the limited contrast between the plaque components and the surrounding soft tissue.

The purpose of the work described in this thesis is to develop and evaluate methods that allow automated quantification of atherosclerosis in the carotid bifurcation in CTA images. We aim to develop methods to quantify carotid artery stenosis and accurately segment the outer vessel wall and its plaque components from MDCT data. The methods are evaluated on large sets of MDCT imaging data.

This thesis is further organized as follows. Chapter 2 presents an automated method for carotid artery lumen segmentation in CTA. The method uses three user defined seed points, located in the common carotid artery (CCA), internal carotid artery (ICA) and external carotid artery (ECA) to extract the lumen centerline using a minimal cost path approach. The method is validated with respect to stenosis grading. In Chapter 3 the focus shifts to outer vessel wall segmentation. A novel method is presented which utilizes a variant of the lumen segmentation method from Chapter 2 as a starting point. Subsequently, a voxel based classification is used to separate inner and outer region of the vessel. A machine learning algorithm is trained using spatial, intensity and Gaussian features. In Chapter 4 carotid artery plaque components are segmented using the method from Chapter 3 and applying different HU thresholds to segment different plaque components. The method is evaluated with respect to cardiovascular risk factors correlations with plaque component percentages and volumes. In Chapter 5 a novel level set based method is presented for outer vessel wall segmentation. Using HU thresholding, the method is evaluated with respect to plaque component volumes and percentages. Chapter 6 represents conclusion of this thesis with a summary.

1.4 References

[1] K. D. Keele. Leonardo Da Vinci's influence on renaissance anatomy, *Med Hist,* 8(4): 360–370, October 1964.

[2] A. Vesalius. De humani corporis fabrica libri septem, *Ex officina Joannis Oporini*, 1543.

[3] V. Gray. *Roentgen's revolution: the discovery of the X-Ray*, Little Brown & Co, June 1973.

[4] M. Soleimani, R.J. Shipley, N. Smith and C.N. Mitchell. Medical imaging and physiological modeling: linking physics and biology, *Biomedical Engineering Online*, 2009.

[5] E. Hiesiger, J.S. Fowler, A.P. Wolf, J. Logan, J.D. Brodie, D. McPherson, R.R. MacGregor, D.R. Christman, N.D. Volkow, E. Flamm. Serial PET studies of human cerebral malignancy with [1-11C] putrescine and [1-11C] 2-deoxy-D-glucose, *Journal of Nuclear Medicine*, Aug, 1987.

[6] R. Weissleder. Molecular imaging: exploring the next frontier, *Radiology*, 212: 609-614, September 1999.

[7] S. Glagov, E. Weisenberg, C.K. Zarins, R. Stankunavicius, G.J. Kolettis. Compensatory enlargement of human atherosclerotic coronary arteries, *N Engl J Med* 316:1371-75, 1987.

[8] C. Warlow, C. Sudlow, M. Dennis, J. Wardlaw, P. Sadercock. Stroke, *Lancet*, 362:1211-24, 2003.

[9] P. M. Rothwell, R. Gibson and C. P. Warlow. Interrelation between plaque surface morphology and degree of stenosis on carotid angiograms and the risk of ischemic stroke in patients with symptomatic carotid stenosis. on behalf of the european carotid surgery trialists' collaborative group, *Stroke*, 31(3): 615–621, Mar 2000.

[10] J. K. Lovett, P. J. Gallagher, L. J. Hands, J. Walton and P. M. Rothwell. Histological correlates of carotid plaque surface morphology on lumen contrast imaging, *Circulation*, 110 (15): 2190–2197, Oct 2004.

[11] M. Naghavi, P. Libby, E. Falk, S. W. Casscells, S. Litovsky, et al. From vulnerable plaque to vulnerable patient: A call for new definitions and risk assessment strategies: Part I, *Circulation*, 108: 1664-1672, 2003.

[12] Asymptomatic carotid atherosclerosis group. Endarterectomy for asymptomatic carotid artery stenosis. *JAMA*, 73:1421–1428, 1995.

[13] ECST collaborators. Randomised trial of endarterectomy for recently symptomatic carotid stenosis: final results of the MRC european carotid surgery trial (ecst). *Lancet* 351 (9113), 1379–1387, 1998.

[14] NASCET Collaborators. Beneficial effect of carotid endarterectomy in symptomatic patients with high-grade carotid stenosis. *N. Engl. J. Med.* 325 (7), 445–453, 1991. <http://content.nejm.org/cgi/content/abstract/325/7/445>.

[15] J.W. Mark, M.J. Koelemay, P.J. Nederkoorn, J.B. Reitsma, C.B. Majoie Systematic review of computed tomographic angiography for assessment of carotid artery disease. *Stroke*, 35:2306-12, 2004.

[16] A.S. Agatston, W.R. Janowitz, F.J. Hildner, N.R. Zusmer, M. Jr. Viamonte and R. Detrano. Quantification of coronary artery calcium using ultrafast computed tomography. *J Am Coll Cardiol*, 15:827-832, 1990.

[17] C.R. Becker, A. Knez, T. F. Jakobs, S. Aydemir, A. Becker, U.J. Schoepf, R. Bruening, R. Haberl and M. F. Reiser. Detection and quantification of coronary artery calcification with electron-beam and conventional CT, *Eur Radiology*, 9:620-4, 1999.

[18] G. D. Rubin and N. M. Rofsky. *CT and MR angiography: comprehensive vascular assessment*, Lippincott Williams & Wilkins, 2009.

[19] A. W. Leber, A. Knez, A. Becker, et al. Accuracy of multidetector spiral computed tomography in identifying and differentiating the composition of coronary atheroslcerotid plaques: a comperative study with itracoronary ultrasound“, *J Am Coll Cardiol*, 47(7): 1241-7, 2004.

[20] T. T. de Weert, M. Ouhlous, P. E. Zondervan, J. M. Hendriks, D. W. J. Dippel, M. R. H. M. van Sambeek, and A. van der Lugt. In vitro characterization of atherosclerotic carotid plaque with multidetector computed tomography and histopathological correlation, *Eur. Radiol.*, 15(9): 1906–1914, Sep 2005.

[21] T. T. de Weert, M. Ouhlous, E. Meijering, P. E. Zondervan, J. M. Hendriks, M. R. H. M. van Sambeek, D. W. J. Dippel, and A. van der Lugt. In vivo characterization and quantification of atherosclerotic carotid plaque components with multidetector computed tomography and histopathological correlation, *Arterioscler. Thromb. Vasc. Biol.*, 26(10): 2366–2372, Oct 2006.

2 Semi-automatic Level-Set Based Stenosis Quantification of the Internal Carotid Artery in CTA

This chapter is based on:

D. Vukadinović. et al. Semi-automatic level-set based stenosis quantification of the internal carotid artery in CTA, manuscript in preparation.

Abstract

A semi-automatic carotid artery lumen segmentation method, aimed at accurate stenosis quantification, is developed and evaluated. The method is initialized with 3 user defined seed points: one in the common carotid artery (CCA), one in the internal carotid artery (ICA) and one in the external carotid artery (ECA). An initial centerline is extracted based on intensity statistics in the neighborhood of the seed points. This centerline is used to initialize a level set lumen segmentation that utilizes intensity statistics along the extracted path for defining the carotid artery lumen. A final centerline is extracted by skeletonization of the lumen segmentation. Lumen segmentation and centerline are then used for automated stenosis detection and quantification. Parameter settings are optimized for stenosis quantification accuracy on a training set of 9 datasets.

Stenosis grading is evaluated on 41 dataset from the carotid bifurcation segmentation and stenosis grading framework in CTA images (CLS2009 framework). The mean stenosis quantification error was 19.3 % and 18.2 % for area stenosis and diameter stenosis respectively, and our method ranked second among the algorithms that have participated in the CLS2009 challenge.

2.1 Introduction

Stroke is one of the leading causes of death and a cause of major disability among the surviving individuals in the western world. The degree of carotid artery stenosis is an important factor in therapy selection, e.g. whether to perform carotid endarterectomy [1]. Carotid stenosis grading is currently increasingly performed using CTA, but this measurement is subject to inter-observer variability [2]. Therefore, there is a large interest in methods that allow more objective grading of carotid artery stenosis from CTA data, using (semi-)automatic approaches.

Automatic methods for stenosis grading generally require lumen segmentation as a prior step. A variety of lumen segmentation methods exist. Those include methods based on the evolution of curves or surfaces (Lorigo et al. [3]; Zhuge et al. [4]; Yan and Kassim [5], Manniesing et al. [6], Scherl et al. [7], Krissian et al. [8], Cuisenaire [9], van Bemmel et al. [10]), model based approaches (Mille et al. [11], Wong et al. [12], Zuluaga et al. [13], Valencia et al. [14]), particle filtering (Florin et al. [15]) and graph-cuts (Boykov and Jolly [16], Homann et al. [17]; Schaap et al. [18], Freiman et al. [19], Gulsun et al. [20]). An overview of vessel segmentation techniques has been provided by Lesage et al.[21].

Compared to the quite extensive literature on vessel segmentation, relatively less work has focused on (semi-) automatic carotid artery stenosis grading. Results of semi-automatic stenosis grading methods for carotid arteries in CTA images have been reported by Berg et al. [22], Scherl et al. [7] and Wintermark et al. [23]. The evaluations have been carried out on different datasets and using different evaluation measures. Neither of these papers explicitly defines how stenosis is measured with automated methods.

Several authors participated in the CLS2009 framework [24] where lumen segmentation and stenosis grading on CTA carotid artery data was evaluated on 56 datasets using a standardized evaluation framework. Most of the lumen segmentation methods split the problem into two steps: (i) initial centerline extraction and (ii) subsequent lumen segmentation.

A fully automated lumen segmentation method was proposed by Cuisenaire et al. [9]. The centerline of each vessel was first extracted using a fast marching algorithm The vessel lumen was segmented using 3D active objects initialized as a tube around the centerline. Krissian and Arencibia-García [8] first extracted an initial centerline using a minimal cost path based on a multi-scale vesselness filter response. After detecting the junction position and cutting or extending the paths based on the requested lengths, a level set segmentation was used for lumen segmentation. Freiman et al. [19] used a two-phase graph-based energy minimization approach initialized with start and end seed points inside the vessel. First, the weighted shortest path between the vessel seed endpoints based on image intensity, image intensities around the seed points, and vessel path geometric characteristics was computed. Subsequently a region of interest from the shortest path and the estimated vessel radius was derived, and the vessel boundaries were extracted by minimizing the energy on a corresponding graph cut. Gulslun et al. [20] used graph-cuts optimization techniques together with centerline models for segmenting the carotid arteries. They first extracted the centerline between the user placed seed points using a minimal path method operating on a medialness map. The lumen of carotid arteries was then extracted by a graph-cut optimization technique using the detected centerlines as input. Mille et al. [11] based their algorithm on an extension of the minimal path method that models the vessel as a centerline and boundary. This is achieved by adding one dimension for the local radius around the centerline. Next step was the definition of the anisotropic local metrics to minimize. In order to deal with carotid stenosis or occlusions, the segmentation was refined using a region-based level set method derived from the Chan and Vese model [25].

Three participants of the CLS2009 challenge evaluated their method with respect to stenosis grading. Valencia et al [14] proposed a lumen segmentation approach using right generalized cylinders (RGC) with piece-wise constant parameters to model carotid artery lumen. RGC were extracted using 2D contours extracted along the minimal cost path between two points [26].

Zuluaga et al.[13] proposed an algorithm consisting of two stages: intensity-based preprocessing using Dual Tree Complex Wavelet Transform filter [27] denoising and Fuzzy C-means classifier and model-based lumen delineation using elastic model and multi-scale eigen-analysis of the inertia matrix [28]. Stenosis quantification is performed on a plane-by-plane basis using isocontours. Wong et al [12] generated a centerline using a vesselness measure and minimal cost path search. The method used a 1D intensity model and resulted in a centerline with associated vessel radii. Segmentation and the stenosis grading were performed assuming circular lumen cross-sections. Reference part is 20 mm distal from the stenosis position and has a length of 10 mm. The stenosis is calculated using NASCET [29] – like criteria defined by the CLS2009 organizers.

Our contribution is a semi-automated method that improves on previous work of Manniesing et al. [6]. Manniesing et al. used three user–defined points to extract an initial centerline which is further used as an initial level set in order to segment the lumen. The cost function for the initial centerline extraction and the stopping function for the level set evolution use intensity and image gradient features. In this paper we present improvements on the vessel segmentation method of Manniesing et al. regarding the initial centerline extraction and level set evolution. We further adapted and optimized this method for accurate stenosis grading by performing parameter optimization. In order to perform stenosis grading on the lumen segmentation we incorporated the centerline extraction method by Antiga et al [30]. Our method has been evaluated for stenosis grading using a publicly available framework for carotid lumen segmentation and stenosis grading [24].

2.2 Materials and Methods

The lumen segmentation method used for this study consists of two steps: an initial centerline extraction and subsequently a level set based lumen segmentation that utilizes the initial centerline for initialization of the levelset. In order to determine the stenosis degree the final centerline and the lumen cross sections orthogonal to the centerline are extracted from the lumen segmentation.

We modified the method of Manniesing et al. [6] in the following way. First, the robustness of the method was improved by integrating morphological operations in order to avoid leaking into bony structures which happens in our case because in the carotid artery challenge database the ICA seed points are mostly positioned more distally than the seed points used in their evaluation study [6]. Second, the initial centerline tracking was improved to cope with the higher stenosis degrees that were present in the challenge data compared to the data used in [6]. Third, for the same reason, the level set stopping function used for the lumen segmentation was adapted. We also added a final centerline extraction method [30] for stenosis grading calculation.

2.2.1 Initial Centerline Extraction

The lumen centerline in contrast enhanced CTA consists of voxels with intensities ranging between the lower intensities of the surrounding soft tissue and higher intensities of bones and calcified tissue. We define an intensity range filter by multiplying two error functions which mask the lower and higher intensities respectively:

$$\begin{aligned} P(x) = &\left(\frac{1}{2}+\frac{1}{2}\operatorname{erf}\left(\frac{I(x)-\beta_l}{\theta}\right)\right) \\ &\cdot\left(\frac{1}{2}-\frac{1}{2}\operatorname{erf}\left(\frac{I(x)-\beta_u}{\theta}\right)\right) . \end{aligned} \tag{1}$$

Here *I(x)* is the image intensity at position x, θ is a user defined slope of the error functions and β_l and β_u are computed from the image as follows:

$$\begin{aligned} \beta_l &= \mu - k_l\sigma \\ \beta_u &= \mu + k_u\sigma , \end{aligned} \tag{2}$$

where μ and σ are intensity mean and variance of the neighborhood around the seed points and k_l and k_u are constants to be optimized with respect to stenosis degree for a value of $\theta = 20$ as used in [6].

The initial centerline is extracted using Dijkstra's algorithm which determines a minimum cost path between two seed points. The cost function used in Dijkstra algorithm is defined for each voxel x as the inverse value of $P(x)$ from equation (1). In the remainder of this paper the resulting image of filtering CTA image with the band-pass filter (1) is named intensity-range image, while the inverse image of the intensity range image is called cost image.

In [6] the authors use an additional factor in the intensity range filter (1) to remove imaging artifacts and surrounding anatomical structures (such as bones) from the image. This is achieved by locally (per slice) and globally calculating intensity variance.

We did not implement this additional factor, for several reasons. First, the ICA seed points used in our study are positioned more distally, where the artery enters the skull. In this region the bone is more close to the artery making bone removal more challenging than in [6]. Second, the data used for this study has on average higher degrees of stenosis than the data in the study of Manniesing et al. Finally, the method based on local variance measurement would remove narrow stenotic lumen resulting in incorrect initial centerline extraction.

Instead we use a morphological opening on the intensity range image in order to prevent leakage into bone. This method was found to be very effective in removing skull bones edges that are represented in the intensity range image as thin lines-like structures (Fig. 2.1). At the same time, morphological opening leaves bulb like structures (such as stenotic lumens) untouched.

In [6] the cost value, $C(x)$, is set to be in the range $[1, 10^5]$. Having a minimum cost prevents too long paths., However, in our training set this resulted in miss detected paths in a few datasets since shorter paths are favored even when they are partly incorrectly positioned (e.g. through the jugular vein). We resolved this issue by setting the minimum cost value to be close to zero:

$$\begin{gathered} C(x) = \frac{1}{P\big(I(x)\big)} - 1 + \varepsilon, \qquad P\big(I(x)\big) > 10^{-5} \\ C(x) = 10^5,\ P\big(I(x)\big) > 10^{-5}, \end{gathered} \tag{3}$$

where ε is chosen to be small: $\varepsilon = 0.01$. This change did not affect the correctly detected paths in the training set.

2.2.2 Lumen Segmentation

For vascular lumen segmentation the geodesic active contours approach is used [6]. The approach is described by the following partial differential equation:

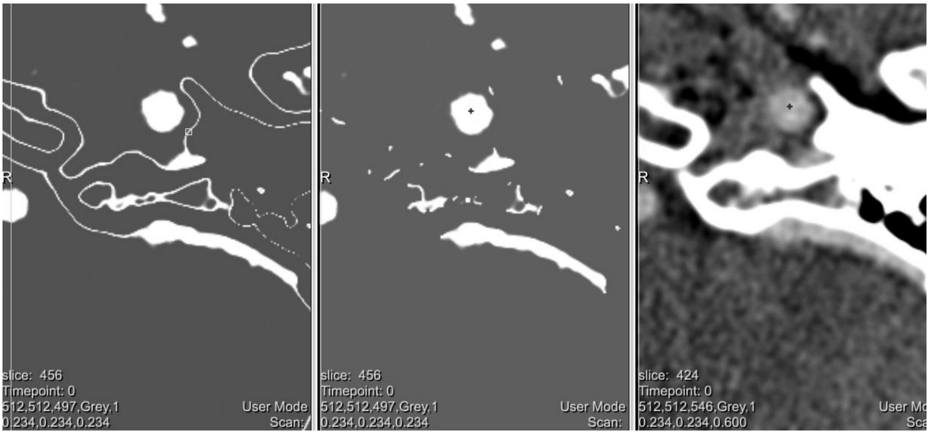

Figure 2.1 Morphological opening applied on the intensity – range image to remove bony structures. Left: intensity-range image P(I(x) before opening; Center: P(I(x)) after opening is applied; extracted centerline position is indicated with a dot; Right: original CTA image.

$$\Phi_t - \alpha \nabla F_{segm} \nabla \Phi + F_{segm}(1 - \gamma k_{min})|\nabla \Phi| = 0\,, \tag{4}$$

where Φ is the level set function, α is a weighting term, F_{segm} is the image-based speed term for segmentation, and γ is the weighting term of the minimal curvature term k_{min}. The level set is initialized with the initial centerlines extracted in the previous step. The image based stopping function F_{segm} is defined by the image intensity and image gradient:

$$F_{segm} = \begin{cases} \left(-\,erf\left(\frac{1-\beta_l'}{\theta'}\right)\right)\left(erf\left(\frac{1-\beta_u'}{\theta'}\right)\right) & |\nabla I| < \tau \\ 0 & |\nabla I| \geq \tau \end{cases} \tag{5}$$

$$\begin{aligned} \beta_l' &= \mu' - \sigma' k_l \\ \beta_u' &= \mu' + \sigma' k_u \end{aligned} \tag{6}$$

$$\begin{aligned} \mu' &= (1-\eta)\mu_l + \eta\mu_g \\ \sigma' &= (1-\eta)\sigma_l + \eta\sigma_g \,, \end{aligned} \qquad (7)$$

where *erf ()* is the error function, I denotes the image intensity, θ is the slope of the error functions,∇I is the gradient, k_l and k_u are two constants and τ is the threshold on the gradient magnitude. The stopping function is constructed by using local and global intensity statistics derived from the neighborhood of the initial centerline points: σ_l and μ_l denote local standard deviations and means in a small circular neighborhood around the initial centerline as a function of the axial slice, while σ_g and μ_g are the global standard deviation and mean calculated over the initial centerline. η is a weighting parameter for balancing influence of the local and global estimates. The stopping function is set to have negative minimum value of -1 in order to prevent leaking in the neighboring structures usually occurring with strictly positive speed ranged functions only. In [6] small and consistent under-segmentation was observed and an additional dilation of the segmentation, φ, was introduced. This dilation parameter is optimized in the work described in this paper.

In cases where the initial centerline is positioned at the border of the lumen, the neighborhood statistics is skewed to the lower intensity values. This may cause the segmentation to leak into the non-lumen lower intensity regions. In our adapted implementation this issue was solved by deriving the abovementioned statistics after discarding a portion, $k_{balance}$, of the points with the lowest intensity.

For deriving the stenosis degree from the segmented lumen, we require a smaller carotid artery range than the range determined by the seed points provided by the CLS2009 framework. Therefore, we iteratively apply our segmentation method. We first determine centerline and lumen segmentation from the original seed points, and use this segmentation to determine the bifurcation region of interest. We then position new seed points closer to the bifurcation, referred to as cropped seed points in the remaining of this paper. The cropped seed points are placed in the center of mass of the lumen segmentation on the axial slice at fixed distances from the bifurcation slice.

The method is rerun using the cropped seed points, resulting in the final segmentation. This rerun is done in order to achieve more accurate segmentation by avoiding external artery branches that are positioned more distally and to minimize leaking to other neighboring structures.

2.2.3 Final Centerline Extraction

From the converged level set segmentation the zero level set is extracted. The extracted surface is then smoothed using the method by Taubin et al [31] in order to remove irregularities in the surface. Finally, the method of Antiga et al [30] is used to extract the ICA centerline given the smoothed surface and two cropped seed points: one in CCA and one in ICA. This analysis is only applied to the ICA, as the stenosis degree is calculated in the ICA in the CLS2009 framework. This centerline extraction approach is based on solving the Eikonal equation on the Voronoi diagram embedded into the object, with wavefront speed inversely proportional to Voronoi ball radius values.

2.2.4 Stenosis Degree Calculation

Stenosis quantification is performed in the region between the cropped seed points positioned in CCA and ICA, using the method described by Hameeteman et al. [24]. Using the centerline extracted between these points, planes perpendicular to the centerline are determined. For every cross-sectional plane the contour that results from intersecting the original non-smoothed iso surface with the plane is determined [32]. The resulting contours are then used to calculate the cross-sectional area and minimal diameter of the vessel along the centerline. The resulting area and diameter curves are smoothed using a Gaussian kernel with a standard deviation of R mm. The minimal value of these smoothed curves is defined as the location of the stenosis. Using the found position, the degree of stenosis is then determined from the un-smoothed curve using both the minimum value and the average value of the distally positioned reference area. We use the following NASCET-like [29] criteria for the area-based stenosis grade S_a:

$$S_a = 100\% \times \left(1 - \frac{a_m}{a_r}\right) \tag{8}$$

where a_m is the minimal cross-sectional area along the CCA and ICA, and a_r the average cross-sectional area over a 5mm long distal reference part of the ICA positioned 15 mm from the stenosis. For the diameter-based stenosis grade S_d we similarly use:

$$S_d = 100\% \times \left(1 - \frac{d_m}{d_r}\right) \tag{9}$$

where d_m and d_r are the minimal and average reference cross-sectional diameter, respectively. The definition of the cross-sectional diameter is explained in [24].

2.3 Data and Experiments

2.3.1 Data Description and Experiments

The method was trained and evaluated using data from the CLS2009 framework [24]. This framework contains 15 datasets for training and 41 for testing from three different sites, with varying stenosis degrees, and includes a manual reference standard. The region of interest in which lumen segmentation and stenosis grading was evaluated starts in the CCA 20 mm caudal of the bifurcation slice, and ends in ICA up to 40 mm distal to the bifurcation slice and includes the ECA up to between 10 and 20 mm distal of the bifurcation slice. Participants of the challenge should submit partial volume lumen segmentations and stenosis area and stenosis diameter gradings per dataset. The lumen segmentation performance is evaluated using Dice, mean surface distance and Hausdorff distance [24] and the stenosis grades are evaluated using absolute difference.

2.3.2 Implementation

The first two steps of the method, initial centerline extraction and lumen segmentation, use three seed points provided by the CLS2009 framework. The cropped seed points are positioned in CCA 20 mm caudal of the bifurcation slice, in the ICA at 40 mm cranial of the bifurcation slice and in ECA 20 mm cranial of the bifurcation slice. The full method was run using the cropped seed points.

From the final level set image an iso surface is extracted and smoothed using VTK software. The final centerline is extracted from the smoothed isosurface using the VMTK package.

Minimal area and minimal diameter search is performed in a region starting at 1 mm distance distal to the bifurcation slice in ICA along the centerline and ending 20 mm under the last cropped seed point (ICA). The cross-sectional contours were sampled at 1 mm spacing along the centerline using the vtkCutter class. The reference area is a 5 mm length segment starting 15 mm distally to the minimal area or diameter cross-section.

In cases where the lumen segmentation was shorter than 20mm, both area and diameter stenosis were assigned a value of 100% since it means that there was a complete occlusion in the given dataset.

Parameter	Parameter’s description	Range	Optimized value
τ	Image gradient threshold	[90 … 200]	100
φ	The post distance value to expand the final level set	[0.0 … 1.0]	0.6
η	Balance parameter between local and global statistics along the centerline.	[0.0 .. 1.0]	0.2
ρ	Initial distance of the GAC	[0.1 … 1.5]	0.5
α	Advection coefficient in GAC	$[0, 10^{-4}, 10^{-3}, 10^{-2}]$,	0.001
γ	Curvature coefficient in GAC	$[0, 10^{-4}, 10^{-3}, \dots 1.0]$	0
$k_{balance}$	Lower intensity portion of initial centerline points.	[0.3 … 0.7]	0.5
R[mm]	Gauss kernel used in stenosis calculation	[1, 2, 3]	1
k_l	Lower coefficient for cut – off values in intensity distribution equations.	[0.8 ... 3]	1.2
k_u	Upper coefficient for cut – off values in intensity distribution equations.	[0.8 ... 3]	1.2

Table 2.1 Results of the parameters tuning on the training set

2.3.3 Parameter Optimization on the Training Set

We ran our centerline extraction algorithm on the fifteen training datasets of the CLS2009 framework. In three training datasets the ICA seed points were positioned within the region of interest where the stenosis area and diameter should be evaluated. Since our method stops at (or close to) seed points provided, we had to exclude these 3 datasets from the training sets. Additionally three datasets were excluded from training because the initial centerline was not correctly extracted and the subsequent lumen segmentation was not correct.

We optimized ten parameters of the algorithm (see Table 2.1): τ - image gradient threshold in equation (5), φ - the post distance value to expand the final level set, η - balance in equation (7), ρ - initial distance of the GAC, α - advection coefficient from equation (4), γ - curvature coefficient from equation (4), R - Gauss kernel used in stenosis calculation, k_l and k_u - two coefficients from equations (2) and (6). These parameters were optimized on the training set for stenosis quantification accuracy. The optimization minimizes the mean value of both the area and diameter stenosis errors of the 9 nine remaining datasets from the training set. The stenosis error is defined as the absolute difference between measured stenosis and ground truth stenosis as provided by the CLS2009 framework.

The parameters for the initial centerline extraction were taken from [6] since we assume that they do not influence the stenosis quantification accuracy. The parameters that were related to lumen segmentation were optimized following a multiresolution tuning. All parameters were optimized individually in the order listed in Table 2.1.

2.3.4 Test Set Experiments

Using the optimized parameters, the method was applied to the 41 test datasets of the CLS2009 framework. The method was evaluated against both lumen segmentation accuracy and stenosis degree quantification error.

2.4 Results

2.4.1 Parameter Optimization Results

Parameters optimization results with respect to stenosis grading are presented in Table 2.1.

On the training set, the optimal settings resulted in a mean area and diameter stenosis error of 10% (p = 0.47) with average area stenosis error of 12.8% (p = 0.56) and average diameter stenosis error of 7.2 % (p = 0.35).

		Stenosis		Lumen segmentation		
	Number of datasets	Area [%]	Diam [%]	D_{si} [%]	D_{msd} [mm]	D_{hd} [mm]
All test set datasets	41	19.3	18.2	82.7	0.75	3.68
Excluded data with wrongly placed ICA seed points (3)	38	15.7	15.5	82.9	0.69	3.19
Excluded data with incorrectly extracted initial CL(5) and wrongly placed ICA seed points (3)	33	11.7	10.9	87.5	0.31	2.08

Table 2.2 The results of our method on a complete test set data and subsets of the test set: lumen segmentation and stenosis quatification.

2.4.2 Results of the Carotid Challenge

The results on the test data of the carotid artery challenge are presented in Table 2.2. Besides the results on all 41 datasets, the results after excluding different subsets of the test set are shown. Datasets where the seed points in the ICA where incorrectly placed (3 datasets) resulted in an incorrect stenosis evaluation, and therefore we also present the results when excluding these cases.

We also determine the accuracy of stenosis quantification if we would use only the datasets where the initial centerline was correctly extracted and the seed points in ICA were correctly positioned.

2.5 Discussion

We have proposed a semi-automatic method for lumen segmentation and stenosis quantification in CTA images and evaluated the method using the carotid challenge framework [24]. The method uses three seed points provided by the CLS2009 framework. The method has been optimized for stenosis quantification.

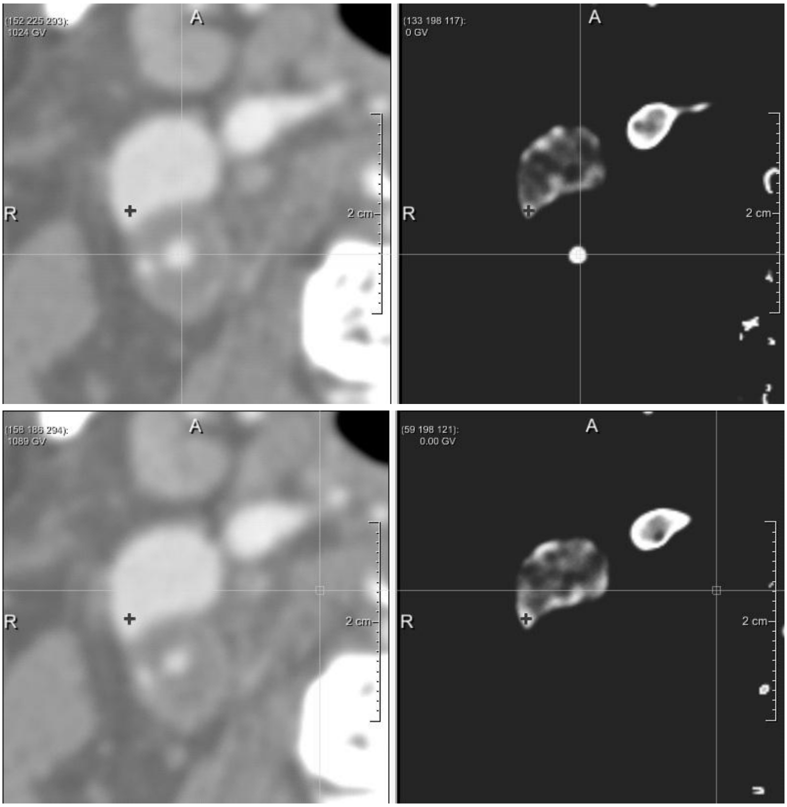

Figure 2.2 Axial consecutive slices of carotid artery CTA scan with high stenosis (left), corresponding intensity-range images P(I(x)). Crosses represent initial centerline points erroneously positioned in jugular vein.

On the 41 datasets of the test set, the method made higher stenosis error than on the training set: 19.3% for area and 18.2% for diameter stenosis. The total rank was 4.04 which correspond to the second position out of 4 methods that have participated in the challenge (Table 2.3). In the CLS2009 framework, three of the datasets have ICA initialization seed points erroneously positioned, as they are inside the region to be evaluated. Since stenosis quantification uses only ICA for evaluation, our method will not work in those cases. We, therefore, also evaluated our method on the remaining 38 datasets and the area and diameter stenosis error was reduced to 15.7% and 15.5% respectively. The total rank of our method on these 38 datasets was 3.96 and our algorithm scores as the best out of 4 stenosis challenge algorithms.

In 5 datasets, initial centerline extraction, was unsuccessful, as parts of the initial centerline were positioned outside the arterial lumen. The main reason of the initial centerline error was lower contrast in some parts of the vessel caused by higher stenosis degree (Fig 2.2). In order to compare the stenosis grading success on the test set with the success on the train set, the method was evaluated when we excluded the datasets where the centerline extraction failed. The error decreased to 11.7% and 10.9% for area and diameter stenosis respectively, which is similar to the results on the training dataset where we also excluded failed centerlines and wrongly positioned ICA seed points.

Three other methods participated not only in the lumen segmentation challenge, but also in the stenosis challenge CLS2009 [24]: Zuluaga et al. [13], Wong et al. [12] and Valencia et al. [14]. The stenosis area and diameter errors of our method and the method of Zulaga et al. are similar. On the all 41 data from the test set the algorithm of Zuluga et al. has higher rank but after excluding datasets where ICA seed point was position within evaluation region, our method scored better than the method of Zuluaga et al. The other two methods had higher error for both area and diameter stenosis (Table 2.3).

To improve reliability of the method, initial centerline extraction success should be increased. One practical solution to this would be to place additional seeds points, e.g. at the bifurcation or at the stenotic region. This would facilitate a more robust stenosis grading, at the expense of limited additional user interaction. Alternatively, more robust automated approaches could be explored, e.g. by also integrating higher order image information, such as vesselness measures, in the minimum cost path approach.

In conclusion, we developed a method for semi-automated stenosis grading of the internal carotid artery. Evaluation on a publicly available dataset showed promising results, demonstrating that semi-automatic stenosis grading is becoming feasible.

	Number of datasets 41			Number of datasets 38			Number of datasets 33		
	Stenosis			Stenosis			Stenosis		
	Total rank	Area [%]	Diam [%]	Total rank	Area [%]	Diam [%]	Total rank	Area [%]	Diam [%]
Reference	1.00	0.0	0.0	1.0	0.0	0.0	1.0	0.0	0.0
Observer A	2.17	2.9	3.4	2.21	2.8	3.3	2.21	2.9	3.0
Observer B	2.59	4.3	5.4	2.57	3.9	4.8	2.64	3.7	5.3
Observer C	2.80	5.0	5.7	2.78	4.5	5.3	2.76	4.1	5.3
REGROW D.Vukadinovic	4.04	19.3	18.2	3.96	15.7	15.5	3.79	11.7	10.9
MARACAS Zulaga et al. [30]	3.91	16.9	17.0	3.96	16.2	16.0	4.06	17.0	17.7
Media Wong et al.[29]	4.65	25.2	31.4	4.61	24.3	30.2	4.47	19.9	26.2
RGC Valencia et al.[9]	5.15	37.0	43.3	5.16	37.1	43.1	4.97	33.4	39.1

Table 2.3 Stenosis error compared to the reference standard of all the cls2009 stenosis challenge participants on the test set and its subsets. Our method is under name “REGROW”.

2.6 References

[1] M. D. Hill, M. M. Foss, J. V. Tu and T. E. Feasby. Factors influencing the decision to perform carotid endarterectomy, *Neurology*, 62:803-805, March 2004.

[2] G. Kılıçkap, E. Ergun, E.Başbay, P. Koşar and U. Kosar. Carotid stenosis evaluation by 64-slice CTA: comparison of NASCET, ECST and CC grading methods, *The International Journal of Cardiovascular Imaging*, August 11, 2011.

[3] L. M. Lorigo, O. D. Faugeras, W. E. L. Grimson, R Keriven, R. Kikinis, A. Nabavi, C. F. Westin. CURVES: curve evolution for vessel segmentation, *Medical Image Analysis,* 5 (3), 195–206, 2001.

[4] F. Zhuge, G. R. Rubin, S. Sun and S. Napel. An abdominal aortic aneurysm segmentation method: level set with region and statistical information, *Medical Physics,* 33 (5), 1440–1453, 2006.

[5] P. Yan and A. A. Kassim. Segmentation of volumetric MRA images by using capillary active contour, *Medical Image Analysis* 10 (3): 317–329, 2006.

[6] R. Manniesing, M. Schaap, S. Rozie, K. Hameeteman, D. Vukadinović, A. van der Lugt and W. J. Niessen. Robust CTA Lumen segmentation of the atherosclerotic carotid artery bifurcation in a large patient population, *Medical Image Analysis*, 14(6): 759-769, December 2010

[7] H. Scherl, J. Hornegger, M. Prümmer and M. Lell. Semi-automatic levelset based segmentation and stenosis quantification of the internal carotid artery in 3D CTA data sets, *Medical Image Analysis,* 11(1): 21–34, 2007.

[8] K. Krissian and S. Arencibia-García. A minimal cost path and level set evolution approach for carotid bifurcation segmentation, *Midas J*. 2009.

[9] O. Cuisenaire, S. Virmani, M. E. Olszewski and R. Ardon. Fully automated segmentation of carotid and vertebral arteries from contrast enhanced cta, *SPIE Medical Imaging,* February 2008

[10] C. M. van Bemmel, M. A. Viergever and W. J. Niessen. Semi-automated segmentation and stenosis quantification of 3D contrast-enhanced MR angiograms of the internal carotid artery, *Magnetic Resonance in Medicine* 51 (4), 753–760, 2003b.

[11] J. Mille, F. Benmansour and L. D. Cohen. Carotid lumen segmentation based on tubular anisotropy and contours without edges, *Midas J*, 2009.

[12] W. C. K. Wong, R. W. K. So and A. C. S. Chung. Principal curves: a technique for preliminary carotid lumen segmentation and stenosis grading. *Midas J*, 2009.

[13] M. A. Zuluaga, M. Orkisz, E. J. F. Delgado Leyton, V. Doré, A. Morales Pinzón and M. Hernández Hoyos. Adaptations of MARACAS algorithm to the

segmentation of the carotid bifurcation and stenosis quantification in CTA images, *Midas J*, 2009.

[14] L. Flórez Valencia, J. Azencot and M. Orkisz. Carotid arteries segmentation in CT images with use of a right generalized cylinder model, *Midas J*, 2009.

[15] C. Florin, N. Paragios and J. Williams. Particle filters, a quasi-Monte-Carlosolution for segmentation of coronaries, *Medical Image Computing andComputer Assisted Intervention (MICCAI)* 8, 246–253, 2005.

[16] Y. Y. Boykov and M. P. Jolly. Interactive graph cuts for optimal boundary and region segmentation of objects in n-D images, *Proceedings of the Eighth IEEE International Conference on Computer Vision (ICCV)*, 1:105–112, 2001.

[17] H. Homann, G. Vesom and J. A. Noble. Vasculature segmentation of CT liver images using graph cuts and graph-based analysis, *Proceedings of the 5th IEEE International Symposium on Biomedical Imaging (ISBI): From Nano to Macro*, 53–56, 2008.

[18] M. Schaap, L. Neefjes, C. T. Metz, A. G. van der Giessen, A. C. Weustink, N. R. A. Mollet, J. J. Wentzel, T. van Walsum, W. J Niessen. Coronary lumen segmentation using graph cuts and robust kernel regression. *Information Processing in Medical Imaging, 5636. Lecture Notes in Computer Science* 528–539, 2009.

[19] M. Freiman, J. Frank, L. Weizman , E. Nammer, O. Shilon and L. Joskowicz, J. Sosna. Nearly automatic vessels segmentation using graph-based energy minimization. *Midas J*, 2009.

[20] M. A. Gulsun and H. Tek. Segmentation of carotid arteries by graph-cuts using centerline models, *Midas J*, 2009.

[21] D. Lesage, E. Angelini, I. Bloch and G. Funka-Lea. A review of 3d vessel lumen segmentation techniques: Models, features and extraction schemes, *Medical Image Analysis* 13 (6), 819 – 845, 2009.

[22] M. Berg, Z. Zhang, A. Ikonen, H. Manninen and R. Vanninen. Carotid stenosisassessment with CT angiography using advanced vessel analysis software, *Computer Assisted Radiology and Surgery (CARS),* 1281: 322–327, 2005.

[23] M. Wintermark, C. Glastonbury, E. Tong, B. C. Lau, S. Schaeffer, J. D. Chien, P. J. Haar and D. Saloner. Semi-automated computer assessment of the degree of carotid artery stenosis compares favorably to visual evaluation, *J. Neurol. Sci*. 269(1–2): 74–79, 2008.

[24] K. Hameeteman, M. A. Zuluaga, M. Freiman, L. Joskowicz, O. Cuisenaire, L. Florez Valencia, M. A. Gulsun, K. Krissian, J. Mille, W. C. K. Wong, M. Orkisz, H. Tek, M. Hernandez Hoyos, F. Benmansour, A. C. S. Chung, S. Rozie, M. J. van Gils, L. van den Borne, J. Sosna, P. Berman, N. Cohen, P. Douek, I. Sánchez, M. Aissat, M. Schaap, C. T. Metz, G. P. Krestin,

A. van der Lug, W. J. Niessen and T. van Walsum. Evaluation framework for carotid bifurcation lumen segmentation and stenosis grading, *Medical Image Analysis*, 2011.

[25] T. Chan and L. Vese. Active contours without edges. *IEEE Trans. Image Process,* 10 (2), 266–277, 2001.

[26] M. B. Milwer, L. F. Valencia, M. H. Hoyos, I. E. Magnin and M. Orkisz. Fast-marching contours for the segmentation of vessel lumen in CTA cross-sections, *Conf Proc IEEE Eng Med Biol Soc*, 2007:791-4, 2007.

[27] V. Doré and M. Cheriet. Robust NL-means filter with optimal pixel-wise smoothing parameter for statistical image denoising, *IEEE Trans. Signal Process*, 57 (5), 1703–1716, 2009.

[28] M. Orkisz, L. F. Valencia and M. H. Hoyos. Models, algorithms and applications in vascular image segmentation, *Machine Graph. Vis.,* 17 (1/2):5–33, 2008.

[29] NASCET collaborators. Beneficial effect of carotid endarterectomy in symptomatic patients with high-grade carotid stenosis, *N. Engl. J. Med.* 325 (7), 445–453, 1991.

[30] L. Antiga and D. A. Steinman. Robust and objective decomposition and mapping of bifurcating vessels, *IEEE Trans. Med. Imag*. 23 (6), 704–713, 2004.

[31] G. Taubin, T. Zhang and G. H. Golub. Optimal surface smoothing as filter design, *ECCV '96 Proceedings of the 4th European Conference on Computer Vision*, Volume I.

[32] W. Schroeder, K. Martin and B. Lorensen. Visualization Toolkit: An Object-Oriented Approach to 3D Graphics, *4th edition Kitware*, December, 2006.

3 Segmentation of the Outer Vessel Wall of the Common Carotid Artery in CTA

This chapter is based on:

D. Vukadinović, T. van Walsum, R. Manniesing, S. Rozie, K. Hameeteman, T. T. de Weert, A. van der Lugt and W. J. Niessen. Segmentation of the outer vessel wall of the common carotid artery in CTA, *IEEE Transactions on Medical Imaging*, 2010.

Abstract

A novel method is presented for carotid artery vessel wall segmentation in CTA data. First the carotid lumen is semi-automatically segmented using a level set approach initialized with three seed points. Subsequently, calcium regions located within the vessel wall are automatically detected and classified using multiple features in a GentleBoost framework. Calcium regions segmentation is used to improve localization of the outer vessel wall because it is an easier task than direct outer vessel wall segmentation. In a third step, pixels outside the lumen area are classified as vessel wall or background, using the same GentleBoost framework with a different set of image features. Finally, a 2D ellipse shape deformable model is fitted to a cost image derived from both the calcium and vessel wall classifications. The method has been validated on a dataset of 60 CTA images. The experimental results show that the accuracy of the method is comparable to the interobserver variability.

3.1 Introduction

One of the major causes of death in western world is atherosclerotic disease, which manifests itself as ischemic heart disease and ischemic stroke [1]. Atherosclerosis is a thickening of the arterial wall due to accumulation of atheromatous debris in the tunica intima and media.

In carotid arteries, the main diagnostic criterion to assess the severity of atherosclerotic disease is the degree of stenosis or severity of luminal narrowing. Risk of (recurrent) stroke is related to the severity of stenosis [2]. However, the presence of a large atherosclerotic plaque is not always associated with luminal narrowing [3], which demonstrates that luminal narrowing alone is probably not a reliable marker for atherosclerosis. In addition, studies on carotid atherosclerotic plaque show that plaque morphology and composition are also important in the risk assessment of patients with carotid artery stenosis [4][5].

CT angiography has been shown to be successful in the assessment of luminal narrowing in the carotid artery [6]. The increased resolution in multidetector CT (MDCT) allows for the analysis of carotid atherosclerotic plaque as well as its different components. Accurate quantification of plaque components from CTA data enables the study of the relation between plaque characteristics and clinical events. This could pave the way for improved diagnosis and risk prediction.

The automatic analysis of the carotid atherosclerotic plaque from CTA data is a challenging problem, owing to the limited contrast between the plaque components and the surrounding soft tissue. The most important step towards automatic atherosclerotic plaque quantification is the difficult task of detecting the outer vessel wall boundary, which encloses both the vessel lumen and the atherosclerotic plaque. Once the outer vessel wall is defined and the lumen is segmented, it facilitates the further quantification of plaque, as recent studies have shown that the different plaque components have more or less distinctive ranges of Hounsfield Units (HU) [7][8].

In this paper we propose a new method for outer vessel wall segmentation, which aims at achieving both a high level of automation and a high accuracy. The method consists of four steps (Fig. 3.1). First, the vessel lumen is segmented using a level set approach. Subsequently, using a set of image features, calcium objects which are part of the vessel wall are detected using a GentleBoost framework. Calcium objects classification is used as a preprocessing step for the outer vessel wall segmentation since it is much easier task to deal with and it can improve the accuracy of the segmentation. In the third step pixels are classified as within or outside the vessel, using the same framework. Finally, an ellipsoid is fitted to the image that represents combined result of calcium and vessel classification. The resulting outer vessel wall is quantitatively evaluated on slices along the common carotid artery proximal to the bifurcation. A preliminary version of this approach has previously been presented [9]. Compared to this work, we introduce an

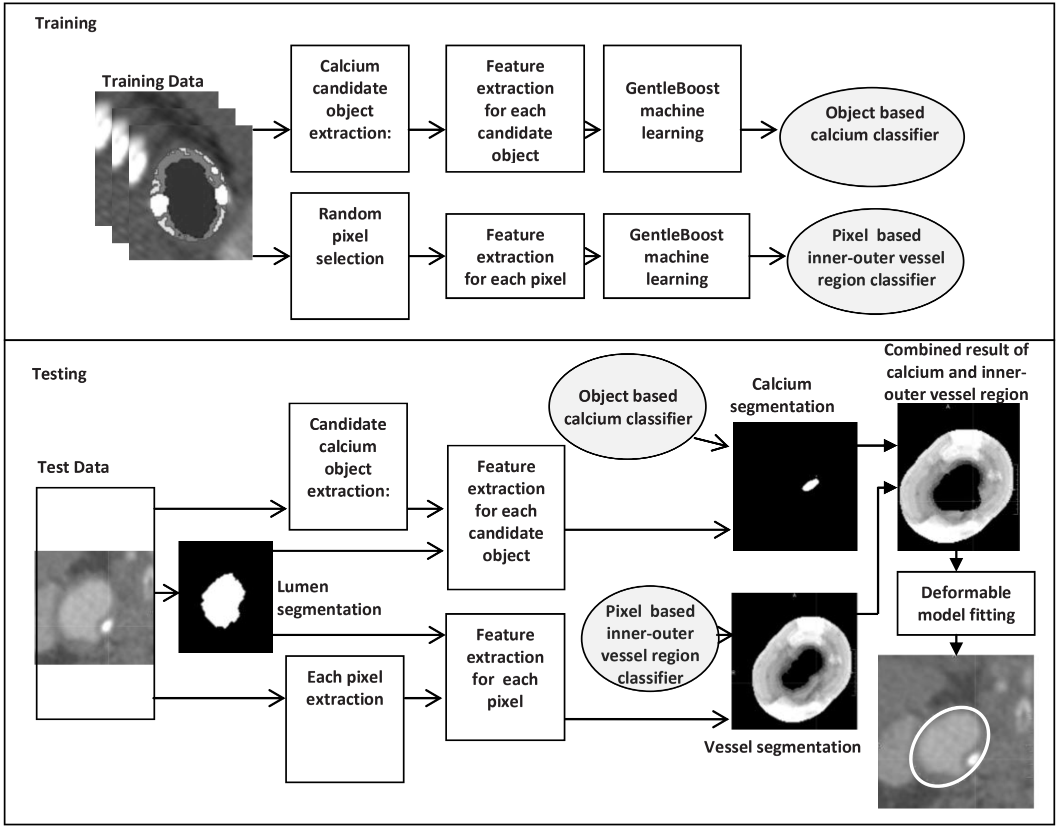

Figure 3.1 Block diagram of the method. Training phase (top) and testing phase (bottom).

improved calcium detection scheme, we improve vessel boundary localization by incorporating Gaussian derivatives features in the inner and outer region of the vessel classification, we improve the model fitting by ensuring spatial continuity along the axial direction, and we perform a more elaborate validation study. The remainder of this paper is organized as follows: in Section 3.2 related work is discussed, followed by a description of the methodology in Section 3.3 Subsequently, in Section 3.4 we describe our experimental setup, including the data sets used, and the evaluation methodology. In Section 3.5 we present the results, followed by a discussion in Section 3.6 and a conclusion in Section 3.7.

3.2 Related Work

Whereas many methods for lumen segmentation have been reported in the literature (e.g. [10-20]), the segmentation of the outer vessel wall has received considerably less attention. Outer vessel wall segmentation of the carotid artery wall in CT is a difficult task owing to the low and varying contrast between the vessel wall and the surrounding tissue (Fig. 3.2), and the large variability in plaque morphology and composition.

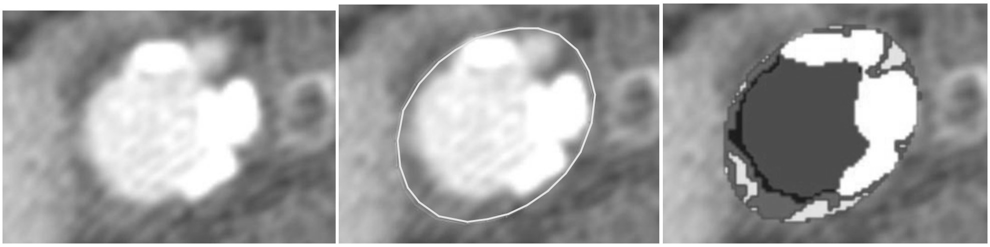

Figure 3.2 Example of a carotid artery CTA scan axial view (left), with contour drawn by a trained observer (center) and with different tissue shown in different colors (right): red – lumen, blue – non-calcified tissue with Hounsfield values (HV) ranging from 130 HU till luminal HU, green – fibrous tissue with HV ranging from 60-130 HU, yellow – lipid with HV ranging from 0-60 HU, white – calcium with HV above 130 HU.

Some authors have addressed the segmentation of the outer vessel wall, both on CTA and MR data. Olabarriaga et al. [21] proposed a deformable model based segmentation of the lumen and thrombus in abdominal aortic aneurysms in CTA data. For the wall segmentation a gray level modeling approach with a KNN classifier using intensity profiles sampled along the surface normal was used.

The active shape model (ASM) based method by De Bruijne et al. [22], [23] also addressed aortic aneurysm segmentation. This method requires a manual delineation of the aneurysm in the first slice after which the contour propagates to the adjacent slices based on grey value similarity. A slice-by-slice control by the user is required.

De Bruijne et al. [24] also proposed a 3D ASM which included a grey level appearance model which was based on non-parametric pattern classification. The user has to draw the top and bottom contours, and indicate the approximate aneurysm centre. Reported results are accurate, but the amount of interaction for initialization is still significant.

A snake based method for defining the vessel lumen and wall boundaries in MR images of the carotid artery was proposed by Yuan et al. [25]. Adams et al. [26] proposed a similar method, deforming two initial contours in MR carotid images. Both methods require a high level of manual interaction. Adame et al. [27] proposed a gradient based ellipse fitting method combined with fuzzy clustering to outline the carotid artery outer vessel wall on MR images. The method requires manual interaction, namely a center point in the lumen, a seed point inside the lipid core and a circle that surrounds the vessel.

The work we present in this paper consists of three stages, i.e. feature extraction, pixel classification, and model fitting, and in this sense it is most similar to the work presented by Olabariaga [21] and De Bruijne [24]. However, in their work the segmentation of thrombus in abdominal aortic aneurysms was considered, and we here address the more challenging problem of automated carotid vessel wall segmentation and quantification in CTA datasets, which, to the best of our knowledge, has not been reported before. In addition, we introduce a separate calcium quantification step in our algorithm. Finally, we applied the GentleBoost framework to determine an optimal set of features, both for calcium detection and vessel wall classification.

3.3 Methodology

The first step of the method is level-set based lumen segmentation, initialized with three seed points: one in the common carotid artery (CCA), one in the internal carotid artery (ICA) and one in the external carotid artery (ECA). For more information on the lumen segmentation method, we refer to the work of Manniesing et al. [20].

Subsequently, we apply a machine learning method that uses spatial location (distance to the lumen), (smoothed) intensity and Gaussian derivative features and a set of size, intensity and shape features for classifying calcium candidate objects. A similar approach is adopted for classifying all pixels as inside or outside the outer vessel wall. Next, the segmentation is obtained by fitting a 2D ellipse to the pixel-based classification result, taking into account the position of previously automatically detected calcified regions and ensuring spatial continuity in the longitudinal direction. Each of the detection and classification steps is described in more detail below.

3.3.1 Calcium Detection

Trained observers strongly rely on the presence and location of calcified regions when manually drawing the vessel wall contour. It is therefore expected that including a separate calcium detection step in our automated processing improves subsequent vessel wall segmentation.

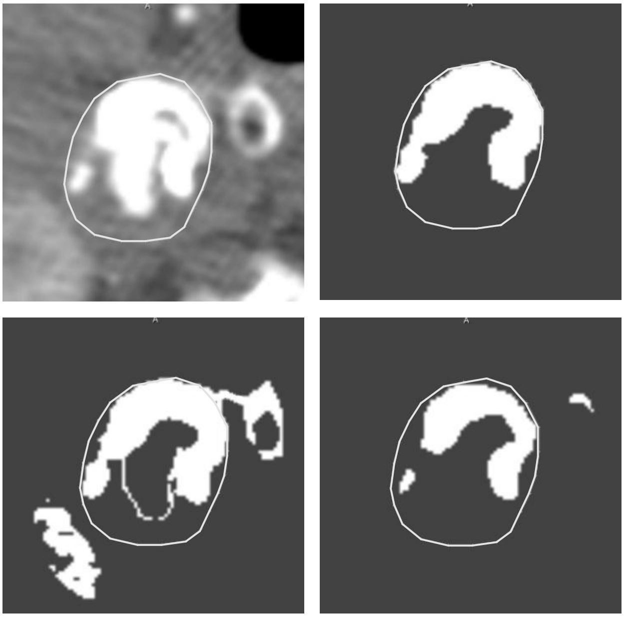

Figure 3.3 Original image with the vessel wall contour drawn by a trained observer (top left), the mask image of true calcium on one slice (top right). Region outside the lumen in the original image on one slice thresholded with th = 130HU (bottom left), and with th = 320 HU (bottom right).

Our automated calcium detection consists of three steps:

1. The extraction of candidate calcium objects.

2. The determination of features for these objects.

3. The classification of the candidate objects as being calcifications or non-calcifications.

3.3.1.1 Candidate Objects Extraction

In clinical practice, calcified regions are commonly characterized as those regions having a density higher than 130 HU [28]. However, in CT angiography, intensity values of the lumen and the tissues surrounding the carotid artery, such as bone structures or the internal jugular vein, may have values larger than 130 HU (Fig. 3.3). A consequence of this is that neighboring high HU regions merge with calcified regions in the process of candidate object extraction. Different threshold values ranging from 80 – 230 HU have been reported in the literature [29]. Isgum et al. in their work on calcium segmentation in contrast-enhanced CT of aorta [30] used 220 HU threshold due to the higher lumen attenuation. T. de Weert et al. [31] for calcium region segmentation in contrast enhanced intracranial carotid artery used threshold of 500 HU in order to separate calcified regions from contrast material in the lumen. In our approach, the lumen has been segmented semi-automatically in a preprocessing step. Still, owing to partial volume effects at too low thresholds calcium candidate objects connect and grow too large (Fig. 3.3). Therefore, on the training set we empirically increased the HU threshold value until this undesired grouping of calcium objects did not occur. Eventually, a threshold value of 320 HU was selected. We also observed that the candidate calcium objects sometimes merged, in the training phase, with the external lumen which is usually not labeled by the observers. Therefore, if for the given dataset the average lumen HU value is higher than 320 HU, the threshold is set to the average intensity value of the lumen.

The ground truth of calcified regions is obtained by the method described in [7] and [8] where thresholding is applied in the region between lumen and vessel wall in order to extract different plaque components, including calcium.

Candidate objects are extracted from the thresholded images by means of connected component analysis, using 18-connectivity in three dimensions [32]. Only clusters of three or more connected voxels are considered valid calcium candidate objects. The objects smaller than 3 voxels are assumed to represent noise. This was confirmed by the training data, where the smallest calcium object had a size of 11 voxels.

3.3.1.2 Object Features

For each candidate object a set of features is calculated. Below we discern between features computed using only the object information and those using both object information and neighboring pixel intensities.

The features selected for the candidate objects were inspired by the work of Isgum at al. [30][33], who included spatial, size, intensity and shape features.

Unlike in the work of Isgum et al., since in our case we have segmented lumen, spatial features are used to describe the position of the object relative to the position of the lumen. We assume the angular position not to be relevant, and therefore we only use the radial distance, which is defined as the shortest distance of the center of the object to the lumen on that slice.

Other features are the volume, the maximum and average intensity value of the object, and a shape feature which describes the compactness of the object:

$$C = \frac{s^3}{36\pi V^2}, \tag{1}$$

where s denotes the surface area of the object and V its volume.

Calcified regions are always inside the vessel wall, i.e. close to both lumen (high intensities) and soft tissue (low intensities) (Fig. 3.4). Therefore, intensities of the neighboring pixels may help in discriminating calcium objects from non-calcium ones. Neighborhood information is included by extracting linear intensity profiles, which are locally oriented radially and tangentially with respect to the lumen. Linear profiles are extracted directly from the original image, from images smoothed with 2D Gaussian filters on multiple scales, and images filtered with oriented 2D Gaussian derivative filters, also on different scales. The oriented Gaussian derivatives were applied in the same direction as the linear profiles (Fig. 3.4). The first derivative of the Gaussian filter in the direction φ and at scale σ is obtained by convolving with the appropriate derivatives of the Gaussian G_σ:

$$\left(\frac{\partial I}{\partial \phi}\right) = (\vec{r} \cdot \nabla) G_\sigma * I, \tag{2}$$

where

$$\vec{r} = (cos\phi, sin\phi). \quad (3)$$

From each image tangential and radial profiles are extracted. Both profiles are 21 pixels long and one pixel, center of mass of calcium object, is common for both profiles. That means that from the original image 41 pixels are extracted, each representing one feature. The same number of features is extracted from the first derivative image computed using a differential operator. Additionally, 41 features per image are extracted from zeroth and first order Gaussian filtered derivative images at scales 1, 2, and 3 pixels which makes additional 41x6 = 246 features. Five additional features are distance from the lumen center, maximum and average intensity value of the object, object volume and shape. This makes 333 features to describe one calcium candidate object.

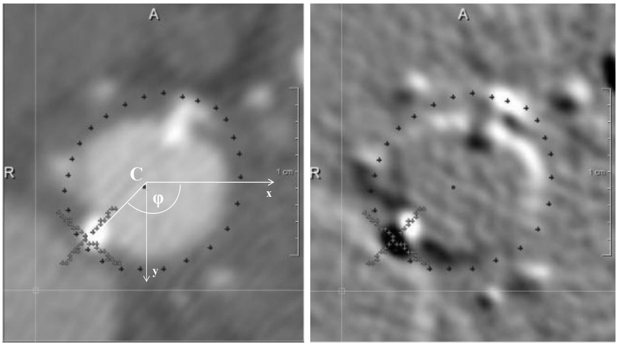

Figure 3.4 Radial profile connecting the lumen center (C) with the center of mass of a calcium object, and the tangential linear profile drawn on the original image (left). The same profiles are also drawn on the first derivative image calculated in the direction connecting center of lumen and center of mass of the calcium object.

3.3.1.3 Candidate Object Classification

Since computation of the complete feature set for all calcium candidate objects is computationally expensive, and there probably is redundancy in the feature set, a boosting [34] method known as GentleBoost [35] is applied to select and combine a set of features which best discriminates between calcium and non-calcium objects. The main difference between AdaBoost and GentleBoost is the way in which the estimates of the weighted class probabilities are used to update the regression function [35]. GentleBoost is assumed to converge faster than AdaBoost [35], is simple to implement and numerically robust. In our application, especially for the classification between the inner and outer vessel region, there is a significant overlap for most features (Fig. 3.5). Performance of boosting methods on data which are generated by classes that have a significant overlap, in other words, classification problems where even the Bayes optimal prediction rule has a significant error has been discussed in [35]. It was concluded that in these cases GentleBoost performs better than AdaBoost since AdaBoost over-emphasizes the atypical examples, which eventually results in inferior rules.

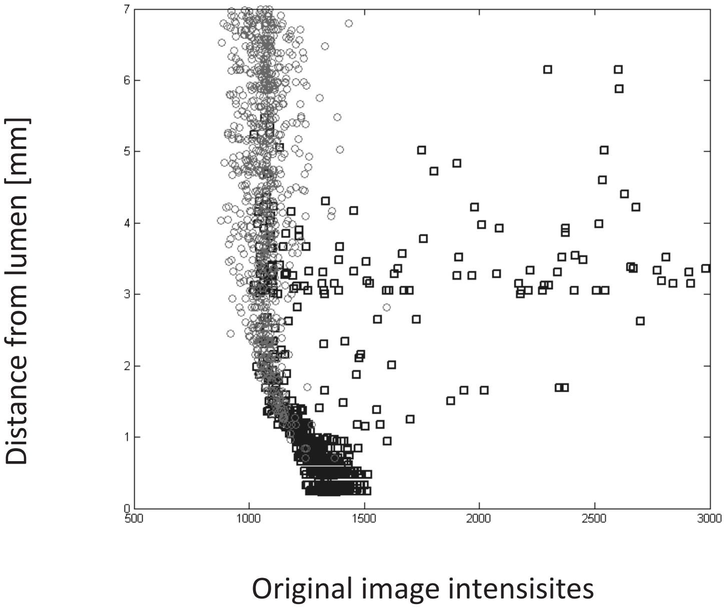

Figure 3.5 Training samples from the inner – outer vessel region classification plotted in the feature space where the axes are the two best discriminating features for classification (see Table V). 800 positive (squares) and 800 negative (circles) samples are randomly chosen from the training set (set I).

The outline of GentleBoost algorithm is presented in Algorithm 4 in Friedman et al. [35]. Boosting methods build "strong" classifiers from a combination of "weak" classifiers (learners). In the case of GentleBoost it is common to use simple functions such as regression stumps (e.g. [35-37]) as weak learners. A regression stump is a two-terminal nodes decision tree that selects a branch for a given feature according to a threshold using a binary decision function. In this way “axes parallel” linear decision boundaries are produced. Friedman et al. [35] performed a simulation study in which they compared GentleBoost performance using stumps and more complex decision trees as weak learners. The conclusion was that for the two classes problem stumps outperform more complex decision trees as a base classifier.

The weak stump classifier used in m-th round is given in this form:

$$f_m(x) = a_m \cdot (x(m) > th_m) + b_m\,, \tag{4}$$

where a_m, b_m and th_m are regression parameters and $x(m)$ is the feature of the test sample x that is chosen in the m-th training round as the most discriminative one. The decision rule for test sample x is given by:

$$F(x) = sign\left[\sum_{m=1}^{M} f_m(x)\right], \tag{5}$$

where M is the number of GentleBoost training rounds.

3.3.2 Inner-Outer Vessel Region Classification

In order to classify the image into two regions, inside and outside the vessel wall, we apply the same method as for calcium classification, albeit with different features. Furthermore, the classification is pixel-based, whereas for calcium segmentation the classification was object-based.

3.3.2.1 Feature Selection

Similar to the calcium case, the distance of each sample to the lumen and contextual features are considered. For representing contextual information, radial image intensity profiles, emanating from the lumen center were considered, similar to [21][22]. Profiles are extracted from the original image, images smoothed with 2D Gaussian filters at different scales, and directional 2D Gaussian derivatives, also at different scales.

Whereas GentleBoost is computationally a very cheap method, in case of pixel based classification, the testing phase can become computationally expensive if the number of features becomes very large. Therefore the sampling rate along the radial profiles is adapted to the scale of the applied Gaussian filters. The finest resolution uses the original image intensities and a profile samples spacing of one pixel. The next resolution level the image is convolved with a

Gaussian kernel with a width of one pixel and a sample spacing of two pixel; subsequent resolutions are obtained by doubling both the kernel width and the sample spacing (see Fig. 3.6).

From each image, pixels are extracted along radial profiles. The first 18 features are 9 pixels extracted from the original image (Fig. 3.6, top left) and 9 pixels extracted from the first derivative image calculated by applying the differential operator. Ten additional features are extracted from the zeroth and first derivative computed at a scale of 1 pixel (Fig. 3.6, top right and bottom right). Finally, six more features are extracted from the zeroth (Fig. 3.6, bottom left) and first derivative calculated at a scale of 2 pixels. Together with the distance to the vessel lumen, this makes 35 features.

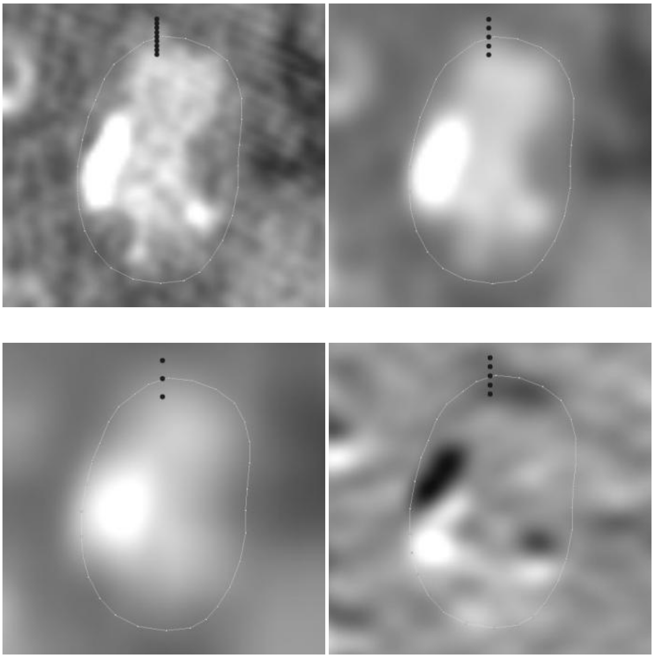

Figure 3.6 One sample positioned on the vessel wall and features describing it: Original image and linear profile of length 9 pixels (top left), image smoothed with a Gaussian kernel of width one pixel and sampled with a spacing of two pixels (top right), image smoothed with a Gaussian kernel of width two pixels and sampled with spacing of four pixels (bottom left) and first derivative of image smoothed with Gaussian kernel of width one pixel with the linear profile with sampling distance equal two pixels (bottom right).

GentleBoost classification results in an image h(x) which contains for each position in the image a value stating the confidence with which each pixel is classified as being inside or outside the vessel wall. For h(x)>0, the pixel x is classified as being outside the outer vessel wall contour, for h(x) <0, the pixel is inside the vessel; the confidence of this classification is given by the magnitude |h(x)| (Fig 3.7). The values in the classification image are in the range [-1, 1].

3.3.3 Ellipse Fitting

The third step of the algorithm is to fit the vessel wall contour to the result of the classification. Similarly to the work by Adame et al. [27], we use prior information that the cross-sectional shape of the CCA is roughly elliptic. An ellipse is fitted to each of the classified transversal slices.

The cost image to which the ellipsoid model is fitted is constructed by combining the confidence image constructed in the vessel wall classification (Fig. 3.7) with the position of automatically detected calcified regions. On each slice, if a calcified region is detected, lumen and calcium are connected and h(x) is set to -1 for the pixels in between, i.e. it is highly unlikely that the vessel wall is positioned in between the calcium and lumen. This adapted h(x) is referred to as h'(x) in the remainder of the paper.

In order to find the most optimal ellipsoid, the following cost function C is optimized:

$$C = \frac{1}{n}\sum_{i=1}^{n} |h'(x_i)| \,, \tag{6}$$

where x_i is a sample along the ellipse and n is the number of samples used to create an ellipse. The best ellipse has minimal C value.

The ellipse model contains five degrees of freedom: two diameters (a, b), positions along the x and y axis (x, y), and angle of rotation (θ). An exhaustive search optimization is used to determine the ellipse with minimum cost in the first slice. In every next slice the initial position and search range of ellipse parameters depends on the ellipse parameters in the previous slice. In this way continuity along the axial direction is enforced, while simultaneously improving computation efficiency by restricting the search range for the exhaustive search.

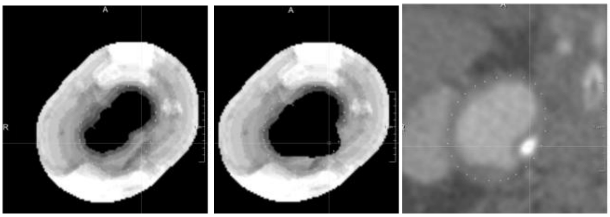

Figure 3.7 Example of a confidence image *h(x)* (left), combination of the confidence image and the detected calcium region *h'(x)*, i.e. cost image for the ellipse fitting (center), corresponding original image with the vessel wall points marked on it (right).

The initial center of the ellipse on the slice $i+1$ is translated in 2D based on the displacement of the lumen center from slice i to slice $i+1$. The range for the angle of rotation θ_{i+1} for the ellipse on the slice $i+1$ depends on the rotation θ_i and the ratio R_i between shorter and longer axis of the ellipse on slice i. The value of the ratio R describes the shape of the ellipse: the closer the R value is to 1.0, the more circular the ellipse is, and the larger the rotation range can be. If the ellipse is stretched in one direction, in the next slice we should limit the possible orientations of the ellipse to that direction, and thus have smaller range for valid values for θ.

The remaining parameters, a, b, x and y depend linearly on the axis sizes in the previous slice ellipse. The exact parameter values used in the experiments are given in Section 3.4.4.3.

3.4 Experimental Setup

3.4.1 Input Data

The CTA data were acquired on a MDCT scanner (Siemens, Sensation 16, Erlangen, Germany), with a standardized optimized contrast-enhanced protocol (120 kVp, 180 mAs, collimation 16_0.75 mm, table feed 12 mm/rotation, pitch 1) and a slice thickness of 1.0 mm and a pixel size of 0.23 mm. More details on scanning protocol are presented in [7]. Only the scans reconstructed with b46 kernel were used in our experiments.

From a database containing 140 CTA carotid arteries from patients with transient ischemic attacks (TIA) symptoms we have selected 85 consecutive datasets. From these 85 datasets, 40 were randomly chosen for training (set I) and 40 were randomly chosen for testing (set II). The remaining 5 were used as

Number of datasets	Name	Description	Observer who drew the ground truth
40	I	Training set	A
40	II	Testing set	A
5	III	Calcium classification optimization set	A
20	IV	Interobserver variability test set	B, C

Table 3.1 Description of datasets used for training, testing and optimization.

an optimization set (set III) in order to determine how many GentleBoost rounds should be used for the calcium objects classification. Additionally 20 more carotid CTA datasets (set IV) were randomly chosen from the 46 datasets used in the interobserver study on carotid artery plaque by de Weert et al. [39]. These 20 datasets were also used for testing, resulting in 60 testing datasets. The datasets from set IV enable us to compare algorithm performance with interobserver variability. The datasets are described in Table 3.1.

Three observers manually annotated contours and these contours are considered to be our ground truth. Observer A is an experienced resident in radiology with two years of experience on CTA and CT plaque analysis. Observer B is an experienced resident in radiology with four years of experience on CTA and CT plaque analysis. Observer C is an experienced CT technologist with two years of experience on CTA and CT plaque analysis.

Contours used in the training phase (set I), testing phase (set II) and in the optimization phase (set III) are drawn by the same observer (A). The contours from the test set IV used for the interobserver variability comparison are drawn by observer B and C.

In all sets (I-IV) used in this work, the contours were drawn on the range of consecutive slices where the vessel wall was thickened. On average, 40 slices per dataset were manually annotated. This usually included CCA and ICA part since in the ECA plaque is rarely present. The evaluation is only performed in the CCA part since in the bifurcation region the elliptic deformable model is not suitable

3.4.2 Experiments Performed

Using the proposed method we trained both the calcium classifier and the inside-outside vessel wall classifier on the 40 datasets in the training set. Vessel wall segmentation was subsequently quantitatively evaluated on the 60 datasets in the test sets II and IV.

3.4.2.1 Calcium Segmentation – Training and Testing

From the training set 347 candidate objects were extracted, 167 true positive and 180 false positive objects. For each candidate object 333 features were calculated.

In the testing phase calcium candidate objects are extracted and the set of features described in the section 3.3.1.2 are calculated for each object. The classifier takes only the features selected in the training phase and based on the value calculated by (11) decides if the candidate object is calcium or not.

We evaluated success of the classification with three criteria: sensitivity, specificity and accuracy.

In our method we use only objects classified as positive (calcium) to change the confidence image $h(x)$ in order to improve the ellipse fitting. Hence, classification of a background candidate object as calcium object will negatively affect segmentation accuracy, and therefore specificity as close as possible to 100% is desired, i.e. no background object should be classified as calcium region.

We first explored how many iterations in the training of the GentleBoost algorithm were needed in order to achieve optimal classification, i.e. we aimed at establishing the minimal number of iterations for the classifier to converge. Hereto, a small optimization set III was randomly selected. This optimization dataset contained 42 candidate objects, 23 calcium and 19 non-calcium objects. Classification performance as function of the number of iterations was performed, and the minimal number of required iterations was determined.

The evaluation on the test datasets II and IV was performed on CCA and ICA with a classifier trained with this number of iterations. The datasets included 432 candidate objects, of which 265 calcium and 167 non-calcium.

3.4.2.2 Vessel Wall Segmentation – Training and Testing

From the training set I 40000 samples (positions in the training images) were randomly selected, 10000 positive samples (inside vessel wall) and 30000 negative samples (outside vessel wall).

Comparable to the calcium classification, the optimal feature set for inner and outer vessel wall classification was determined in the training stage on the training set. Using the resulting optimal classifiers, vessel wall segmentation is quantitatively evaluated on the test set containing 60 datasets. Samples are collected, both for training and testing, in the same region of interest as for the calcium object classification.

The first set of experiments was performed on the 40 datasets in the set II for which one manually annotated vessel wall is drawn by observer A, who also drew the ground truth contours in the training set I on which our method was trained. We investigated whether using Gaussian (derivative) features in addition to intensities increased the accuracy of vessel wall detection. Therefore, next to the classifiers trained with all features as described in Section 3.3.2, we used a classifier which was only trained using features extracted from the original image.

In a second experiment the best performing classifier was applied to the set IV. In this set we compared the success of our method to the inter observer variability.

3.4.3 Evaluation Measures

In order to compare different outer vessel wall segmentations, we use two measures. The first measure is the Dice coefficient or similarity index *SI*, which measures the similarity of two segmentations:

$$SI = \frac{2|X \cap Y|}{|X| + |Y|}, \tag{7}$$

where *X* and *Y* denote the regions inside the contour. This measure relates the over- and undersegmentation to the size of the object to segment.

The second measure is the absolute average distance between the contours, expressed in millimeters. Both the average error measure per dataset (E_d) and per contour ($E(k)$) are determined, where the average error per contour is defined as

Parameter	Range	Discretization Step
Diameter a	[minLumenRadius + 2mm, maxLumenRadius+2mm]	0.46 [mm]
Diameter b	[a, maxLumenRadius+2mm]	0.46[mm]
Translation x	[-0.94, 0.94]	0.46[mm]
Translation y	[-0.94, 0.94]	0.46[mm]
Orientation θ	[0,180] [deg]	5[deg]

Table 3.2 Parameters of ellipse fitting using exhaustive search. The range and stepsize of the ellipse parameters on the first slice, on which an exhaustive search is performed.

$$E(k) = \frac{\sum_{i=0}^{N} S(i)}{N}, \tag{8}$$

with *S(i)* is the minimum Euclidian distance between position *i* along the ground truth c ontour (defined by *N* points) and the ellipse.

Differences in measures between classification methodologies were tested with Wilcoxon's matched pairs signed rank test [40]

3.4.4 Parameters Values

3.4.4.1 Calcium Segmentation

In the calcium classification experiments the following parameter settings were used: the length of the linear profile was set to 21 pixels (4.92 mm) and the sampling distance is one pixel (0.23 mm). The profile length we assumed to be large enough to capture all relevant neighborhood information since the maximum calcium object diameter in our dataset was 4.6 mm long. Candidate objects were selected by thresholding in a region within 8 mm from the lumen boundary. This range was selected since in the entire dataset the vessel wall was never further away than 7.1 mm.

3.4.4.2 Vessel Wall Segmentation

For the vessel wall profile a length of 9 pixels (2.1mm) was used. Training and testing samples were extracted from a region of interest within 8 mm from the lumen boundary.

Parameter	Range[mm]	Discretization step[mm]
Diameter a	$[0.875 \cdot a_{PreviousSlice}, 1.125 \cdot a_{PreviousSlice}]$	0.23
Diameter b	$[0.875 \cdot b_{PreviousSlice}, 1.125 \cdot b_{PreviousSlice}]$	0.23
Translation x	[-0.23, 0.23]	0.23
Translation y	[-0.23, 0.23]	0.23

Table 3.3 Parameters of ellipse fitting using non-exhaustive search. The range and discretization steps of the ellipse parameters for the exhaustive search with restricted search range in the adjacent slices. The values of the ellipse parameters depend on the ellipse parameters from the previous slice.

3.4.4.3 Ellipse Fitting Parameters

Ellipse fitting was performed on the image *h'(x)* as described in Section 3.3.3. In the first slice an exhaustive search strategy was used, while in all consecutive slices information from the adjacent slice was used. Table 3.2 shows the range and discretization of the ellipse fitting parameters used in the first slice. As the processing starts at the proximal end of the carotid, far away from the bifurcation, with hardly any plaque burden, we chose the initial maximum ellipse diameter to be only slightly (2 mm) larger than the maximum lumen diameter on that slice. In all other consecutive slices an exhaustive ellipse fitting search with restricted parameters range was performed. The parameters values for this fitting process are listed in Table 3.3.

In case the optimal ellipse still crosses a calcified region, a new fit was started, with a larger search range for the position of the ellipse center. The ellipse center translation range in this case in x and y direction is $[-0.25 \cdot d_i, 0.25 \cdot d_i]$ where d_i is the larger diameter of the extracted ellipse in the previous slice i.

3.5 Results

3.5.1 Calcium Objects Classification

In Fig. 3.8 sensitivity, specificity and accuracy of calcium object classification as a function of number of iterations used in the GentleBoost algorithm are shown. After 20 iterations the graphs converge, and specificity has reached 100%, while accuracy and sensitivity were 94% and 90% respectively. Therefore, in the remainder of the experiments we used those 20 weak classifiers *f* for classification. A sensitivity as close as possible to 100% is of importance, as it implies that the model fitting part of our method is only improved by the calcium detection and in no test case degraded by the misclassification of the background objects. The first four features which are the most important for the calcium classification are shown in the Table 3.4.

The training samples in the feature space of the first two features are shown in Fig. 3.9.

Feature description	th	a	b	error
Distance from lumen [mm]	2.59	1.86	-0.91	0.13
0-derivative, scale = 0.69mm, radial profile	$1.27\ 10^3$	-1.60	0.88	0.36
Max intensity	$1.6\ 10^3$	-1.13	0.68	0.68
0-derivative, scale = 0.23mm, radial profile	$1.2\ 10^3$	1.08	-0.57	0.70

Table 3.4 Four most discriminative calcium object features. *th*, *a*, and *b* are the parameters of Gentle Boost classifier described in (4). The error parameter is the classification error on the training set when only the considered feature is used.

Calcium detection in 60 datasets of set II and set IV in CCA and ICA, performed with the twenty features selected in the training experiment as a preprocessing step for vessel wall segmentation, also yielded good classification results. We achieved very high values for all measures: sensitivity of 93%, specificity of 99% and overall accuracy of 95%. In the CCA specificity was 100%.

3.5.2 Vessel Wall Segmentation

The four most relevant features for inner-outer vessel region classification are shown in Table 3.5.

To illustrate the degree of overlap between the classes 800 randomly selected positive and 800 randomly selected negative samples are plotted in the feature space spanned by the first two features from Table 3.5 (Fig. 3.5). It is clear that the problem to classify inner and outer region of the vessel is much harder than calcium – non-calcium object classification (Fig. 3.9).

3.5.2.1 Influence of Using Gaussian Zeroth and First Order Derivative

Feature description	th	a	b	error
Distance from lumen [mm]	1.30	1.65	-0.78	0.27
Original image	$1.27\ 10^3$	-1.21	0.54	0.47
0-derivative, scale = 0.23mm	$1.05\ 10^3$	-0.93	0.87	0.59
0-derivative,scale = 0.46mm,	$1.34\ 10^3$	-0.85	0.08	0.73

Table 3.5 Four most discriminative inner – outer vessel region features. *th*, *a*, and *b* are the parameters of Gentle Boost classifier described with equation (4). The error parameter is the classification error on the training set when only the considered feature is used.

Vessel wall classification using Gaussian and intensity features was compared with classification using only intensity features on the set II. In Fig. 3.10, similarity indices (6) are given and Fig. 3.11 shows the average wall localization error in mm (7). For all datasets our method using Gaussian features and intensity features was better than the approach that uses intensity features only. The similarity indices and segmentation errors are listed in the Table 3.6.

From the Table 3.6 we can see that the similarity index improved from 88.5±3.3 % in the case where only intensity features were used to 91.3 ± 2.6 % when in addition the Gaussian derivatives features were used ($p<0.0001$). In addition, the segmentation error E_d, reduced from 0.58±0.18 mm^3 to 0.43±0.13 mm^3 ($p<0.0001$).

The first two rows of Fig. 3.12 show results on three consecutive slices from two of the datasets presented in Fig. 3.10 and Fig. 3.11.

3.5.2.2 Segmentation Accuracy versus Interobserver Variability

The similarity indices and segmentation error between the method's results and the two manual tracings of the observers, and between two observers are shown in Fig. 3.13 and Fig. 3.14, respectively.

In Table 3.7 the average values of the similarity index and segmentation error over the 20 datasets are listed. From Fig. 3.13 and 3.14 it can be observed that the interobserver error and the interobserver similarity index have the same order of magnitude as the difference between our method and the observers. It can also be seen that the performance of our method is slightly better when compared to observer B than observer C. The difference between the error of our method and the inter observer variability error, albeit small, is statistically significant (p=0.047 for observer B and p=0.004 for observer C). The difference between similarity index between our method and observers and the similarity index between two observers is not statistically significant (p=0.067) for observer B, but it is significant for observer C (p=0.004).

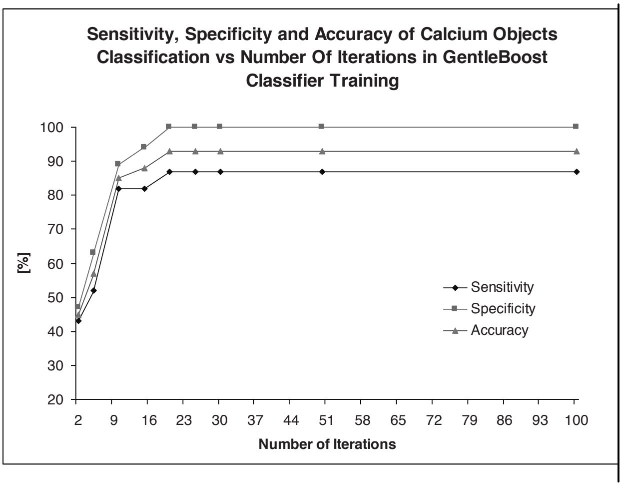

Figure3.8. Sensitivity, specificity and accuracy of the calcium candidate object classification as a function of number of iterations performed during training of the classifier. The test is performed on the 5 carotid arteries from the optimization set (set III).

The last two rows of Fig. 3.12 show results on three consecutive slices from two of the datasets in Fig. 3.13 and Fig. 3.14.

Method	μ (SI) ± std. dev [%]	SI [min, max]	μ (E_d) ± std. dev [mm]	E_d [min, max]
With Gaussian and intensity features	91.3 ± 2.6	[84.4, 95.3]	0.43±0.13	[0.22, 0.82]
With only intensity features	88.5±3.3	[80.0, 93.1]	0.58±0.18	[0.39, 1.15]

Table 3.6 Similarity index and segmentation error on 40 scans. Similarity index and average segmentation errors, E_d, with standard deviations for all 40 datasets (set II).

Comparison	μ (SI) ± std. dev [%]	SI [min, max]	μ(E_d) ± std. dev [mm]	E_d [min, max]
Our method – Observer B	90.5 ± 2.8	[83.2, 94.9]	0.48±0.14	[0.32, 0.93]
Our method – Observer C	89.8±3.1	[82.1, 93.6]	0.53±0.17	[0.31, 1.05]
Observer B – Observer C	92.1±3.1	[84.4, 95.4]	0.42±0.16	[0.22,0.88]

Table 3.7 Similarity index and segmentation error on 20 scans. Average similarity index and average segmentation errors, E_d, with standard deviations for all 20 datasets where comparison with the inter observer error is done (set IV).

3.6 Discussion

We presented and evaluated a new method for outer vessel wall segmentation, which is based on a combination of pixel-based classification and deformable model fitting.

First, candidate calcium objects are extracted and classified based on their features. Since calcium regions usually follow the shape of the outer vessel wall, next to candidate object intensity, volume, and shape features, both radial and tangential linear profiles have been included as features. In a feature selection phase, it was found that these profiles are very relevant in the classification process; next to features extracted from the radial and tangential profiles only distance from the lumen and maximum intensity of the candidate object are important for the classification success. The most relevant feature is the spatial position of the object relative to the lumen. This is not surprising given that the calcified regions are positioned very close to or touching the lumen boundary. Other features which best discriminate calcium and non-calcium objects are the zeroth and first order Gaussian derivative of the radial intensity profile. Object volume only appears in one of the last iterations while shape information is not selected in any iteration. In previous work, Isgum et al. [33] also found that calcium shape and size features were not relevant in the detection of coronary calcifications. Our method for candidate object extraction may have affected the relevance of the shape and size features. As it is shown in Fig. 3.3, candidate objects represent in most of the cases only a part of the complete calcified region. This is due to the fact that in CTA data a higher HU threshold needs to be used than in non-contrast enhanced CT, to prevent contrast-enhanced veins to merge with the calcified regions. Shape information that may be discriminative between calcium and non-calcium objects is potentially lost owing to this undersegmentation. Average object intensity is also shown not to be relevant for calcium classification, whereas maximum intensity is one of the most relevant features.

Whereas calcium classification achieved high specificity (99%), and sensitivity (93%), vessel wall segmentation can still be further improved by improving calcium classification. The second row of Fig. 3.12 shows an example where one calcium object is detected (left from the lumen) and the second one (under lumen) is not. It is clear that the vessel wall segmentation error would have been considerably smaller if both calcium objects would have been detected. False positive classification did not negatively influence the results, as the specificity of calcium detection is very high with only one background object classified as calcium. This did not have influence on the outer vessel wall segmentation since the misclassified object was located in the region of ICA, i.e. above the bifurcation.

To classify pixels to belong to the inner or outer vessel region we applied the same classification framework with a different set of features. Voxel based classification was used and features were extracted from radial profiles. Distance from the lumen was the most informative feature. A comparison study using only original intensity profiles and using additional profiles filtered with Gaussian filters and directional Gaussian derivatives showed that the use of Gaussian features outperforms the approach using intensity features only. We do not only add Gaussian blurring, but also Gaussian derivative features, which improves edge localization. The combination of these two groups of features improves the overall result.The difference between our method and both observers is in the same range as the interobserver variability. The average distance over 20 datasets from the set IV of our method compared to the observer B as the ground truth is 0.48 mm, and compared to observer C 0.53 mm, while the inter observer variability (between observer B and C) is 0.42 mm. The difference of 0.06 mm and 0.11 mm correspond to one quarter and one half of a pixel size respectively. The Wilcoxon test shows that the inter observer error is not significantly different compared to the error between automated segmentation and observer B. On the other hand, the error of our method compared to the observer C, albeit small, is statistically significantly different from the interobserver error.

The data we used for training and testing consisted of a consecutive set of data acquired in our hospital, and was very diverse with respect to pathology (degree of stenosis, degree of calcifications). Therefore the training and evaluation sets were representative for the variability that occurs in clinical practice.

Our algorithm is shown to be very robust when tested on a large dataset. This is a promising result with respect to the applicability in clinical practice. As described in the work of De Weert et al. [7,8], having a lumen and outer vessel wall contour is sufficient in order to characterize three main plaque components (lipid, fibrous tissue and calcium) with an accuracy comparable to histology, which shows the large potential of the approach to be used in clinical practice for plaque characterization. There are, however, still a number of limitations. Our current algorithm is primarily slice based. Only calcium object detection is performed in 3D, and the other 3D aspect of the algorithm is that ellipse fitting part relies on the ellipse fitting results of the neighboring slices. Another current limitation is that it assumes an elliptical cross section of the carotid artery; this assumption does not always hold in the small region around the bifurcation. Future work will therefore be directed to fitting more flexible 3D models to the classification results.

3.7 Conclusion

We have presented a method for the segmentation of the carotid outer vessel wall in CTA scans, which combines classification of previously extracted calcium objects and inner-outer vessel wall region with a parametric vessel shape model.

The method has been evaluated on a dataset of 60 CTAs of the carotid arteries.

The average similarity index between vessels segmented by our method and the vessels segmented by experienced observers was 91% and comparable to the similarity index between two observers.

The results are highly encouraging with respect to the plaque quantification in medical practice.

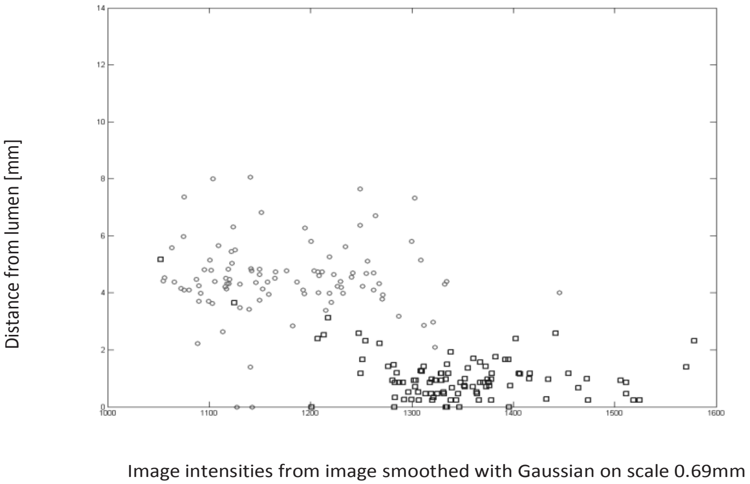

Figure 3.9. Calcium objects samples plotted in the features space, where the axes are the two most discriminating features for classification, see table 3.4. 100 positive (squares) and 100 negative (circles) samples randomly chosen from the training set (set I) are plotted.

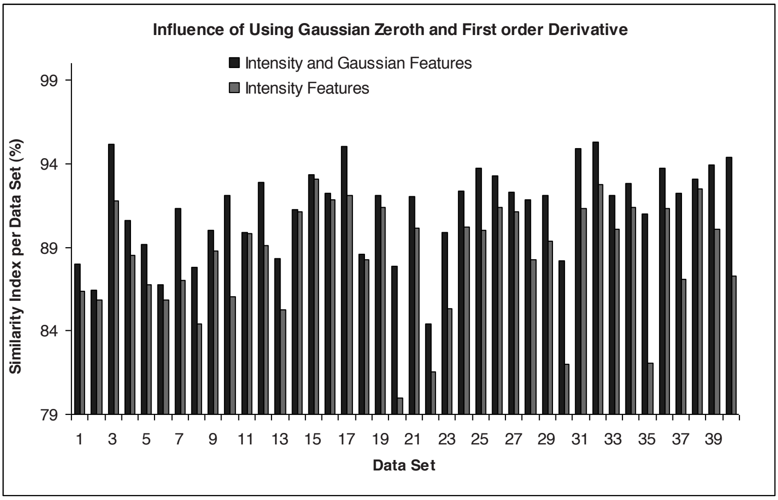

Figure 3.10 Similarity indices (according to equation (7)) for the vessel segmentation using intensity and Gaussian features (first column) and using only the features extracted from the original image (second column). The test is performed on the 40 carotid arteries (set II).

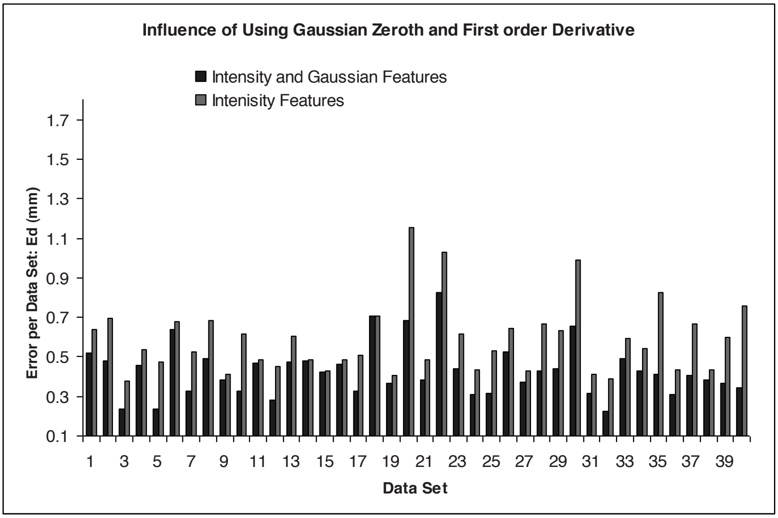

Figure 3.11 Segmentation errors (according to equation (8)) for the vessel segmentation using intensity and Gaussian features (first column) and for the classifier using only features extracted from the original image (second column). The test is performed on the 40 carotid arteries (set II).

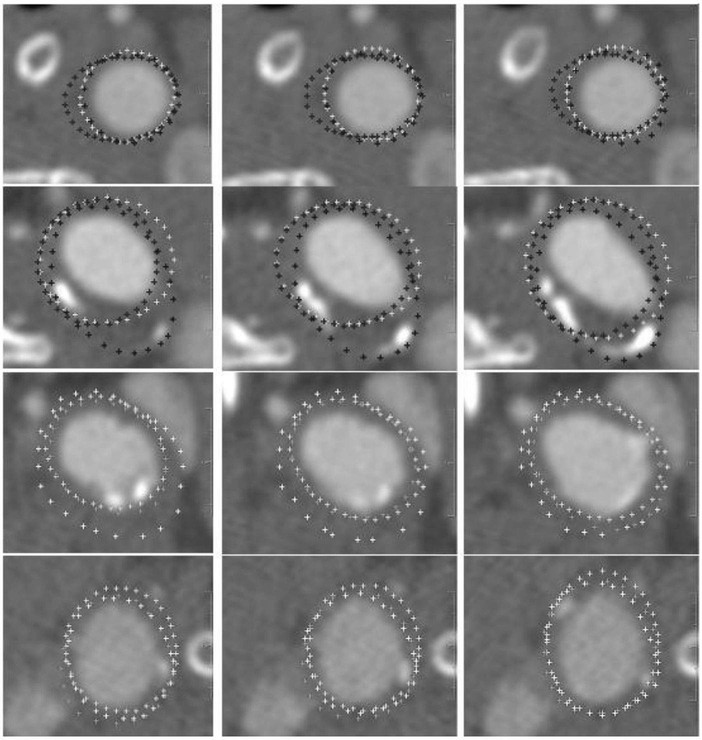

Figure 3.12 Examples of vessel wall segmentation results. In all rows three consecutive slices of one dataset are shown. Yellow markers represent our method using Intensity and Gaussian Features, red markers represent the same method with Intensity Features only, blue markers represent the ground truth drawn by observer A, orange markers represent the ground truth drawn by observer B, and white markers represent the ground truth drawn by observer C. Top row: dataset 30 from figures 10 and 11 is presented illustrating that Gaussian features improve the segmentation. Second row: an example with high error which would be significantly reduced if misclassified calcium region (bottom left) was correctly classified as calcium - dataset number 22 from figures 10 and 11 is shown. In the third row dataset number 9 from figures 13 and 14 is shown. This is an example of our segmentation almost overlapping with the ground truth drawn by observer B, while making a big error compared to the observer C. In the bottom row dataset number 13 from figures 13 and 14 is shown. This is an example where error of our segmentation is very similar to the inter observer error and our segmentation is very similar to contours drawn by both observer B and observer C.

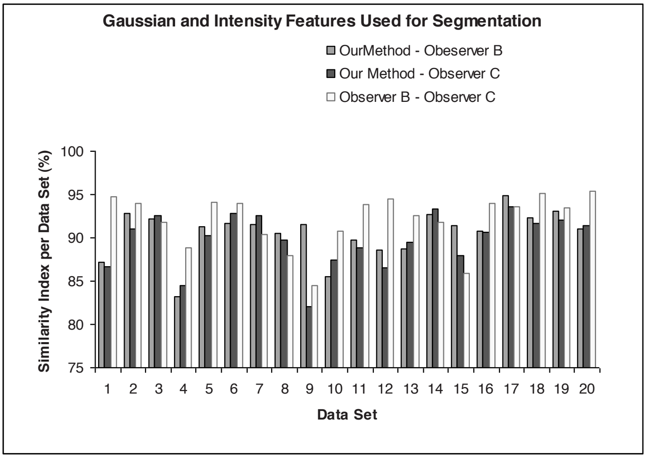

Figure 3.13 Similarity Index calculated as in (7) for three cases: our method with Gaussian and Intensity features used for the wall classification compared with the ground truth from observer B and observer C and comparison between two observers. The test is performed on the 20 carotid arteries where two observers (B and C), drew the ground truth (set IV).

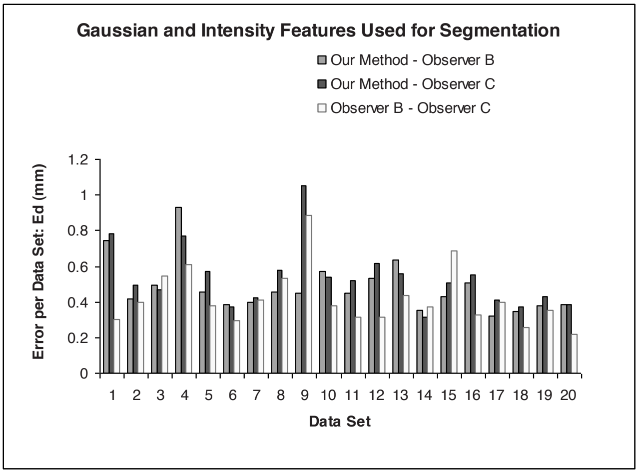

Figure 3.14 Wall segmentation errors according to (8) for our method using Gaussian and Intensity features compared with the ground truth from the observer B and observer C, and comparison between two observers. The test is performed on the 20 carotid arteries for which reference contours by observers B and C were available (set IV).

3.8 References

[1] M. Robins and H. M. Baum. The national survey of stroke: Incidence, *Stroke*, 12: I 45–I57, Mar. - Apr.1981.

[2] North American symptomatic carotid endarterectomy trial collaborators. Beneficial effect of carotid endarterectomy in symptomatic patients with high-grade carotid stenosis, *N. Engl. J. Med.*, 325(7):445-453, Aug. 1991.

[3] S. Glagov, E. Weisenberg, C. K. Zarins, R. Stankunavicius and G. J. Kolettis. Compensatory enlargement of human atherosclerotic coronary arteries, *N Engl J Med*, 316(22): 1371–1375, May 1987.

[4] P. M. Rothwell, R. Gibson and C. P. Warlow. Interrelation between plaque surface morphology and degree of stenosis on carotid angiograms and the risk of ischemic stroke in patients with symptomatic carotid stenosis, *Stroke*, 31(3): 615–621, Mar 2000.

[5] J. K. Lovett, P. J. Gallagher, L. J. Hands, J. Walton and P. M. Rothwell. Histological correlates of carotid plaque surface morphology on lumen contrast imaging, *Circulation*, 110(15): 2190–2197, Oct 2004.

[6] M. J. W. Koelemay, P. J. Nederkoorn, J. B. Reitsma and C. B. Majoie. Systematic review of computed tomographic angiography for assessment of carotid artery disease, *Stroke*, 35(10): 2306–2312, 2004.

[7] T. T. de Weert, M. Ouhlous, E. Meijering, P. E. Zondervan, J. M. Hendriks, M. R. H. M. van Sambeek, D. W. J. Dippel and A. van der Lugt. In vivo characterization and quantification of atherosclerotic carotid plaque components with multidetector computed tomography and histopathological correlation, *Arterioscler. Thromb. Vasc. Biol.*, 26(10): 2366–2372, Oct 2006.

[8] T. T. de Weert, M. Ouhlous, P. E. Zondervan, J. M. Hendriks, D. W. J. Dippel, M. R. H. M. van Sambeek and A. van der Lugt. In vitro characterization of atherosclerotic carotid plaque with multidetector computed tomography and histopathological correlation, *Eur. Radiol.*, 15(9): 1906–1914, Sep 2005.

[9] D. Vukadinović, T. van Walsum, R. Manniesing, A. van der Lugt, T. T. de Weert and W. J. Niessen. AdaBoost classification for model based segmentation of the outer vessel wall, *Proc. SPIE Medical Imaging*, 6914, 2008.

[10] C. M. van Bemmel, M. A. Viergever and W. J. Niessen. Semi-automated segmentation and stenosis quantification of 3D contrast-enhanced MR angiograms of the internal carotid artery, *Magnetic Resonance in Medicine*, 51(4):753 – 760, Mar. 2004

[11] H. Scherl, J. Hornegger, M. Prümmer and M. Lell. Semi-automatic level-set based segmentation and stenosis quantification of the internal carotid artery in 3D CTA data sets, *Med. Image Anal.*, 11(1): 21–34, Feb 2007.

[12] T. Boskamp, D. Rinck, F. Link, B. Kuemmerlen, G. Stamm and P. Mildenberger. A new vessel analysis tool for morphometric quantification and visualization of vessels in CT and MRI datasets, *Radiographics*, 24*:* 287-277 (2004).

[13] L. M. Lorigo, O. D. Faugeras, W. E. L. Grimson, R. Keriven, R. Kikins, A. Nabavi and C. F. Westin. CURVES: Curve evolution for vessel segmentation, *Med. Image Anal.*, 5(3): 195-206, Sep. 2001.

[14] A. Frangi, W. J. Niessen, P. Nederkoorn, J. Bakker, W. Mali and M. Viergever. Quantitative analysis of vascular morphology from 3D MR angiograms: In vitro and in vivo results, *Magnetic Resonance in Medicine*, 45(2): 311–322, Jan. 2001.

[15] S. Aylward, S. Pizer, E. Bullitt and D. Eberl. Intensity ridge and widths for tabular object segmentation and registration, *Workshop on Mathematical Methods in Biomedical Image Analysis*: 131–138, 1996.

[16] T. F. Chan and L. A. Vese. Active contours without edges, *IEEE Trans. on Image Processing,* 10(2): 266-277, Feb. 2001.

[17] P. J. Yim, P. L. Choyke and R. M. Summers. Gray-scale skeletonization of small vessels in magnetic resonance angiography, *IEEE Trans. on Med. Imag.*, 19: 568–576, June 2000.

[18] A. K. Klein, F. Lee and A. A. Amini. Quantitative coronary angiography with deformable spline models, *IEEE Trans. on Med. Imag.*, 16: 468–482, Oct. 1997.

[19] P. Yan and A. A. Kassim. Segmentation of volumetric MRA images by using capillary active contour, *Med. Image Anal.*, 10(3): 317-329, Jun 2006.

[20] R. Manniesing, B. K. Velthuis, M. S. van Leeuwen, I. C. van der Schaaf, P. J. van Laar and W. J. Niessen. Level set based cerebral vasculature segmentation and diameter quantification in CT angiography, *Med. Image Anal.*, 10(2): 200-214, Apr. 2006.

[21] S. D. Olabarriaga, J. M. Rouet, M. Fradkin, M. Breeuwer and W. J. Niessen. Segmentation of thrombus in abdominal aortic aneurysms from CTA with non-parametric statistical grey level appearance modelling, *IEEE Trans. on Med. Imag.*, 24(4): 477 - 485, Apr. 2005.

[22] M. de Bruijne, B. van Ginneken, W. J. Niessen, M. Loog and M. A. Viergever. Active shape model based segmentation of abdominal aortic aneurysms in CTA images, *SPIE Medical Imaging, ser. Proc. of the SPIE*, 4684: 463–474, 2002.

[23] M. de Bruijne, B. van Ginneken, M. Viergever and W. J. Niessen. Interactive segmentation of abdominal aortic aneurysms in CTA data, *Med. Image Anal.*, 8(2): 127–138, 2004.

[24] M. de Bruijne, B. van Ginneken, M. Viergever and W. J. Niessen. Adapting active shape models for 3D segmentation of tubular structures in

medical images, *Information Processing in Medical Imaging*, ser. LNCS, 2732. Springer: 136–147, 2003.

[25] C. Yuan, E. Lin, J. Millard and J. N. Hwang. Closed contour edge detection of blood vessel lumen and outer wall boundaries in black-blood MR images, *Magn. Reson. Imaging*, 17(2: 257-266, Feb. 1999.

[26] G. J. Adams, G. W. Vick, C. B. Bordelon, W. Insull and J. D. Morrisett. An algorithm for quantifying advanced carotid artery artherosclerosis in humans using MRI and active contours, *Proc. SPIE Medical Imaging*, 4684: 1448-1457, 2002.

[27] I. M. Adame, R. J. van der Geest, B. A. Wasserman, M. A. Mohamed, J. H. C. Reiber and B. P. F. Lelieveldt. Automatic segmentation and plaque characterization in atherosclerotic carotid artery MR images, *MAGMA*, vol 16(5): 227 – 234, Apr. 2004.

[28] P. Gayard, J. M. Garcier, J. Y. Boire, A. Ravel, N. Perez, C. Privat, P. Lucien, J. F. Viallet and L. Boyer. Spiral CT quantification of aorto-renal calcification and its use in the detection of atheromatous renal artery stenosis: A Study in 42 Patients, *CardioVascular and Interventional Radiology*, vol 23(1: 17-21, Jan 2000.

[29] C. Hong, K. T. Bae and T. K. Pilgram. Coronary artery calcium: Accuracy and reproducibility of measurements with multi-detector row CT – assessment of effects of different thresholds and quantification methods, *Radiology*, 227: 795-801, May. 2003.

[30] I. Išgum, B. van Ginneken and M. Olree. Automatic detection of calcifications in the aorta from CT scans of the abdomen, *Academic Radiology*, 11(3): 247-257, Mar. 2004.

[31] T. T. de Weert, H. Cakir, S. Rozie, S. Cretier, E. Meijering, D. W. J. Dippel and A. van der Lugt. Intracranial internal carotid artery calcifications: association with vascular risk factors and ischemic cerebrovascular disease, *American Journal of Neuroradiology*, vol 30(1): 177-184, Jan. 2009.

[32] A. K. Jain. Fundamentals of digital image processing, *Upper Saddle River, NY, USA: Prentice-Hall, Inc*, 1989.

[33] I. Isgum, A. Rutten, M. Prokop and B. van Ginneken. Detection of coronary calcifications from computed tomography scans for automated risk assessment of coronary artery disease, *Medical physics*, 34(4): 1450-61, Apr. 2007.

[34] Y. Freund and R. Schapire. A decision–theoretic generalization of on-line learning and an application to boosting, *Lecture Notes in Computer Science .Proceedings of the Second European Conference on Computational Learning Theory*, 904: 23-37, 1995.

[35] J. Friedman, T. Hastie and R. Tibshirani. Additive logistic regression: A statistical view of boosting, *The Annals of Statistics,* 28(2): 337-407, 2000.

[36] P. Viola and M. Jones. Robust real-time object detection, *International Journal of Computer Vision*, 57(2: 137–154, 2004.

[37] A. Torralba, K. Murphy and W. Freeman. Sharing features: efficient boosting procedures for multiclass object detection, *IEEE Computer Society Conference on Computer Vision and Pattern Recognition*, 2: 762–769, 2004.

[38] R. Lienhart, A. Kuranov and V. Pisarevsky. Empirical analysis of detection cascades of boosted classifiers for rapid object detection, *DAGM 25th Pattern Recognition Symposium*, pp 297–304, 2003.

[39] T. T. de Weert, C. de Monye, E. Meijering, R. Booij, W. Niessen, D. W. J. Dippel and A. van der Lugt. Assessment of atherosclerotic carotid artery plaque volume with multidetector computed tomography angiography, *International Journal of Cardiovascular Imaging*, 24: 751–759, Oct. 2008.

[40] D. Altman. *Practical statistics for medical research*, Chapman & Hall/CRC, 1999.

4 Automated versus manual segmentation of atherosclerotic carotid plaque volume and components in CTA: associations with cardiovascular risk factors

This chapter is based on:

D. Vukadinović, S. Rozie, M. J. van Gils, T. van Walsum, R. Manniesing, A van der Lugt and W. J. Niessen. Automated versus manual segmentation of atherosclerotic carotid plaque volume and components in CTA: associations with cardiovascular risk factors, *International Journal of Cardiovascular Imaging*, May 2011.

Abstract

The purpose of this study was to validate automated atherosclerotic plaque measurements in carotid arteries from CT angiography (CTA).

We present an automated method (three initialization points are required) to measure plaque components within the carotid vessel wall in CTA. Plaque components (calcifications, fibrous tissue, lipids) are determined by different ranges of Hounsfield Unit values within the vessel wall.

On CTA scans of 40 symptomatic patients with atherosclerotic plaque in the carotid artery automatically segmented plaque volume, calcified, fibrous and lipid percentages were 0.97±0.51 cm^3, 10±11%, 63±10% and 25±5%; while manual measurements by first observer were 0.95±0.60 cm^3, 14±16%, 63±13% and 21±9% respectively and manual measurement by second observer were 1.05±0.75 cm^3, 11±12%, 61±11% and 27±10%.

In 90 datasets, significant associations were found between age, gender, hypercholesterolemia, diabetes, smoking and previous cerebrovascular disease and plaque features. For both automated and manual measurements, significant associations were found between: age and calcium and fibrous tissue percentage; gender and plaque volume and lipid percentage; diabetes and calcium, smoking and plaque volume; previous cerebrovascular disease and plaque volume. Significant associations found only by the automated method were between age and plaque volume, hypercholesterolemia and plaque volume and diabetes and fibrous tissue percentage. Significant association

found only by the manual method was between previous cerebrovascular disease and percentage of fibrous tissue.

Automated analysis of plaque composition in the carotid arteries is comparable with the manual analysis and has the potential to replace it.

4.1 Introduction

One of the major causes of death in the western world is atherosclerotic disease, which manifests itself as ischemic heart disease and ischemic stroke [1]. The amount of atherosclerotic disease in carotid arteries is normally expressed by the severity of luminal narrowing. Risk of (recurrent) stroke is related to the severity of stenosis [2]. However, the presence of a large atherosclerotic plaque is not always associated with luminal narrowing [3], which demonstrates that luminal narrowing alone is probably not a reliable marker of atherosclerosis. In addition, studies on carotid atherosclerotic plaque show that plaque morphology and composition are also important in the risk assessment of patients with carotid artery stenosis [4][5][6].

Atherosclerotic plaque volume and composition can be determined with Magnetic Resonance Imaging (MRI) [7-10] and CT angiography (CTA) [11-14]. CTA has established itself as an accurate modality to assess the presence of atherosclerotic disease and to grade the severity of stenosis [15]. Carotid plaques with a thin fibrous cap and a large lipid core are also considered to increase the risk for stroke [16][17], while plaques with high calcium content, especially when located superficially, are thought to be associated with a lower risk for stroke [18].

Manual measurement of plaque volume and the contribution of the different plaque components to the plaque volume in MRI or CTA data is a very labor intensive task. Several methods address the segmentation of the outer vessel wall and plaque components in both MRI and CTA data in carotid arteries [19-24] as well as coronary arteries [25][26]. We previously developed an algorithm to automate the plaque measurements in CTA imaging data of the carotid arteries. In this algorithm we combined outer vessel wall segmentation [27] with lumen segmentation [28]. Once the outer vessel wall and lumen were segmented, the plaque components were segmented using distinctive ranges of Hounsfield Unit (HU) values [11]. However, with this algorithm the outer vessel wall was automatically segmented only in common carotid artery, while atherosclerotic disease is commonly present in both the common and internal carotid artery.

The purpose of this study was to develop and evaluate a method to obtain automated measurements of plaque volume and its components at the carotid bifurcation and to demonstrate that this method has potential to replace the manual measurements in terms of accuracy in plaque volume and plaque component characterization. Furthermore, we investigated whether in group associations studies similar trends can be found with automated processing. Hereto, the method validation consists of (1) evaluation of the accuracy by comparing differences between method and manual tracings with variability of manual measurements of different observers and (2) comparison of the associations between cardiovascular risk factors and plaque features as assessed with manual segmentation and automated segmentations.

4.2 Materials and Methods

4.2.1 Study Population

From November 2002 to December 2005, patients with amaurosis fugax, TIA or minor ischemic stroke (Rankin score ≤ 3) were consecutively enrolled in the study cohort and clinical and research data were derived in a standardized way. Multi-detector CT angiography (MDCTA) of the carotid arteries was performed as part of a research protocol, approved by the Institutional Review Board. All patients gave written informed consent. All patients underwent neurological examination on admission and symptoms and risk factors were reported. Subsequently, all carotid arteries of those patients with symptoms in the anterior circulation were evaluated for the presence of atherosclerotic plaque. This validation study of the automated plaque segmentation has a retrospective study design. The main test set contained the symptomatic carotid artery from 90 randomly selected patients (63% male, mean age 67±11 years) from the group of patients with atherosclerotic plaque in the symptomatic carotid artery. The symptomatic carotid artery was the artery ipsilateral to the ischemic hemisphere, which was based on clinical symptoms and findings on MDCT of the brain. A subset of 40 datasets, which has a similar distibution of stenosis degrees as the full set, was used for the interobserver study.

4.2.2 Training set for Automated Method

The parameter settings for the automated method were previously trained on 40 manually annotated datasets, which are not part of the 90 datasets for which the method is evaluated. Furthermore this training was manually annotated by a different observer than the two observers who annotated the imaging data reported on this study. Hence, a possible bias of the method to one of the observers is prevented.

4.2.3 Scan Protocol and Image Reconstruction

CTA of the carotid arteries was performed on a 16-slice MDCT system (Siemens, Sensation 16, Erlangen, Germany) with a standardized optimized contrast-enhanced protocol (120 kVp, 180 mAs, collimation 16×0.75 mm, table feed 12 mm/rotation, pitch 1) [29]. All patients received 80 ml contrast material (Iodixanol 320 mg/ml, Visipaque, Amersham Health, Little Chalfont, UK), followed by 40 ml saline bolus chaser, each at an injection rate of 4 ml/sec. Synchronization between the passage of contrast material and data acquisition was achieved by real-time bolus tracking at the level of the ascending aorta. Image reconstructions were made with a 120-mm field of view, a matrix size of 512×512, a slice thickness of 1.0 mm, an increment of 0.6 mm, and an intermediate reconstruction filter (B46f).

4.2.4 Plaque Volume and Composition Measurements

To define different plaque components by using different HU ranges, it is sufficient to have a segmentation of the carotid artery outer vessel wall and the lumen [11]

4.2.4.1 Automated Segmentation of the Outer Vessel Wall and Lumen

An automatic method using a three-point initialization was used to segment the outer vessel wall of the carotid artery in CTA [27][30]. First, the vessel lumen was segmented using a level set approach [28], using an initialization point in the common, internal and external carotid artery. Subsequently, using a set of image features, calcium objects which are part of the vessel wall were detected using a GentleBoost framework [27]. Calcium object classification is used as a preprocessing step for the outer vessel wall segmentation since it is a much easier task than outer vessel segmentation and it can improve the accuracy of outer vessel wall segmentation. In the third step probability images were created that indicate the likeliness of a voxel lying within or outside the vessel, using the same GentleBoost framework. Each voxel is represented by a set of descriptive features: distance of the pixel to the lumen center and a set of contextual features. Contextual features in this case are radial image intensity profiles emanating from the lumen center. These profiles are extracted from the original image, the image smoothed with 2D Gaussian filters at different scales and directional 2D, Gaussian derivatives also at different scales. Based on this set of features, a GentleBoost classifier is trained to classify each pixel as being inside or outside vessel wall. The classifier provides a confidence measure which reflects the likelihood that a pixel lies inside or outside the vessel.

Finally, ellipsoids are fitted using both the calcium and vessel classification results.

4.2.4.2 Manual Segmentation of the Outer Vessel Wall and Lumen

Images of carotid arteries that contained plaque were analyzed using custom-made quantitative image analysis software, developed using MeVisLab (MeVis Research, Bremen, Germany). Using this software, regions of interest (ROI) were manually drawn over the outer vessel wall contour in consecutive axial MDCTA images (Fig. 4.1). Since the observers placed the ROI over the outer vessel wall contour, the ROI consisted of both plaque and lumen. The window/level setting was fixed at 1200/800 HU for all measurements.

To assess the border between lumen and atherosclerotic plaque it was necessary to draw a second ROI close to the lumen in each image. Normally, the lumen area was then automatically differentiated from atherosclerotic plaque based on the adjusted cut-off value. But in those plaques in which calcifications bordered the lumen and the two dense structures merged with each other, lumen area and calcifications had to be separated by manual drawing. One observer (S.R.) who was blinded to other clinical information, manually drew lumen and outer vessel wall contours. A second observer (M.G.) performed the manual segmentations in the interobserver dataset. A third observer (T.W.) performed manual annotation of the training set on which our automated method was trained.

4.2.4.3 Calculation of the Volume of Plaque and the Components

Having the carotid artery vessel wall and lumen segmented, different HU ranges were used to define different plaque components. The cut-off point for the distinction between calcifications and fibrous tissue was set at 130 HU, the value currently used for calcium scoring. The cut-off point for the distinction between fibrous tissue and lipid was set at 60 HU as determined in previous studies [11]. We adjusted the cut-off point for the distinction between atherosclerotic plaque and vessel lumen for each patient on the basis of the full-width-half-maximum principle (mean lumen attenuation plus mean fibrous tissue attenuation (≈ 88 HU) divided by two). The pixels surrounding the vessel lumen, with a density between 130 HU and the adjusted cut-off value, were considered to be fibrous tissue.

The plaque volume and the volume of the plaque components were calculated by multiplying the number of pixels of the total atherosclerotic plaque or its components, with the pixel size and the slice increment. The proportion of plaque components was calculated as the ratio of volume of the component to the total plaque volume multiplied by 100. As an example, in Fig. 4.1 a cross-sectional slice with outer vessel wall and all three plaque components in different colors automatically segmented and manually segmented by two observers is shown.

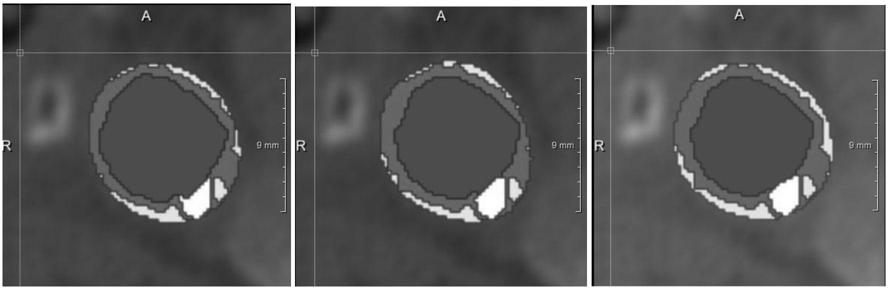

Figure 4.1 Different plaque components on one cross sectional slice segmented by the automated method (left), observer S.R. (center) and observer M.G. (right). ■lumen, ▨fibrous, □ lipids, □calcium

4.2.5 Cardiovascular Risk Factors

We obtained clinical measures and information on risk factors and medication during the patient’s visit at the outpatient clinic. Subjects were categorized as currently, ever, or never smoking. Hypertension was defined as systolic blood pressure over 140 mmHG and/or diastolic blood pressure over 90 mmHg during two episodes of at least 15 min of continuous noninvasive blood-pressure measurement and/or treatment with antihypertensive medication. Blood pressure-lowering drugs comprised ACE inhibitors, calcium-antagonists, beta-blockers, and diuretics. Hypercholesterolemia was defined as fasting cholesterol over 5.0 mmol/l and/or use of cholesterol-lowering drugs. Diabetes was defined as fasting serum glucose levels over 7.9 mmol/l, nonfasting serum glucose levels over 11.0 mmol/l, or use of antidiabetic medication. Information was collected on previous cardiovascular events and conditions (myocardial infarction, atrial fibrillation, angina pectoris, chronic heart failure, coronary artery bypass grafting) and previous cerebrovascular events.

4.2.6 Statistical Analysis

Both for automated and manual measurements (2 observers), plaque and plaque component volumes and proportions were presented on 40 datasets with mean ± (SD). The differences between automated and manual measurements and those between the measurements of two observers are presented with mean values and standard deviations. The differences between the automated and manual measurements (2 observers) on 40 datasets were plotted against the mean value of the measurements (Bland-Altman plot), they were evaluated with paired Student t-test and the correlation between the measurements by the two methods was evaluated by Pearson's correlation coefficient (R_P). Bland-Altman plots are plotted in Excel. Limits of agreement are calculated as average difference ± 1.96 · standard deviation of the difference.

The differences between automated and manual measurements on 90 datasets (1 observer) are presented with mean values and standard deviations and the correlation was evaluated by R_P.

Both for automated and manual measurements (1 observer) we determined the associations between cardiovascular risk factors and PV and plaque composition on 90 datasets using univariable linear regression. Multivariable analysis was not performed for two reasons. Firstly, the focus of the study was to show that automated method can replicate the associations between manually measured plaque components and cardiovascular risk factors. Second, we did not focus on the assessment of independent associations between risk factors and plaque characteristics as this was not possible due to limited sample size. Because the distribution of plaque volume was skewed, we used a log10 transformation prior to statistical analysis. Similarly, for proportion of plaque components we used square root (sqrt) transformation.

P values <0.05 were considered statistically significant. Statistical analyses were performed using SPSS software (version 15.0, Inc., Chicago, Illinois).

4.3 Results

4.3.1 Baseline Clinical Characteristics

The baseline characteristics are presented in Table 4.1.

Characteristics	N=90
Age [years; mean ±SD]	67±11
Male sex [%]	63
Hypertension [%]	84
Hypercholesterolemia [%]	85
Diabetes Mellitus [%]	24
Smoking: current or past [%]	44
Previous cardiac disease [%]	35
Previous cerebrovascular disease [%]	31

Table 4.1 Demographic and clinical characteristics of 90 patients

4.3.2 Plaque Measurements: Comparison to Interobserver Variability

Table 4.2 shows lumen, plaque volume, plaque component volumes and plaque component proportions assessed by the automated method and by the manual methods (two observers) in 40 datasets. The differences between the automated and the manual method and between the manual measurements of two observers are also shown. The differences between automated method and both observers were in the same range as the differences between observers.

The difference between the automated method and first observer manual measurements of PV, calcified, fibrous and lipid percentages were 0.02±0.24cm^3, -4±6%, -0±8% and 4±7% respectively. The differences between automated method and second observer manual measurements of PV, calcified, fibrous and lipid percentages were -0.09±0.43cm^3, -1±4%, 2±8% and -1±9% respectively. The differences between two observers manual measurements of PV, calcified, fibrous and lipid percentages were 0.11±0.29cm^3, 3±5%, 2±6% and -5±7% respectively. Similar differences were found between automated plaque measurements and manual measurements performed on 90 datasets by observer S.R.

Fig.4.2. shows regression plots and Pearson's correlation coefficient (R_P) between automated and manual measurements by both observers of plaque features on 40 datasets. For PV, calcium, fibrous and lipid contribution

correlation coefficients between automated and manual measurements of observer S.R. and M.G. were: 0.92 and 0.83; 0.94 and 0.94; 0.79 and 0.73 and 0.57 and 0.52 respectively. Correlation coefficients between automated and manual measurements by observer S.R. on 90 datasets of PV, calcium, fibrous and lipid contributions were 0.89, 0.86, 0.77 and 0.55 respectively.

From the Bland–Altman plots, in Fig. 4.3, it can be observed that the difference

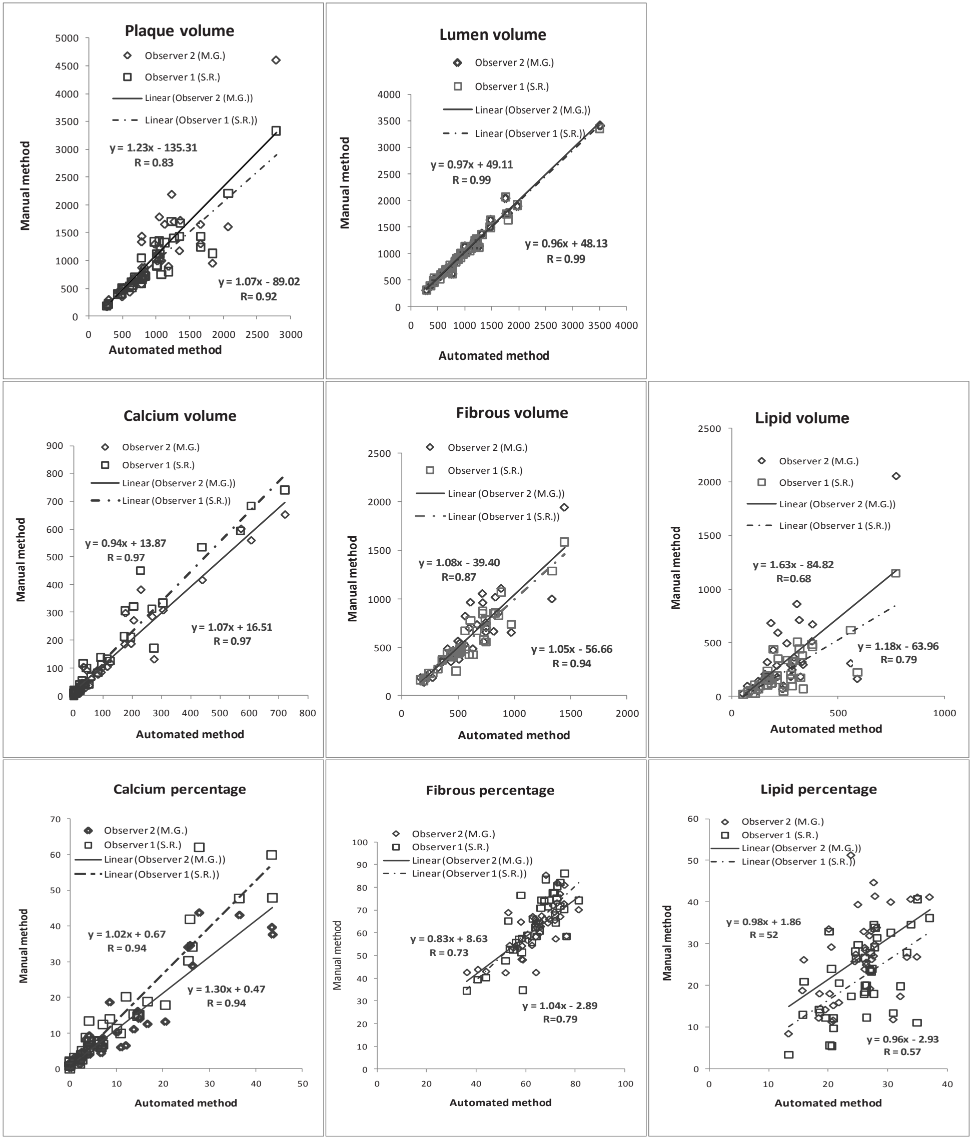

Figure 4.2 Regression plots showing the comparison between automated and manual measurements in 40 datasets.

between automated and manual measurements of plaque volume increases when the volume increases. Similarly, the difference between automated and manual measurements of plaque components proportions increase with the components proportions.

Plaque volume Calcium Percentage

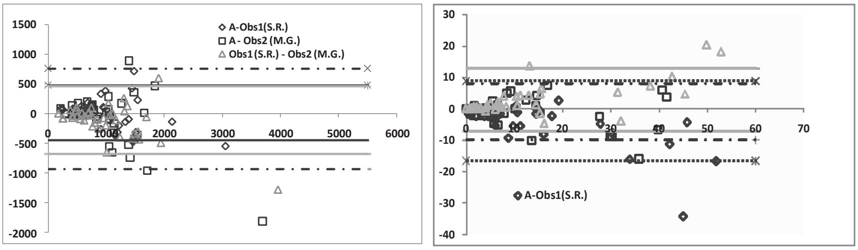

Fibrous Percentage Lipids Percentage

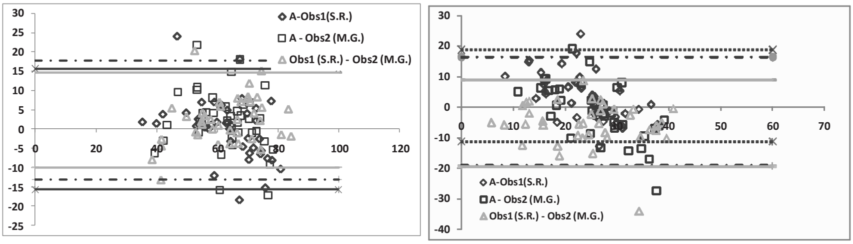

Figure 4.3 Bland-Altman plots of plaque volume and plaque components percentages assessed by automated method and manual method by two observers in 40 datasets.

4.3.3 Risk factors Associations with Plaque Features: Comparison Between Manual and Automated Measurements.

Table 4.3 shows the associations between cardiovascular risk factors and automatically assessed and manually assessed plaque volume and plaque component percentages on 90 datasets. Mostly, similar associations were found with automatically and manually assessed plaque features and cardiovascular risk factors.

Older patients had significantly larger PV measured by the automated method, whereas the association with manually assessed PV was not significant (p=0.065). Male patients had significantly higher plaque volume for both automated and manual plaque measurements. Patients with hypercholesterolemia had significantly lower plaque volume when measured with the automated method, and not when measured manually. Patients who were smokers and patients who had a history of cerebrovascular disease had significantly higher plaque volume for both automated and manual plaque measurements.

For both automated and manual plaque measurements older patients had a significantly higher calcium contribution and a significantly lower fibrous contribution. Male patients had a significantly higher lipid contribution for both automated and manual plaque measurements. Patients with diabetes had a significantly higher calcium contribution for both automated and manual plaque measurements and a significantly lower fibrous contribution when measured with the automated method and not when measured manually.

Patients with a history of cerebrovascular disease had a significantly lower fibrous contribution when measured manually and not when measured automatically.

4.4 Discussion

In this study we presented a method for automated plaque volume and plaque composition assessment. Furthermore, we evaluated its accuracy (i) with respect to manual tracings, and (ii) its ability to replicate associations between plaque characteristics and cardiovascular risk factors.

With respect to segmentation accuracy, we showed that the differences in estimating plaque volume and plaque components between our automated method and expert observers are in the same range as interobserver variability. The results show some bias between the observers and between observers and the method. All automated volume measurements values are larger than volumes measured by observer S.R and smaller than the volumes measured by observer M.G with the exception of calcium volume and fibrous contribution. All the volumes and proportion differences between two observers were statistically significant, although these differences were small. The statistically significant difference is a consequence of a persistent, albeit small, oversegmentation of most plaque components by observer M.G compared to observer S.R. The differences between automated method and observer S.R were significant for calcium volume and proportion and lipid proportion. None of the differences between automated method and observer M.G. were significant. The differences between automated method and observer S.R were larger than the differences between automated method and observer M.G for more measurements: calcium volume, fibrous volume, calcium proportion and lipid proportion. In a previous interobserver study of plaque and plaque components assessment with CTA, in which three observers manually annotated 46 CTA datasets [14], the differences of plaque volume and all plaque components were significant between at least one pair of observers [14]. Pearson's correlation coefficients between automated and manual measurements of both observers for PV and plaque contributions were mostly similar as shown in Fig. 4.2.

In a second evaluation, we showed that associations between cardiovascular risk factors and automated plaque measurements were mostly similar to the associations found with manual plaque measurements. Seven associations were significant for both the automated and manual plaque measurements; one was significant for the automated method and almost significant for manual method and three were significant for only one of the methods. The associations that were found to be significant for both manual and automated measurements have also similar correlation coefficient values.

To our knowledge, this is the first study that compares cardiovascular risk factors associations with manually and automatically assessed plaque volume and plaque components. When comparing our results with results of a previous study in which the association between cardiovascular risk factors and manually assessed plaque volume and plaque components was evaluated in 57 symptomatic carotid arteries [31], we found more associations. This can possible be explained by the larger number of datasets that is used in our study. In the previous study age and smoking were related to plaque volume, which is confirmed in our current study. In the previous study, patients with hypercholesterolemia had significantly less lipid and more calcium; these associations were not confirmed. A reason for this could be that automated results are the least similar to manual ones in case of lipids contribution (R_p=0.55). Calcium proportion is shown to be underestimated by the automated method..

In previous studies from our institute on CT based plaque assessment [11], [29] and [14], different datasets were used than in this paper. The 57 datasets used to relate manually derived plaque measurements to cardiovascular risk factors in [31] are a subset of the 90 datasets used in this paper. Compared to this work, we thus both extended the dataset, and we investigated the influence of automated plaque assessment, in order to try to replace laborious manual plaque segmentation.

Manual quantification takes on average around 30 minutes per carotid artery. This time period depends on the lesion length. The automated method takes on average around 6 minutes on a single CPU 2GHZ, RAM 24 GB computers. Manual plaque segmentation is not applicable in clinical setting, because it is too time-consuming. Automated plaque assessment already is considerably faster and improved implementation and hardware could reduce processing time such that it would become acceptable in clinical workflow. Also, this automated tool can be used in larger datasets for the investigation of associations between plaque volume / composition and risk factors or recurrent ischemic events and for longitudinal studies on plaque imaging.

4.5 Study Limitations

A limitation of our study is that we do not have a definite gold standard. The scarcity of histological carotid plaque specimens hampers the validation of automated plaque volume and composition assessment on a sizeable dataset. We therefore compared results from automated plaque segmentation with those from manual plaque segmentation-a method previously validated against histology-thus indirectly evaluating the performance of our automated method.

A second limitation of our study is that we used CT data from a single vendor, collected at a single site. Our automated method might perform less on data from different CT-scanners, different sites or using different image protocols. However, the underlying method is generic and if required can be tuned to different systems by using new training on data. A third limitation concerns the plaque segmentation method that uses distinctive ranges of Hounsfield Unit (HU) values [11]. There is some overlap between the HU of lipid and fibrous tissue and no distinction can made between lipid and intraplaque heamorrhage, which is thought to be an important feature in plaque vulnerability assessment as well [9].

As a final limitation, the comparison of cardiovascular risk factors associations with manually and automatically segmented plaque components does only indicate that the automated method can be used to find similar associations in a group study. It does not provide information on the method applicability on a single subject.

4.6 Conclusion

We presented an approach to automatically segment outer vessel wall and plaque of carotid artery in CTA and to automatically assess plaque volume and plaque components. The results were validated with respect to manual tracings and interobserver variability. Furthermore, the associations between cardiovascular risk factors and plaque volume and plaque component contributions assessed by our automated method and a manual method were compared. We have shown that the difference between our automated method and the observers is in the range of the variability of the observers, and hence can be applied for automated analysis in large studies.

40 datasets	μ (A) ± SD	μ (Obs 1) ± SD	μ (Obs 2) ± SD	μ (Diff (A,Obs1)) ± SD	μ (Diff (A,Obs2)) ± SD	μ (Diff (Obs1, Obs2)) ± SD
Plaque volume [mm^3]	965±511	946±595	1052±754	19±235	-87±432	-106±288*
Lumen volume [mm^3]	1030±577	1040±562	1052±567	-10±84	-22±73	-12±27*
Calcium volume [mm^3]	129±178	155±197	136±174	-26±50*	-6±45	19±31*
Fibrous volume [mm^3]	591±271	564±302	602±336	26±101	-10±165	-37±112*
Lipid volume [mm^3]	244±144	225±215	314±348	18±133	-69±272	-88±190*
Calcium proportion [%]	10±11	14±16	11±12	-4±6*	-1±4	3±5*
Fibrous proportion [%]	63±10	63±13	61±11	-0±8	2±8	2±6*
Lipid proportion [%]	25±5	21±9	27±10	4±7*	-1±9	-5±7*

Table 4.2 Plaque features measured by automated method and by two observers in 40 datasets with the differences and coefficients of variation: μ- mean, A – automated method, Obs1 – first observer, Obs2 – second observer, SD – standard deviation, Diff – difference, CoV – coefficient of variation, * - t-test P-value < .05

90 Datasets	PV(A)	PV (M.)	Calc % (A)	Calc % (M)	Fib % (A)	Fib % (M.)	Lip % (A)	Lip % (M)
	B(P-value)	B(P-value)	B(P-value)	B(P-value)	B(P-value)	B(P-value)	B(P-value)	B(P-value)
Age	.004 (.029)*	.005 (.065)	.048 (.004)*	.056 (.001)*	-.013 (.033)*	-.021 (.005)*	-.006 (.25)	-.006 (.56)
Gender	.113 (.010)*	.168 (.003)*	.182 (.64)	.192 (.64)	-.196 (.16)	-.323 (.062)	.234 (.048)*	.560 (.024)*
Hypercholesterolemia	-.120 (.049)*	-.054 (.49)	-.728 (.17)	-1.056 (.060)	.268 (.16)	.152 (.53)	-.064 (.71)	.505 (.14)
Hypertension	.052 (.39)	.048 (.52)	.315 (.54)	.224 (.68)	-.005 (.98)	-.044 (.85)	-.106 (.52)	-.138 (.68)
Diabetes mellitus	.025 (.62)	.018 (.78)	1.163 (.006)*	1.231 (0.007)*	-.396 (.010)*	-.317 (.10)	-.103 (.46)	-.403 (.15)
Smoking (ever)	.093 (.031)*	.113 (.038)*	.137 (.72)	.094 (.82)	-.048 (.72)	-.093 (.58)	.015 (.90)	.221 (.36)
Previous cardiac disease	.053 (.24)	.075 (.19)	.593 (.12)	.634 (.13)	-.095 (.50)	-.264 (.13)	-.199 (.11)	-.058 (.82)
Previous cerebrovascular disease	.122 (.008)*	.138 (.019)*	.489 (.22)	.812 (.056)	-.234 (.11)	-.465 (.009)*	.047 (.71)	.076 (.77)

Table 4.3 The associations between risk factors and PV and plaque components percentages assessed by automatic method (A) and manual method (M) in 90 datasets. The associations were assessed by linear regression and represented by coefficient of regression (B) and P-value.

* - significant p-values (<0.05), PV – plaque volume, A - automated method, M – manual method, B – regression coefficients, Calc – calcium, Fib – fibrous, Lip – lipids.

4.7 References

[1] M. Robins and H. M. Baum, The national survey of stroke: Incidence, *Stroke*, 12: I 45–I57, Mar. - Apr.1981.

[2] North American symptomatic carotid endarterectomy trial collaborators. Beneficial effect of carotid endarterectomy in symptomatic patients with high-grade carotid stenosis, *N. Engl. J. Med.*, vol 325(7):445-453, Aug. 1991.

[3] S. Glagov, E. Weisenberg, C. K. Zarins, R. Stankunavicius and G. J. Kolettis. Compensatory enlargement of human atherosclerotic coronary arteries, *N Engl J Med*, 316 (22):1371–1375, May 1987.

[4] P. M. Rothwell, R. Gibson and C. P. Warlow. Interrelation between plaque surface morphology and degree of stenosis on carotid angiograms and the risk of ischemic stroke in patients with symptomatic carotid stenosis, *Stroke*, 31(3):615–621, Mar 2000.

[5] J. K. Lovett, P. J. Gallagher, L. J. Hands, J. Walton and P. M. Rothwell. Histological correlates of carotid plaque surface morphology on lumen contrast imaging, *Circulation*, 110(15):2190–2197, Oct 2004.

[6] M. Naghavi, P. Libby, E. Falk, S. W. Casscells, S. Litovsky, et al. From vulnerable plaque to vulnerable patient: A call for new definitions and risk assessment strategies: Part I, *Circulation*, 108: 1664-1672, 2003.

[7] T. Saam, T. S. Hatsukami, N. Takaya, B. Chu, H. Underhill, W. S. Kerwin, J. Cai, M. S. Ferguson, C. Yuan. The vulnerable, or high-risk, atherosclerotic plaque: noninvasive MR imaging for characterization and assessment, *Radiology*, 244:64-77, 2007.

[8] J. M. Cai, T. S. Hatsukami, M. S. Ferguson, R. Small, N. L. Polissar, C. Yuan. Classification of human carotid atherosclerotic lesions with in vivo multicontrast magnetic resonance imaging, *Circulation,* 106(11):1368-1373, 2002.

[9] N. Takaya, C. Yuan, B. Chu, T. Saam, H. Underhill, J. Cai, N. Tran, N. L. Polissar, C. Isaac, M. S. Ferguson, G. A. Garden, S. C. Cramer, K. R. Maravilla, B. Hashimoto, T. S. Hatsukami. Association between carotid plaque characteristics and subsequent ischemic cerebrovascular events: A prospective assessment with magnetic resonance imaging – initial results, *Stroke,* 37: 818–823, 2006.

[10] C. Yuan, K. W. Beach, L. H. Jr Smith and T. S. Hatsukami. Measurement of atherosclerotic carotid plaque size in vivo using high resolution magnetic resonance imaging, *Circulation*, 1998.

[11] T. T. de Weert, M. Ouhlous, E. Meijering, P. E. Zondervan, J. M. Hendriks, M. R. H. M. van Sambeek, D. W. J. Dippel, and A. van der Lugt. In vivo characterization and quantification of atherosclerotic carotid plaque

components with multidetector computed tomography and histopathological correlation, *Arterioscler. Thromb. Vasc. Biol.*, 26(10): 2366–2372, Oct 2006.

[12] K. R. Nandalur, A. D. Hardie, P. Raghavan, M. J. Schipper, E. Baskurt, C. M. Kramer. Composition of the stable carotid plaque: insights from a multidetector computed tomography study of plaque volume, *Stroke* 38:935–940, 2007.

[13] M. Wintermark, S. S. Jawadi, J. H. Rapp, T. Tihan, E. Tong, D. V. Glidden, S. Abedin, S. Schaeffer, G. Acevedo-Bolton, B. Boudignon, B. Orwoll, X. Pan and D. Saloner. High-resolution CT imaging of carotid artery atherosclerotic plaques, *AJNR Am J Neuroradiol* 29:875–882, 2008.

[14] T. de Weert, C. de Monye, E. Meijering, R. Booij, W. J. Niessen, D. W. J. Dippel, A. Van der Lugt, Assesment of atherosclerotic carotid plaque volume with multidetector computed tomography angiography, *International Journal of Cardiovascular Imaging*, 24: 751-9, 2008.

[15] M. J. Koelemay, P. J. Nederkoorn, J. B. Reitsma and C. B. Majoie. Systematic review of computed tomographic angiography for assessment of carotid artery disease, *Stroke* 35:2306–2312, 2004.

[16] H. S. Bassiouny, Y. Sakaguchi, S. A. Mikucki, et al. Juxtalumenal location of plaque necrosis and neoformation in symptomatic carotid stenosis, *J Vasc Surg* , 26:585–94, 1997.

[17] G. M. Biasi, A. Froio, E. B. Diethrich, et al. Carotid plaque echolucency increases the risk of stroke in carotid stenting: the imaging in carotid angioplasty and risk of stroke (ICAROS) study, *Circulation*, 110:756–62, 2004.

[18] M. Miralles, J. Merino, M. Busto, et al. Quantification and characterization of carotid calcium with multi-detector CT-angiography, *Eur J Vasc Endovasc Surg,* 32:561–67, 2006.

[19] C. Yuan, E. Lin, J. Millard and J. N. Hwang. Closed contour edge detection of blood vessel lumen and outer wall boundaries in black-blood MR images, *Magn. Reson. Imaging*, 17(2):257-266, Feb. 1999.

[20] G. J. Adams, G. W. Vick, C. B. Bordelon, W. Insull and J. D. Morrisett. An algorithm for quantifying advanced carotid artery artherosclerosis in humans using MRI and active contours, *Proc. SPIE Medical Imaging*, 4684:1448-1457, 2002.

[21] I. M. Adame, R. J. van der Geest, B. A. Wasserman, M. A. Mohamed, J. H. C. Reiber, B. P. F. Lelieveldt. Automatic segmentation and plaque characterization in atherosclerotic carotid artery MR images, *MAGMA*, 16(5):227 – 234, Apr. 2004.

[22] F. Liu, D. Xu, M. S. Ferguson, B. Chu, T. Saam, N. Takaya, T. S. Hatsukami, C. Yuan and W. S. Kerwin. Automated in vivo segmentation of

carotid plaque MRI with morphology-enhanced probability maps, *Magnetic Resonance in Medicine*, 55:659 – 688, 2006.

[23] F. Yang, G. Holzapfel, C. Schulze-Bauer, R. Stollberger, D. Thedens, L. Bolinger, A. Stoplen and M. Sonka. Segmentation of wall and plaque in in vitro vascular MR images, *The International Journal of Cardiolvascular Imaging,* 19:419-428, 2003.

[24] W. Kerwin, D. Xu, F. Liu, T. Saam, H. Underhill, N. Takaya, B. Chu, T. Hatsukami and C. Yuan. MRI of carotid atherosclerosis: Plaque analysis, *Topics in Magnetic Resonance Imaging*, 18:371-378, Nov 2007.

[25] D. Dey, V. Cheng, P. Slomka, R. Nakazato, A. Ramesh, S. Gurudevan, G. Germano and D. Berman. Automated 3-dimensional quantification of noncalcified and calcified coronary plaque from coronary CT angiography, *J Cardiovasc Comput Tomography,* 3(6):372-382, 2009.

[26] O. Klass, S. Kleinhans, M. J. Walker, M. Olszewski, S. Feuerlein, M. Juchems and M. H. K. Hoffmann. Coronary plaque imaging with 256-slice multidetector computed tomography: interobserver variability of volumetric lesion parameters with semiautomatic plaque analysis software, *Int J CardiovascImaging,* 26(6):711-720, 2010.

[28] D. Vukadinovic, T. van Walsum, R. Manniesing, S. Rozie, K. Hameeteman, T. T. de Weert, A. van der Lugt and W.J. Niessen. Segmentation of the outer vessel wall of the common carotid artery in CTA, *IEEE Transactions on Medical Imaging*, 2010.

[29] R. Manniesing, B. K. Velthuis, M.S. van Leeuwen, I. C. van der Schaaf , P.J. van Laar and W. J. Niessen. Level set based cerebral vasculature segmentation and diameter quantification in CT angiography, *Med. Image Anal.*, 10(2):200-214, Apr. 2006.

[30] C. de Monye, F. Cademartiri, T. T. de Weert, D. A. Siepman, D. W. Dippel and A. van der Lugt. Sixteen-detector row CT angiography of carotid arteries: comparison of different volumes of contrast material with and without a bolus chaser, *Radiology* 237:555–562, 2005.

[31] D. Vukadinovic, T. van Walsum, S. Rozie, T. T. de Weert, R. Manniesing, A. van der Lugt and W. J. Niessen. Carotid artery segmentation and plaque quantification in CTA, *IEEE International Symposium on Biomedical Imaging*, Jan 2010.

[32] S. Rozie, T. de Weert, C. de Monye, P. J. Homburg, H. L. J. Tanghe, D. W. J. Dippel and A. van der Lugt. Atherosclerotic plaque volume and composition in symptomatic carotid arteries assessed with multidetector CT angiography; relationship with severity of stenosis and cardiovascular risk factor, *European Radiology*, 2009.

5 Region Based Level Set Segmentation of the Outer Wall of the Carotid Bifurcation in CTA

This chapter is based on:

D. Vukadinović, T. van Walsum, S. Rozie, T.T. de Weert, R. Manniesing, A. van der Lugt and W. J. Niessen. Carotid Artery Segmentation and Plaque Quantification in CTA, *IEEE International Symposium on Biomedical Imaging*, 2009

Abstract

This paper presents a level set based method for segmenting the outer vessel wall and plaque components of the carotid artery in CTA. The method employs a GentleBoost classification framework that classifies pixels as calcified region or not, and inside or outside the vessel wall. The combined result of both classifications is used to construct a speed function for level set based segmentation of the outer vessel wall; the segmented lumen is used to initialize the level set. The method has been optimized on 20 datasets and evaluated on 80 datasets for which manually annotated data was available as reference. The average Dice similarity of the outer vessel wall segmentation was 92%, which compares favorably to previous methods.

5.1 Introduction

Cardiovascular diseases are a main cause for morbidity and mortality worldwide [1]. One of the main causes of cardiovascular diseases is atherosclerosis, which can be effectively imaged with CT Angiography (CTA) [2]. The severity of stenosis caused by atherosclerosis in the carotid bifurcation is an important risk factor for stroke [3]; however, luminal stenosis as a parameter of carotid artery disease does not necessarily reflect the amount of atherosclerosis [4]. Quantification of plaque features may therefore provide a better diagnosis and prediction of cardiovascular events. This quantification requires segmentation of the lumen and outer vessel wall.

Many authors addressed the problem of outer wall segmentation and plaque quantification on both MRI and CT data. Olabarriaga et al. [5] proposed a deformable model based segmentation of the lumen and thrombus in abdominal aortic aneurysms in CTA data. For the wall segmentation a gray level modeling approach with a KNN classifier using intensity profiles sampled along the surface normal was used. The active shape model (ASM) based method by De Bruijne et al. [6,7] also addressed aortic aneurysm segmentation. This method requires a manual delineation of the aneurysm in the first slice after which the contour propagates to the adjacent slices based on grey value similarity. A slice-by-slicecontrol by the user is required. De Bruijne et al. [8] also proposed a 3D ASM which included a grey level appearance model which was based on non-parametric pattern classification. The user has to draw the top and bottom contours, and indicate the approximate aneurysm centre. Reported results are accurate, but the amount of interaction for initialization is still significant.

A snake based method for defining the vessel lumen and wall boundaries in MR images of the carotid artery was proposed by Yuan et al. [9]. Adams et al. [10] proposed a similar method, deforming two initial contours in MR carotid artery images. Both methods require a high level of manual interaction. Adame et al. [11] proposed a gradient based ellipse fitting method combined with fuzzy clustering to outline the carotid artery outer vessel wall on MR images. The method requires manual interaction, namely a center point in the lumen, a seed point inside the lipid core and a circle that surrounds the vessel.

Liu et al. [12] proposed a method for carotid plaque segmentation in MRI using probability maps utilizing morphology information.

In this paper a novel method for carotid artery outer vessel wall segmentation in CTA is presented, which is an extension of work we previously presented [13, 14]. The main contribution of our work is that we combine voxel classification with a 3D level set segmentation for the carotid artery outer vessel wall rather than 2D ellipsoid fitting, which allows application of the method for segmenting the whole carotid bifurcation. Additionally, we evaluate the method proposed on a large number of CTA datasets.

A similar method has been reported for segmenting abdominal aortic aneurysms, where a support vector machine classifier is used to control a level set based segmentation. [15].

The remainder of this paper is organized as follows: In Section 5.2 the methodology is presented. In Section 5.3 the experimental set up is described followed by a discussion and conclusion in Section 5.4.

5.2 *Methodology*

5.2.1 Overview

The method consists of four steps. First, the vessel lumen is segmented using a level set approach initialized with three seed points indicated by the user in the CCA, ICA and external carotid artery (ECA); for detailed information on the lumen segmentation we refer to the work by Manniesing et al. [16]. Subsequently, using a set of image features, calcium objects which are part of the vessel wall, are detected using a GentleBoost classifier [13]. In the third step voxels are classified as within or outside the vessel, using the same classification method [13]. Then segmentation is performed by fitting a model to the classification image. In this work, a 3D region based level set method is applied which segments the outer boundary using the calcium and inner-outer vessel region classifications results to create a speed function. The classification process and the level set method are described in more detail below.

5.2.2 Calcium and Vessel classification

Calcified regions are important markers for determining the outer vessel wall location. As described in [13], the region of interest around lumen is thresholded with high threshold, Th = 320HU. In this way candidate objects are extracted which are further classified as true or false calcified regions.

Figure 5.1 An example of a classification result, showing the confidence image with darker regions more likely belonging to the inside of the outer vessel wall. The black mask highlights negative values in the image. The light contour represents the ground truth for the outer vessel wall as drawn by an experienced clinician.

Classification is done based on a set of features, i.e. spatial, size, intensity and shape features [13].

For vessel classification, each pixel in the region of interest around lumen is described with a set of contextual image features extracted from radial profiles positioned radially from the lumen center. These features are used to classify each pixel as being inside or outside vessel wall [13].

As described in [13], calcium and inner-outer vessel region classification are combined by connecting lumen and calcified region since we are certain that this region is inside the vessel. In this way confidence image is created with negative values inside and positive values outside ranging from -1 to 1(Fig 5.1).

5.2.3 Region Based Level Set Outer Vessel Wall Segmentation

Atherosclerotic plaque is usually present around the bifurcation. That is why it is essential that plaque is segmented in the region including bifurcation. Level sets are suitable for representing complex geometries. We therefore apply a region based level set [17] to segment the carotid artery outer vessel wall, using the the classification results.

The resulting image of the combined calcium and inner-outer vessel region classification represents the confidence that a pixel belongs to the vessel region (Fig 5.1): the confidence image values are negative inside and positive outside with values ranging between -1 and 1. In case of a perfect classification, the vessel wall should pass through the zero values of the confidence image. However, simply thresholding the classification image will result in disconnected regions, and does not account for potential classification errors. Therefore, we use a region based level set segmentation to obtain one connected region with smooth boundaries. In the original paper of Chan and Vese on region based level set segmentations [17], the energy function that is minimized is defined as follows:

$$\begin{aligned} F(c_1, c_2, C) = \mu \cdot Length(C) + \\ +\lambda_1 \int_{inside(C)} |I(x,y) - c_1|^2 dxdy + \\ +\lambda_1 \int_{outside(C)} |I(x,y) - c_1|^2 dxdy, \end{aligned} \tag{1}$$

where:

$$C = \{(x,y) \in \Omega : \phi(x,y) = 0\}$$
$$inside(C) = \{(x,y) \in \Omega : \phi(x,y) > 0\}$$
$$outside(C) = \{(x,y) \in \Omega : \phi(x,y) < 0\},$$

$\Omega \subset \mathbb{R}^d$ is the image domain and $I\colon \Omega > R$ and $\mu \geq 0$, λ_1, $\lambda_2 \geq 0$ are parameters, I is a given image, c_1 is the average intensity value of i inside C and c_2 the average value of I outside C.

In our case, we want to penalize positive values inside and negative values outside the zero level set. In order to achieve this, we choose constants c_1 and c_2 to be equally distant from zero with c_1 negative and c_2 positive. We choose c_1=-0.5 and c_2=0.5 considering the values of I image.

The speed function for the level set evolution is calculated by minimizing (1) with the Euler-Lagrange equation while taking into account the sign of image I values inside and outside zero level set. The level set evolution equation for the confidence image becomes:

$$\frac{\partial \phi}{\partial t} = \delta(\phi)\left[\mu\, div\left(\frac{\nabla\phi}{|\nabla\phi|}\right) + \lambda_1(I+0.5)^2 - \lambda_2(I-0.5)^2\right] \tag{2}$$

$$in\ (0,\infty) \times \Omega,$$

where ϕ is a level set function.

The above equation (2) is the implicit active contour model implemented in this paper. The lumen segmentation dilated with a “shape” structuring element of “size” pixels is used to initialize the level set.

5.2.4 Plaque Segmentation

Using the carotid artery vessel wall and lumen segmented, different HU ranges were selected to define different plaque components. The cut-off point for the distinction between calcifications and fibrous tissue was set at 130 HU, the value currently used for calcium scoring. The cut-off point for the distinction between fibrous tissue and lipid was set at 60 HU as determined in previous studies [18]. We adjusted the cut-off point for the distinction between atherosclerotic plaque and vessel lumen for each patient on the basis of the full-width-half-maximum principle (mean lumen attenuation plus mean fibrous tissue attenuation (in our case the average was 88 HU) divided by two). The pixels surrounding the vessel lumen, with a density between 130 HU and the adjusted cut-off value, were considered to be fibrous tissue. We implemented the carotid artery outer vessel wall segmentation using the ITK (Insight Tool Kit) implementation [19].

5.3 *Experiments and Results*

5.3.1 Data Selection

From a database containing CTA datasets with manually segmented carotid arteries, we randomly selected 20 datasets that had the common, internal and external carotid artery annotated. The CTA data were acquired on a MDCT scanner (Siemens, Sensation 16, Erlangen, Germany), with a slice thickness of 1.0 mm and a pixel size of 0.23 mm.

5.3.2 Parameter Selection and Evaluation

The level set integration time step was set to 0.01. The remaining parameters of the method were curvature weight μ and the weights for inside and outside zero level set terms, λ_1, and λ_2. Pilot experiments showed that λ_2 should be equal or larger than λ_1, i.e. the negative values outside zero level set should be penalized more than positive values inside the zero level set. This was caused by the frequent occurrence of misclassified pixels inside the contour in the

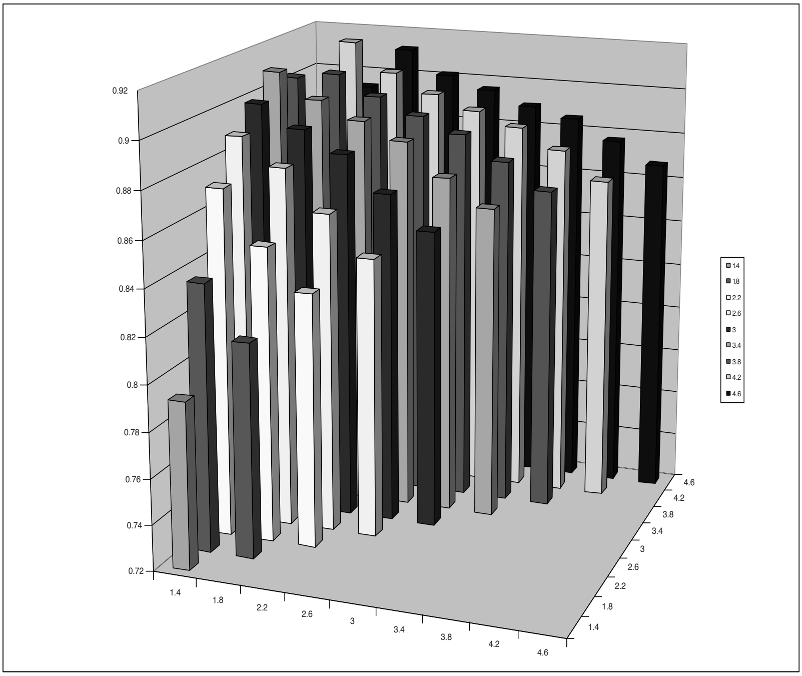

Figure. 5.2 Similarity indices between manual and automated segmentations of 20 CTAs of carotid arteries with μ=1 and λ_1 and λ_2 ranging from 1 to 6.2 with 0.4 steps keeping $\lambda_1 > \lambda_2$.

neighborhood of calcified regions (Fig 5.1). Note that this problem can not be addressed by increasing the curvature weight, as that would also result in misclassifying calcified regions. Additionally, from the pilot experiments it was concluded that the curvature term, μ, should be smaller than λ_1 and λ_2.

The final levelset result is determined by the ratios between the three parameters, the magnitude of the parameters (while maintaining the ratios) only changes the convergence speed. We optimized level set parameters on 20 CTAs of carotid arteries by fixing μ to 1.0 and varied λ_1 and λ_2 from 1.0 to 6.2 in steps of 0.4. Similarity indices are shown in Fig. 5.2.

Maximum Dice similarity index of 91.7% was reached for $\lambda_1 = 1.8$ and $\lambda_2 = 4.2$ and standard deviation was 2%.

The average Dice similarity index over additional 80 datasets using optimized set of parameters was 91.61%, and a standard deviation was 3%. Example segmentations are shown in Fig 5.3.

Plaque segmentation on 80 datasets reached an average similarity index of 80.43% with standard deviation of 6%. An example of plaque components segmented on one cross-sectional slice with the automated method and manually is shown in Fig. 5.4.

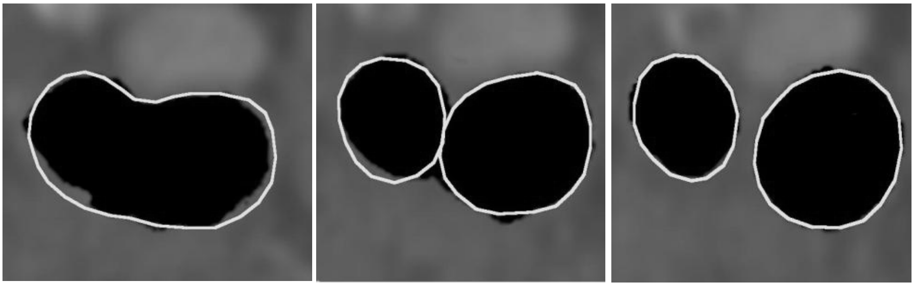

Figure5.3. Three crossectional slices around carotid artery bifurcation. Black mask is segmentation by our method, contour is the ground truth drawn by a clinician.

Figure 5.5 shows areas of total plaque and different plaque components according to the manual observer and those derived from our automated method. The correlation coefficient between method and manual segmentation is low ($R^2 = 0.46$) in the case of lipid volume. This is probably die to the fact that lipid tissue is usually located at the boundary of the vessel wall and has small size. Therefore differences in outer vessel wall segmentation primarily lead to differences in the fibrous tissue and lipid class. Indeed, inter observer error is also especially high for the lipid area [14].

Correlation coefficients between manual and automated plaque and plaque components volumes are similar for the proposed method to the ones we previously achieved with 2D ellipse fitting on 5 datasets [14]. However, similarity between automated and manual measurement of total plaque area is much higher for the new method (73% compared to 81%).

The automated level set segmentation of the outer vessel wall was accurate, with slightly higher average similarity index compared to method where ellipse fitting was used (92% versus 91%) [14].

5.4 Conclusion

We presented a method to segment the outer vessel wall of the carotid bifurcation in CTA. In contrast to previous work, where we used a slice-based fixed ellipse-shaped model for the common carotid artery, we now use a levelset based segmentation, which allows segmentation of the complete bifurcation. The experiments show that the levelset based approach achieves an average Dice similarity for the vessel of 92%. The method thus has large potential for the automated quantification of carotid artery plaque components.

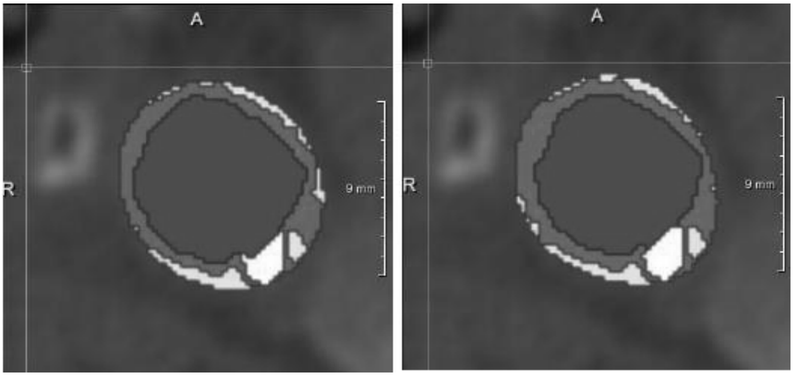

Fig. 5.4 Different plaque components on one crossectional slice segmented by the automated method (left) and manually (right). ■lumen, ▩fibrous, □lipids, ☐calcium.

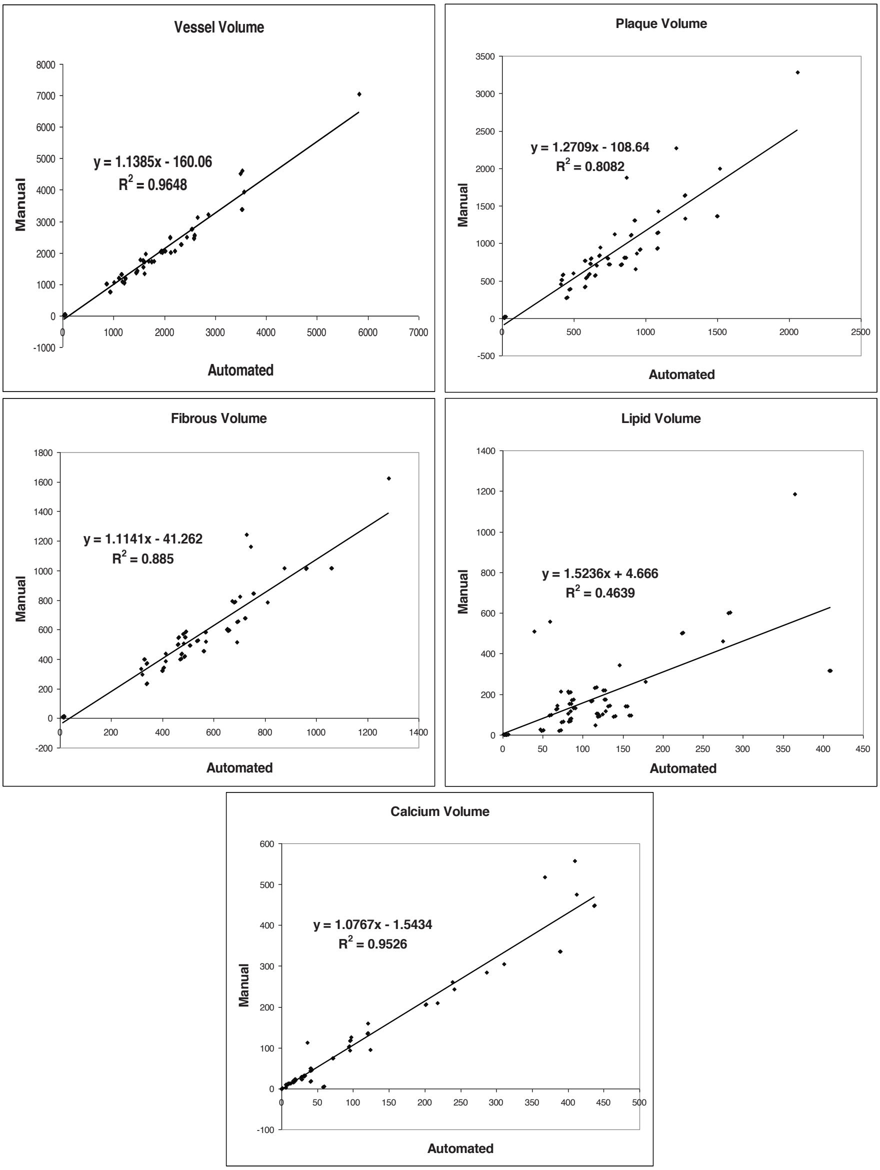

Figure 5.5 Regression plots showing the comparison between automated and manual measurements on 80 datasets.

5.5 References

[1] World health organization, Neglected global epidemics: three growing threats, *the world health report 2003 – Shaping the future,* 2003.

[2] M. J. W. Koelemay, P. J. Nederkoom, J. B. Reitsma and C. B. Majoie, Systematic review of computed tomographic angiography for assessment of carotid artery disease, *Stroke*, 35(10):2306-2312, 2004.

[3] North American symptomatic carotid endarterectomy trial collaborators, Beneficial effect of carotid endarterectomy in symptomatic patients with high-grade carotid stenosis, *N. Engl. J. Med.*, 325(7):445-453, Aug. 1991.

[4] S. Glagow, E. Weisenberg, C. K. Zarins, R. Stankunavicius and G. J. Kolettis. Compensatory enlargement of human atherosclerotic coronary arteries, *N Engl, J Med* , 316(22):1371-1375, May 1987.

[5] S. D. Olabarriaga, J. M. Rouet, M. Fradkin, M. Breeuwer and W. J. Niessen. Segmentation of thrombus in abdominal aortic aneurysms from CTA with non-parametric statistical grey level appearance modelling, *IEEE Trans. on Med. Imag.*, 24(4):477 - 485, Apr. 2005.

[6] M. de Bruijne, B. van Ginneken, W. J. Niessen, M. Loog and M. A. Viergever, Active shape model based segmentation of abdominal aortic aneurysms in CTA images, *SPIE Medical Imaging, ser. Proc. of the SPIE*, 4684:463–474, 2002.

[7] M. de Bruijne, B. van Ginneken, M. Viergever and W. Niessen. Interactive segmentation of abdominal aortic aneurysms in CTA data, *Med. Image Anal.*, 8(2):127–138, 2004.

[8] M. de Bruijne, B. van Ginneken, M. Viergever and W. Niessen. Adapting active shape models for 3D segmentation of tubular structures in medical images, *Information Processing in Medical Imaging, ser. LNCS,* 2732:136–147, 2003.

[9] C. Yuan, E. Lin, J. Millard and J. N. Hwang. Closed contour edge detection of blood vessel lumen and outer wall boundaries in black-blood MR images, *Magn. Reson. Imaging*, 17(2):257-266, Feb. 1999.

[10] G. J. Adams, G. W. Vick, C. B. Bordelon, W. Insull and J. D. Morrisett. An algorithm for quantifying advanced carotid artery artherosclerosis in humans using MRI and active contours, *Proc. SPIE Medical Imaging*, 4684:1448-1457, 2002.

[11] I. M. Adame, R. J. van der Geest, B. A. Wasserman, M. A. Mohamed, J. H. C. Reiber, B. P. F. Lelieveldt. Automatic segmentation and plaque characterization in atherosclerotic carotid artery MR images, *MAGMA*, 16(5):227 – 234, Apr. 2004.

[12] F. Liu, D. Xu, M. S. Ferguson, B. Chu, T. Saam, N. Takaya, T. S. Hatsukami, C. Yuan and W. S. Kerwin. Automated in vivo segmentation of carotid plaque MRI with morphology-enhanced probability maps, *Magnetic Resonance in Medicine*, 55:659 – 688, 2006.

[13] D. Vukadinovic, T. van Walsum, R. Manniesing, S. Rozie, R. Hameeteman, T. de Weert, A. van der Lugt and W. Niessen. Segmentation of

the Outer Vessel Wall of the Common Carotid Artery in CTA, *IEEE Transactions on Medical Imaging*, 29(1): 65-76, Jan. 2010.

[14] D. Vukadinovic, T. van Walsum, S. Rozie, T. T. de Weert, R. Manniesing, A. van der Lugt and W. J. Niessen. Carotid artery segmentation and plaque quantification in CTA, *IEEE International Symposium on Biomedical Imaging*, 2009

[15] F. Zhuge, S. Sun, G. D. Rubin and S. Napel. An abdominal aortic aneurysm segmentation method: level set with region and statistical information, *Medical Physics* 33(5):1440-1453, May 2006.

[16] R. Manniesing, B. K. Velthuis, M. S. van Leeuwen, I. C. van der Schaaf, P. J. van Laar and W. J. Niessen. Level set based cerebral vasculature segmenation and diameter quantification in CT angiography, *Med. Image Anal*, 10(2):200-214, Apr. 2006.

[17] T. F. Chan and L. A. Vese. Active contours without edges, *IEEE Transactions on Image Processing*, 10(2), Feb 2001.

[18] T. T. de Weert, M. Ouhlous, E. Meijering, P. E. Zondervan, J. M. Hendriks, M. R. H. M. van Sambeek, D. W. J. Dippel and A. van der Lugt. In vivo characterization and quantification of atherosclerotic carotid plaque components with multidetector computed tomography and histopathological correlation, *Arterioscler. Thromb. Vasc. Biol.*, 26(10):2366–2372, Oct 2006.

[19] K. R. Mosaliganti, B. Smith, A. Gelas, A. Gouaillard, S. G. Megason. Level set segmentation: active contours without edges, *Insight Journal,* 2009.

6 Summary and Conclusion

This thesis reports on the development and evaluation of automated methods for carotid lumen and carotid atherosclerotic plaque segmentation and quantification in CTA data. These methods were evaluated in various ways: with respect to stenosis degree, plaque volumes correlation with cardiovascular risk factors, similarity indices of lumen and vessel segmentation volumes, correlation coefficients and Bland – Altman plots of plaque components and lumen volumes. Manual measurements by clinical experts served as reference standard in these evaluations.

In Chapter 2 we described an automated carotid lumen segmentation method which was optimized for accurate stenosis quantification. The method uses three user – defined points (in the common, internal and external carotid artery) to extract centerlines that are used to initialize a level set method to segment the carotid artery lumen. The level set is steered by intensity statistics obtained from the intensities around the initial centerlines and the image intensity gradient. In order to determine the stenosis degree a new centerline is obtained from the segmentation and the lumen cross sections orthogonal to the centerline are extracted from the smoothed lumen segmentation surface. The stenosis area and diameter degree results were compared with manual measurements on 41 datasets from a standardized stenosis grading evaluation framework for CTA images of the carotid bifurcation. The mean stenosis quantification error was 19.3 % and 18.2 % for area stenosis and diameter stenosis respectively, and our method ranked second among four algorithms that have participated in the CLS2009 carotid challenge. The results show that automated stenosis grading is becoming feasible. The lumen segmentation similarity index of our method compared to the ground truth was 83%, while the average interobserver variability between three observers was 92%.

In Chapter 3 a method for automated outer vessel wall segmentation of the carotid artery was presented. The method uses a lumen segmentation approach similar to the method presented in Chapter 2. Given the lumen segmentation, calcified regions located inside the carotid artery were segmented using a GentleBoost framework that utilizes a number of spatial, shape, intensity and Gaussian image derivative features. Calcified region segmentation was used as a preprocessing step to outer vessel wall segmentation, to ensure that calcifications are included in the vessel wall. Next, a GentleBoost voxel based classifier was trained using spatial, intensity and Gaussian image derivative features to classify each voxel as being inside or outside the carotid artery. Finally, a 2D ellipse shape deformable model was fitted to a cost image derived from both the calcium and vessel wall classifications. The method was evaluated by comparison with manually delineated outer vessel wall on 60 datasets. The average similarity index between vessels segmented by our method and the vessels segmented by experienced observers on 40 datasets was 91.3%. Additionally, the results were compared with interobserver variability on 20 datasets. Two experienced observers manually delineated the carotid artery outer vessel wall. The similarity indices between our method and the observer's segmentation were 90.5% and 89.8%, while the similarity index between two observers were 92.1%. The results showed that the difference between the method and the manual observers is comparable to the difference between two observers.

In Chapter 4 an automated atherosclerotic plaque measurement approach for carotid arteries using the method described in Chapter 3 was validated by comparing associations of cardiovascular risk factors with plaque volume and plaque composition. Using the carotid artery vessel wall and lumen segmentation, different Hounsfield unit ranges were used to define calcifications, fibrous tissue and lipids within the plaque. These Hounsfield ranges were previously validated using histology. On 40 datasets the automated method was evaluated by comparing plaque volume, plaque component volumes and plaque component percentages measured with the automated method with the measurements of two experienced observers. The differences in measurements between the automated method and the observers were comparable to interobserver variability. On an additional 60 datasets, the automated plaque and plaque components measurements were associated with cardiovascular risk factors: age, gender, hypercholesterolemia, hypertension, diabetes mellitus, smoking, previous cardiac disease and previous cerebrovascular disease. We showed that associations between cardiovascular risk factors and automated plaque measurements were mostly similar to the associations found with manual plaque measurements. Seven associations were significant for both the automated and manual plaque measurements; one was significant for the automated method and almost significant for manual method and three were significant for only one of the methods. The associations that were found to be significant for both manual and automated measurements also had similar correlation coefficient values. This study demonstrated that our automated measurements can potentially be used to replace manual measurements in large imaging studies which aim to associate plaque characteristics with cardiovascular risk factors.

In Chapter 5 a novel level set based method was used in order to segment the carotid outer vessel wall in CT. The method uses a GentleBoost classification framework that classifies pixels as calcified region or not, and inside or outside the vessel wall as in Chapter 2. The combined result of both classifications is used to construct a speed function for level set based segmentation of the outer vessel wall; the segmented lumen is used to initialize the level set. The level set method was a modified version of Chan and Vese region based level set approach [2]. The method was evaluated on 80 datasets for which manually annotated data was available as a reference. The average Dice similarity index of the outer vessel wall segmentation was 92%, which compared favorably to previous methods. Plaque segmentation on 80 datasets reached an average similarity index of 80% which is substantially better than the result (73%) we obtained with the method described in Chapter 3 and 4, albeit on a different dataset.

In summary, this thesis describes methods that were developed and evaluated for automated assessment of atherosclerotic disease in the carotid arteries. The image processing methods utilize deformable models and machine learning algorithms and are trained using a dataset of annotated images. Several features, related to image intensity, spatial location, and object shape are used to automatically delineate vessel wall and lumen boundary of the carotid artery in MDCT data. Thereby, a number of parameters important for atherosclerotic disease quantification can be obtained: stenosis degree, plaque thickness, plaque volume and plaque composition. The automated outer vessel wall algorithms were evaluated on large datasets. The results showed that the errors of our methods were within the interobserver variability. Comparison of association of manual and automated measurments with cardiovascular risk factors showed that our methods can be used for automated analysis in large studies. To the best of our knowledge, these studies are the first to evaluate the segmentation of the outer vessel wall of the carotid artery in CTA. The automated outer vessel wall and plaque segmentation tool based on the methods presented in Chapter 3 and Chapter 4 was used in a clinical study that quantified temporal changes in carotid atherosclerotic plaque volume and composition using MDCT data [3]. This study indicates that the automated measurement of plaque volumes improves reproducibility. When we compare our results, obtained with a semi-automated plaque segmentation method, with the inter-observer reproducibility found in a previous study in which plaque segmentation was performed manually, inter-observer reproducibility improved; coefficient of variation for plaque volume was 15% compared to 23-34% found with the manual segmentation method [3]. De Weert et al. demonstrated that their moderate inter-observer reproducibility was partly due to the difficulty of defining the exact plaque range; consensus about the segmentation range improved the reproducibility [4]. Therefore, defining a fixed range around the bifurcation may further improve inter-observer and intra-observer reproducibility of the automated plaque measurements presented in this thesis. The automated stenosis grading method presented in this thesis achieved reasonable similarity with the manual stenosis measurements. The method was evaluated by participating in a challenge [1] using data from three different vendors. Validation within the context of a challenge ensures that the results of our method can objectively be compared to other algorithms. Furthermore, the availability of datasets of multiple vendors in the challenge, ensures that there is no bias of the result to a specific imaging protocol. In comparison with other participants the method scored second out of four participants.

The evaluation studies on plaque volume and plaque composition have some limitations. One of the limitations is that we do not have a definite gold standard for plaque volume and plaque components. Only in a limited number of cases, histological specimens are available. We therefore compared results from automated plaque segmentation with those from manual plaque segmentation - a method previously validated against histology – thus indirectly evaluating the performance of our automated method. Another limitation is that the validation of our outer vessel wall and plaque segmentation methods were validated on CTA data from a single vendor at a single site. The methods may perform worse using data from different vendors or different sites. On the other hand, our methods performed very robustly when tested on large datasets. These are very promising results with respect to the possible application in clinical practice. It has to be stressed however, that the comparison of cardiovascular risk factors associations obtained with manually and automatically segmented plaque and its components does not provide information on the method applicability on a single subject. We can only conclude that the method can be used used to find similar associations in a group study.

In order to segment the carotid outer vessel wall, we used a two step method, in which first voxels were classified, and then a geometric model was fitted to the classification results. Both ellipse fitting (Chapter 3) and level set evolution (Chapter 5) have been used on the result of the voxel based inner – outer vessel region classification. Less shape restricted and 3-dimensional level set method performed substantionally better in plaque segmentation. The automated levelset segmentation of the outer vessel wall had slightly higher average similarity index compared to method where ellipse fitting was used (92% versus 91%). However, similarity between automated and manual measurement of total plaque area is much higher for the level set method: 81% versus 73%.

The voxel based classification features were calculated in axial slices. We expect the classification results to improve if the features would be extracted from the slices orthogonal to the centerline of carotid lumen. Also, segmenting each plaque component separately instead of using different HU ranges within segmented outer vessel wall could be a more successful path towards determining plaque composition.

In this thesis we concentrated on analyzing carotid artery CTA data. In contrast to CT, MRI is capable of visualizing multiple aspects of the plaque, including e.g. fibrous cap rupture and intraplaque hemorrhage. The latter plaque features are highly associated with plaque rupture and ischemic events [5-9]. Intraplaque hemorrhage has also been associated with an accelerated plaque growth [8]. Using intensity information from different MRI sequences would probably improve the accuracy of the classifier presented in Chapter 3. Similarly, the application of dual-energy CT may provide more accurate measurements of soft-tissue components of the plaque, since it allows the removal of calcifications [10]. As the presented methods in this thesis are generic, we expect that the presented approach can also be successfully be applied to these imaging modalities, and other vessel anatomies.

6.1 References

[1] K. Hameeteman, M. A. Zuluaga, M. Freiman, et al. Evaluation framework for carotid bifurcation lumen segmentation and stenosis grading, *Medical Image Analysis*, 2011.

[2] T. F. Chan and L. A. Vese. Active contours without edges, *IEEE Transactions on Image Processing*, l 10(2), Feb 2001.

[3] M. J. van Gils, D. Vukadinovic, D. Dippel, et al. Carotid **a**therosclerotic plaque progression and change in plaque composition over time: a 5-year follow-up study with serial CT angiography, *American Journal of Neuroradiology*, in press

[4] T. T. de Weert, C. de Monye, E. Meijering, et al. Assessment of atherosclerotic carotid plaque volume with multidetector computed tomography angiography, *Int J Cardiovasc Imaging,* 24:751-59, 2008.

[5] N. Altaf, S. T. MacSweeney, J. Gladman, et al. Carotid intraplaque hemorrhage predicts recurrent symptoms in patients with high-grade carotid stenosis, *Stroke,* 38:1633-35, 2007.

[6] T. S. Hatsukami, R. Ross, N. L. Polissar, et al. Visualization of fibrous cap thickness and rupture in human atherosclerotic carotid plaque in vivo with high-resolution magnetic resonance imaging, *Circulation,* 102:959-64, 2000.

[7] C. Yuan, S. X. Zhang, N. L. Polissar, et al. Identification of fibrous cap rupture with magnetic resonance imaging is highly associated with recent transient ischemic attack or stroke, *Circulation,* 105:181-85, 2002.

[8] N. Takaya, C. Yuan, B. Chu, et al. Presence of intraplaque hemorrhage stimulates progression of carotid atherosclerotic plaques: a high-resolution magnetic resonance imaging study, *Circulation,* 111:2768-75, 2005.

[9] N. Takaya, C. Yuan, B. Chu, et al. Association between carotid plaque characteristics and subsequent ischemic cerebrovascular events: a prospective assessment with MRI-initial results, *Stroke,* 37:818-23, 2006.

[10] K. Uotani, Y. Watanabe, M. Higashi, et al. Dual-energy CT head bone and hard plaque removal for quantification of calcified carotid stenosis: utility and comparison with digital subtraction angiography, *Eur Radiol,* 19:2060–2065, 2009.

Samenvatting

Dit proefschrift rapporteert over de ontwikkeling en evaluatie van geautomatiseerde methoden voor de segmentatie en kwantificatie van het lumen en atherosclerotische plaque compositie in de halsslagader op basis van CT angiografie beelden (CTA). Deze methoden werden geëvalueerd op verschillende manieren: we hebben de segmentatie van het lumen en mate van vernauwing vergeleken met een referentie-standaard, en daarnaast gekeken naar de correlatie van plaque volume en compositie met cardiovasculaire risicofactoren. Handmatige metingen door klinische experts werden gebruikt als de referentie-standaard in deze evaluaties.

In hoofdstuk 2 beschreven we een geautomatiseerde segmentatie methode voor het bepalen van het lumen van de halsslagader. De methode is geoptimaliseerd voor een nauwkeurige kwantificatie van vernauwingen in het lumen. De methode start met het aangeven van drie initialisatie punten door de gebruiker (in de gemeenschappelijke, interne en externe halsslagader) om de middellijnen van de vaten te bepalen. Deze middellijnen worden vervolgens gebruikt om een level set methode te initialiseren om het lumen van de halsslagader te segmenteren. De level set wordt aangestuurd door intensiteitsstatistieken die verkregen zijn op basis van de intensiteiten rond de initiële middellijnen en de intensiteiten in het beeld. Om de mate van vernauwing te bepalen wordt er op basis van de segmentatie eerst een nieuwe middellijn bepaald en vervolgens wordt het lumen doorsneden loodrecht op deze nieuwe middellijn. Hierna werden de oppervlakte en diameter vergeleken met handmatige metingen op 41 datasets, die in het kader van de CLS2009, een grote evaluatie-studie voor het verwerken van CTA-beelden van de halsslagader, zijn verkregen. De gemiddelde fout in de kwantificatie van de vernauwing was 19,3% en 18,2% voor respectievelijk de oppervlakte vernauwing en diameter vernauwing, en onze methode eindigde op de tweede plaats tussen vier algoritmen die deelgenomen hebben aan de CLS2009 evaluatie. De resultaten laten zien dat geautomatiseerde bepaling van lumen vernauwing binnen handbereik is. De mate van overlap van onze lumen segmentatie met de referentie-standaard was 83%, terwijl de gemiddelde variabiliteit tussen drie manuele metingen 92% was.

In hoofdstuk 3 is een methode voor geautomatiseerde segmentatie van de vaatwand van de halsslagader gepresenteerd. De methode maakt gebruik van een lumen segmentatie aanpak die vergelijkbaar is met de methode beschreven in Hoofdstuk 2. Gegeven de lumen segmentatie, worden eerst verkalkte gebieden die zich in de halsslagader bevinden gedetecteerd en gesegmenteerd via de GentleBoost methode, die een aantal ruimtelijke, vorm, en intensiteit kenmerken gebruikt om te bepalen of een gebiedje met hoge intensiteit een verkalkt gebied is of niet. De segmentatie van het verkalkte gebied word als voorbewerkingsstap gebruikt voor de vaatwand segmentatie, om ervoor te zorgen dat de verkalkte gebieden zich binnen de vaatwand bevinden. Vervolgens wordt een GentleBoost voxel gebaseerde classificator getraind om de vaatwand te extraheren. De classifator maakt daarbij gebruik van spatiële informatie, intensiteit en afgeleide kenmerken, om elke voxel te classificeren als binnen of buiten de halsslagader. Tot slot wordt een 2D ellipsoide model gebruikt om, aan de hand van de calcium- en vaatwand classificaties, te bepalen waar de vaatwand zich bevindt. De methode werd geëvalueerd door vergelijking met handmatig annotaties van de vaatwand op 60 datasets. De gemiddelde overlap van vaten gesegmenteerd op basis van onze methode en de vaten gesegmenteerd door ervaren waarnemers op 40 datasets was 91,3%. Daarnaast werden de resultaten vergeleken met de overlap tussen twee waarnemers op 20 datasets. Over deze 20 datasets was de overlap van de segmentatie van onze methode en die van beide waarnemers 90,5% en 89,8%, terwijl de overlap van de segmentaties van de twee waarnemers 92,1% bedroeg. De resultaten laten zien dat het verschil tussen onze methode en de handmatige waarnemers vergelijkbaar is met het verschil tussen twee waarnemers, en dat de methode dus gebruikt kan worden om de waarnemer te vervangen.

In hoofdstuk 4 werd een geautomatiseerde methode, die atherosclerotische plaque in de halsslagaders kan bepalen, gevalideerd. We valideren de methode door correlaties van cardiovasculaire risicofactoren met plaque volume en plaque samenstelling te bepalen. We hebben dit zowel voor de handmatige en automatische analyse van de plaque gedaan, en bepalen of de correlaties met de handmatige methode gereproduceerd kunnen worden met de automatische methode. We maakten gebruik van de eerder beschreven methoden om het lumen en de vaatwand van de halsslagader te bepalen. Vervolgens werden verschillende Hounsfield Unit drempels gebruikt om gebieden met calcificaties, vezelig weefsel en lipiden te definiëren. Deze drempels zijn gevalideerd in eerder onderzoek met behulp van histologie. Eerst is een validatie toegepast op 40 datasets, om plaque volume en plaque compositie gemeten met de manuele en automatische methode te vergelijken . De verschillen in metingen tussen de geautomatiseerde methode en de waarnemers waren vergelijkbaar met variabiliteit tussen waarnemers. Op nog eens 60 datasets werd het geautomatiseerd verkregen plaque volume en de plaque compositie geassocieerd met cardiovasculaire risicofactoren: leeftijd, geslacht, hypercholesterolemie, hypertensie, diabetes mellitus, roken, eerdere hart-en vaatziekten en eerdere cerebrovasculaire ziekte. We toonden aan dat associaties tussen cardiovasculaire risicofactoren en geautomatiseerde plaque metingen over het algemeen vergelijkbaar waren met de associaties gevonden met handmatige plaque metingen. Zeven associaties waren significant voor zowel de automatische en handmatige plaque metingen; één was significant voor de automatische methode en bijna significant voor handmatige methode en drie waren significant voor slechts een van de methoden. De associaties die significant bleken te zijn voor zowel handmatige als geautomatiseerde metingen hadden ook vergelijkbare correlatiecoëfficiënten. Deze studie toonde aan dat onze geautomatiseerde metingen mogelijk kunnen worden gebruikt om handmatige metingen te vervangen, wat een belangrijke ondersteuning zou betekenen voor grote beeld studies die gericht zijn op het associëren van plaque kenmerken met cardiovasculaire risicofactoren.

In hoofdstuk 5 is een nieuwe level set methode geïntroduceerd voor het segmenteren van de vaatwand van de halsslagader in CTA beelden. Ook deze methode maakt gebruik van een GentleBoost kwalificatie methode welke pixels classificeert als verkalkte regio of niet, en binnen of buiten de vaatwand zoals beschreven in hoofdstuk 2. Het gecombineerde resultaat van beide classificaties wordt gebruikt om een snelheidsfunctie te construeren voor level set gebaseerde segmentatie van de buitenste vaatwand; het gesegmenteerde lumen van de halsslagader wordt gebruikt om de level set te initialiseren. De genruikte level set methode is een aangepaste versie van Chan en Vese level set benadering. De methode werd geëvalueerd op 80 datasets, en handmatig geannoteerde data werden gebruikt als een referentie. De gemiddelde overlap van de vaatwand segmentatie was 92%, wat beter was dan de overlap die gerapporteerd is in studies uitgevoerd met andere methoden. Plaque segmentatie bij 80 datasets bereikte een gemiddelde overlap index van 80%, wat aanzienlijk beter is dan het resultaat (73%) dat verkregen is met de werkwijze beschreven in hoofdstuk 3 en 4. Hierbij moet worden opgemerkt dat dit resultaat verkregen is met een andere dataset.

Samenvattend zijn in dit proefschrift methoden voor de automatische beoordeling van atherosclerose in de halsslagaders ontwikkeld en geëvalueerd. De gebruikte beeldverwerkingsmethoden maken gebruik van vervormbare modellen en patroon herkenningstechnieken, die getraind zijn met behulp van een dataset van geannoteerde afbeeldingen. Met de ontwikkelde technieken kan relevante informatie over de atherosclerotische halsslagader automatische workden verkregen, zoals de mate van stenose, de plaque dikte, het plaque volume en de plaque samenstelling. Uit evaluaties van de algoritmes, zowel op nauwkeurigheid van het sementatie resultaat, als op het vermogen om correlaties met risicio-factoren die in eerdere studies zijn gevonden te repliceren, blijkt dat de methoden veel potentie hebben om manuele analyse van CTA data van de halsslagader te vervangen. Voor zover wij weten, zijn dit de eerste studies die de segmentatie van de buitenste vaatwand van de halsslagader in de CTA hebben geëvalueerd.

PhD Portfolio

In-Depth Courses:

Front-End Vision and Multiscale Image Analysis, ASCI	2006
Knowledge driven image segmentation, ASCI	2007
Imaging of carotid bifurcation atherosclerosis, COEUR	2008
Marketing yourself effectively, NWO talent classes	2009

Presentations:

Medical Informatics PhD days	2008
NVPHBV fall meeting, Eindhoven	2008
SPIE Medical Imaging, San Diego	2008
IEEE International Symposium on Biomedical Imaging	2009
Research seminars: Biomedical Imaging Group Rotterdam	2007-2010

Attending National and International Conferences:

SPIE Medical Imaging, San Diego	2008
NVPHBV fall meeting, Eindhoven	2008
IEEE International Symposium on Biomedical Imaging	2009
2nd Dutch Conference on Bio-Medical Engineering	2009
IEEE International Symposium on Biomedical Imaging: From Nano to Macro, Rotterdam	2010

Other:

Reviewing for *IEEE Transactions on Medical Imaging* and *Neuroradiology* journals.	2011-2012

Publications

Publications in international journals:

M. .J. van Gils, **D. Vukadinovic**, D. W. J. Dippel, W. J. Niessen and A. van der Lugt. Carotid Atherosclerotic Plaque Progression and Change in Plaque Composition over Time: A 5-year Follow-up Study with Serial CT Angiography, *American Journal of Neuroradiology*, in press

D. Vukadinović, S. Rozie, T. van Walsum, R. Manniesing, A. van der Lugt, W. J. Niessen. Automated versus manual segmentation of atherosclerotic carotid plaque volume and components in CTA: associations with cardiovascular risk factors, *The International Journal of Cardiovascular Imaging*, May, 2011.

R. Manniesing, M. Schaap, S. Rozie, K. Hameeteman, **D. Vukadinović**, A. van der Lugt and W. J. Niessen. Robust CTA Lumen Segmentation of the Atherosclerotic Carotid Artery Bifurcation in a Large Patient Population, *Medical Image Analysis*, Dec 2010

D. Vukadinović, T. van Walsum, R. Manniesing, S. Rozie, K. Hameeteman, T. T. de Weert, A. van der Lugt and W. J. Niessen. Segmentation of the Outer Vessel Wall of the Common Carotid Artery in CTA, *IEEE Transactions on Medical Imaging*, 2010

Publications in Conference Proceeding:

D. Vukadinović, S. Rozie, T. van Walsum, R. Manniesing, A. van der Lugt, Wiro J. Niessen. Region Based Level Set Segmentation of the Outer Vessel Wall of the Carotid Bifurcation in CTA, *SPIE Medical Imaging 2011: Image Processing*, 2011

D. Vukadinović, T. van Walsum, S. Rozie, T. T. de Weert, R. Manniesing, A. van der Lugt and W.J. Niessen. Carotid Artery Segmentation and Plaque Quantification in CTA, *IEEE International Symposium on Biomedical Imaging*, 2009.

D. Vukadinović, T. van Walsum, R. Manniesing, A. van der Lugt, T. T. de Weert and W.J. Niessen. AdaBoost Classification for Model Based Segmentation of the Outer Vessel Wall, *SPIE Medical Imaging 2008: Image Processing*, 2008

D. Vukadinović and M. Pantic. Fully automatic facial feature point detection using Gabor feature based boosted classifiers, *in Proc. IEEE Int'l Conf. on Systems, Man and Cybernetics (SMC '05)*, pp. 1692-1698, Waikoloa, Hawaii, October 2005

Conference Abstracts:

M. J. van Gils, **D. Vukadinović,** D. W. J. Dippel, W. J. Niessen and A. van der Lugt. Carotid Atherosclerotic Plaque Progression and Change in Plaque Composition over Time: A 5-year Follow-up Study with Serial CT Angiography, *Radiological Society of North America*, 97th Scientific Assembly and Annual Meeting, 2011.

R. Manniesing, **D. Vukadinović**, S. Rozie, M. Schaap, A. van der Lugt and W.J. Niessen. Automated CTA Lumen Segmentation of the Atherosclerotic Carotid Artery Bifurcation in a Large Patient Population, *Radiological Society of North America*, 95th Annual Meeting, 2009.

D. Vukadinović, T. van Walsum, R. Manniesing, S. Rozie, T. T. de Weert, A. van der Lugt and W.J. Niessen. Automated Segmentation of Atherosclerotic Plaque in MDCT Angiography of the Carotid Artery, *2nd Dutch Conference on Bio-Medical Engineering*, 2009.

S. Rozie, **D. Vukadinović**, L. van den Borne, W. J. Niessen, D. J. W. Dippel, A. van der Lugt. Does the amount of calcifications represent the total plaque burden in the carotid artery: An analysis with multidetector CT angiography, *European Congress of Radiology*, 2009.

T. T de Weert, **D. Vukadinovic**, C. de Monye, T. van Walsum, W. J. Niessen, A. van der Lugt. Atherosclerotic carotd plaque quantification with multidetector computed tomography angiography, *European Congress of Radiology*, 2007.

Curriculum Vitae

Danijela Vukadinović was born in Belgrade, Yugoslavia, on February 18, 1978. She received an M.Sc degree in Electrical Engineering (Telecommunications) from the Electrical Engineering Faculty of Belgrade Univeristy, Serbia, in 2003. Her graduation project was on the edge detection in images using wavelets. In 2004 she participated in a research project at Electrical Engineering Univeristy in Belgrade that inculeded vowel sounds recognition. From 2004 to 2005 she carried out research at Man-Machine interaction group in TU Delft about face and facial expressions recognition and emotions classification in images. From 2006 to 2011 Danijela was a PhD student at the Biomedical Imaging Group Rotterdam, Erasmus MC, the Netherlands. The results of this work are presented in this book. In 2011 she joined the IAC group in VUMC Amsterdam.